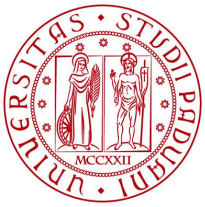

UNIVERSITÀ DEGLI STUDI DI PADOVA

TÉCNICO LISBOA

UNIVERSITÀ DEGLI STUDI DI PADOVA
CENTRO INTERDIPARTIMENTALE *"Centro Ricerche Fusione"*

UNIVERSIDADE TÉCNICA DE LISBOA
INSTITUTO SUPERIOR TÉCNICO

JOINT RESEARCH DOCTORATE IN FUSION SCIENCE AND ENGINEERING
CYCLE XXVI

Characterisation of impurity behaviour in RFX-mod and MST reversed-field pinches

Coordinator: Ch.mo Prof. Piero Martin
Supervisor: Ch.mo Prof. Leonardo Giudicotti
Supervisor: Dott.ssa Lorella Carraro

Doctoral student: Tullio Barbui

January 2014

Abstract

The work presented in this thesis is inserted in the field of the research on plasma physics conducted with magnetically confined devices, whose ultimate goal is the demonstration of the feasibility of the energy production through fusion reactions between nuclei of hydrogen isotopes.

One of the major issues in the operation of a magnetically confined plasma, both in a present device and in a future reactor, is the presence in the plasma of other elements besides the main gas: the so called impurities. These originate mainly by the interaction of the hot plasma with the plasma facing materials, which can both be eroded and release atmospheric gases previously adsorbed. Once these impurities enters the plasma they get ionised and start emitting radiation through bremsstrahlung and atomic processes (line and recombination radiation). If impurities accumulate in the core plasma, where the temperature is highest, this can lead to a dramatic increase in radiation losses, drive radiative instabilities and dilute the plasma with negative consequences on plasma reactivity.

In this regard it is extremely important to keep as low as possible the total impurity content and to control the impurity peaking, i.e. where impurities accumulate. The first point can be addressed by a correct choice of the plasma facing components and by conditioning the first wall. The second point needs a study of the impurity transport in different scenarios, understanding what prevents the accumulation of ions in the core. The radial impurity flux is usually expressed by means of two transport coefficients: the diffusion coefficient and the convective velocity. The determination of these coefficients in different scenarios allows to understand and control the impurity peaking.

The Ph.D. activity developed during these three years is focused on this topic: the understanding of the impurity transport behaviour in different scenarios by means of the determination of the transport coefficients. This analysis has been conducted on a particular magnetic configuration: the reversed-field pinch. It has been carried out on the two main devices operating in this configuration: RFX-mod located in Padua (Italy) and MST located in Madison (WI, USA).

The analysis method consists in the reproduction by means of a 1D impurity transport code of the plasma signals which are mainly affected by the presence of impurities. In order to discriminate the two coefficients, transients in the plasma signals are needed, which are then reproduced by the code. These transients are usually induced by means of artificially introduced impurities; the code reproduces the variations in the emission patterns or in the impurity density (depending on the available measurements) which are caused by the introduced atoms. By matching the simulation with the measurements an estimation of the transport coefficients is obtained. Once the coefficients have been estimated, they are compared with theoretical models in order to understand the nature of the transport in a particular plasma scenario.

For both machines, through the application of this method, the transport of different species of impurities (intrinsic and not) in different magnetic regimes has been studied. In RFX-mod, experiments with injected pellets of carbon and lithium have been carried out and subsequently reproduced with the code, allowing to determine the transport coefficients for the two elements. Moreover, first experiments with introduced tungsten have been conducted; its emission spectrum has been acquired and its penetrating capability investigated. In MST time-dependent

impurity density measurements were available for different intrinsic species in two magnetic regimes; their reproduction with the transport code allowed to estimate the transport coefficients.

This manuscript is organised in two main parts: first three chapters form the introductory part, chapters four and five form the original work of this thesis.

Chapter 1 introduces the role of impurities in fusion plasmas. The production processes are described as well as the impurity effects on the plasma properties. Emitted radiation from impurities is divided into its components (continuum and produced by atomic processes) and briefly characterised. Then the different models used to describe the ion populations are presented: coronal, local thermodynamic and collisional-radiative. Finally the impurity radial transport is depicted in its analytical form, according to the classical and neo-classical formulation.

Chapter 2 describes the reversed-field pinch magnetic configuration. Particle transport in this configuration is analytically presented.

Chapter 3 gives the details of the simulation tool used in this thesis for reproducing experimental measurements. The code consists of a transport model coupled to a collisional-radiative model for various species. Both models are detailed as well as the inputs and outputs to the code.

Chapter 4 reports the analysis performed at RFX-mod on impurity transport. The transient experiments conducted through pellets injection of carbon and lithium are described and the results presented. Transport coefficients are estimated for the different species in different magnetic scenarios. Then experiments with tungsten injection through the laser-blow off technique are presented and the results discussed and compared with reports from other devices.

Chapter 5 deals with the analysis realised at MST on impurity transport. Impurity density measurements carried out for different intrinsic species in different plasma regimes are reproduced with the code. The estimated transport coefficients are presented and compared with theoretical models.

Chapter 6 concludes the thesis with a discussion of the most important results achieved and an overview of possible future developments.

Sommario

Il lavoro presentato in questa tesi si inserisce nel campo della ricerca sulla fisica del plasma condotta con dispositivi confinati magneticamente, il cui obiettivo finale è la dimostrazione della fattibilità della produzione di energia attraverso reazioni di fusione tra nuclei di isotopi di idrogeno.

Uno dei principali problemi nell'operare un plasma a confinamento magnetico, sia in un esperimento attuale che in un futuro reattore, è la presenza nel plasma di altri elementi oltre il gas principale: le cosiddette impurezze. Esse si originano principalmente dall'interazione del plasma caldo con i materiali che si affacciano sullo stesso; questi materiali possono essere sia erosi sia rilasciare gas atmosferici precedentemente adsorbiti. Una volta che queste impurezze entrano nel plasma, esse vengono ionizzate ed emettono radiazione attraverso bremsstrahlung e processi atomici (radiazione di linea e di ricombinazione). Se le impurezze si accumulano nel centro del plasma, dove la temperatura è più alta, questo può portare a un drammatico aumento delle perdite tramite radiazione, si possono generare instabilità radiative e il plasma viene diluito con conseguenze negative sulla sua reattività.

A questo proposito è estremamente importante mantenere il più basso possibile il contenuto totale di impurezze e controllarne il picco, cioè la posizione in cui si accumulano. Il primo punto può essere affrontato con una corretta scelta dei materiali che si affacciano al plasma e condizionando la prima parete. Il secondo punto necessita di uno studio del trasporto di impurezze in diversi scenari, comprendendo cosa ne impedisce l'accumulo nel centro del plasma. Il flusso radiale di impurezze è generalmente espresso mediante due coefficienti di trasporto: il coefficiente di diffusione e la velocità convettiva. La determinazione di questi coefficienti in diversi scenari permette di capire e controllare il picco delle impurezze.

L'attività di dottorato sviluppata durante questi tre anni è incentrata su questo argomento: la comprensione del comportamento del trasporto di impurezze in diversi scenari mediante la determinazione dei coefficienti di trasporto. Questa analisi è stata condotta su una particolare configurazione magnetica: la strizione a campo rovesciato. Lo studio è stato effettuato sui due principali esperimenti operanti in questa configurazione: RFX-mod situato a Padova (Italia) e MST situato a Madison (WI, USA).

Il metodo di analisi consiste nella riproduzione per mezzo di un codice unidimensionale di trasporto di impurezze dei segnali di plasma che sono principalmente interessati dalla presenza di impurezze. Per discriminare i due coefficienti sono necessari dei transienti nei segnali del plasma, che vengono poi riprodotti dal codice. Questi transienti sono solitamente indotti mediante l'introduzione artificiale di impurezze nel plasma; il codice riproduce le variazioni nelle emissioni o nella densità delle impurezze (a seconda delle misurazioni disponibili), causate dagli atomi introdotti. Riproducendo le misurazioni con la simulazione, si ottiene una stima dei coefficienti di trasporto. Una volta che i coefficienti sono stati stimati, essi sono confrontati con modelli teorici per comprendere la natura del trasporto in un particolare scenario del plasma.

Per entrambe le macchine, attraverso l'applicazione di questo metodo, è stato studiato il trasporto di diverse specie di impurezze (intrinseche e non) in diversi regimi magnetici. In RFX-mod, sono stati eseguiti e successivamente riprodotti con il codice diversi esperimenti con iniezione di pellet di carbonio e litio, consentendo di determinare i coefficienti di trasporto per i due elementi. Inoltre sono stati condotti i primi esperimenti con iniezione di tungsteno; il suo

spettro di emissione è stato acquisito e la sua capacità penetrante è stata indagata. In MST erano disponibili delle misurazioni della densità di impurezze per le varie specie intrinseche; queste misurazioni sono dipendenti dal tempo ed eseguite in due diversi regimi magnetici. La loro riproduzione con il codice di trasporto ha permesso di stimare i coefficienti di trasporto.

Questo manoscritto è organizzato in due parti principali: i primi tre capitoli costituiscono la parte introduttiva, i capitoli quattro e cinque formano il lavoro originale di questa tesi.

Capitolo 1 introduce il ruolo delle impurezze nei plasmi fusionistici. Ne sono descritti i processi di produzione come pure i loro effetti sulle proprietà del plasma. La radiazione emessa dalle impurezze è suddivisa nelle sue componenti (continua e prodotta da processi atomici), le quali sono brevemente caratterizzate. Successivamente vengono presentati i diversi modelli utilizzati per descrivere le popolazioni di ioni: corona, termodinamico locale e collisionale-radiativo. Infine il trasporto radiale di impurezze è raffigurato nella sua forma analitica, secondo la formulazione classica e neo-classica.

Capitolo 2 descrive la configurazione magnetica della strizione a campo rovesciato. Il trasporto di particelle in questa configurazione è presentato analiticamente.

Capitolo 3 fornisce i dettagli dello strumento di simulazione utilizzato in questa tesi per la riproduzione delle misure sperimentali. Il codice è costituito da un modello di trasporto accoppiato ad un modello collisionale-radiativo per varie specie. Sono descritti entrambi i modelli nonché gli ingressi e le uscite del codice.

Capitolo 4 riporta l'analisi effettuata su RFX-mod circa il trasporto di impurezze. Sono descritti gli esperimenti transitori condotti attraverso l'iniezione di pellet di carbonio e litio e ne sono presentati i risultati. I coefficienti di trasporto sono stimati per le diverse specie in diversi scenari magnetici. In seguito sono presentati gli esperimenti effettuati con l'iniezione di tungsteno attraverso la tecnica dello sfogo di laser; i risultati sono discussi e confrontati con i resoconti di altri esperimenti.

Capitolo 5 affronta l'analisi realizzata su MST circa il trasporto di impurezze. Le misurazioni della densità di impurezze effettuate per le varie specie intrinseche sono riprodotte con il codice in diversi regimi di plasma. Sono presentati i coefficienti di trasporto stimati e sono confrontati con i modelli teorici.

Capitolo 6 conclude la tesi con una discussione dei risultati più importanti conseguiti ed una panoramica dei possibili sviluppi futuri.

Contents

Chapter 1

The role of impurities in fusion plasmas

This chapter introduces the role of impurities in fusion plasmas from a generic point of view, i.e. valid both for tokamaks and for RFPs. The mechanisms of impurity production are described as well as the impurity effects on plasma performance and control. Then, the attention is focused on the radiation produced by the plasma and on the atomic processes involved in the impurity emissions. Finally, in order to model the impurity phenomena, several types of equilibria are introduced and the impurity perpendicular transport is analysed.

1.1 Impurity production

Besides the basic gas ions (generally protons or deuterons), fusion plasmas always contain traces of impurity ions, produced by interaction with the limiter or the divertor, if the device is equipped with, or the first wall if the device does not have any of them. These interactions are generally referred to as plasma-wall interaction phenomena. The observed impurity elements can be divided into two classes according to [1]: desorbed and eroded impurities. This characterisation originates from the mechanism responsible for their production at the wall and/or the limiter.

1.1.1 Desorption

Desorption is a phenomenon whereby a substance is released from or through a surface. In fusion devices desorption can be due to heat affecting the wall (thermal desorption), or by particle and photon bombardment, or by chemical reactions between particles hitting the wall and wall elements (chemical sputtering).

In case of chemical desorption the production of impurities occur only for specific combinations of projectile-target elements. The most common of these combinations are carbon wall interacting with hydrogen plasma or oxygen impurities. In the first case there will be production of methane and hydrocarbons while in the second case carbon monoxide and carbon dioxide.

The first reaction is very common in fusion devices because carbon is widely used as a limiter and wall material due to its refractory qualities and the fact that it does not melt. However it has a chemical sputtering yields which is comparable or higher than physical sputtering yields in terms of atoms removed per incident ion or atom. Formation of hydrocarbons by interaction of hydrogen with carbon materials (graphite) depends on a variety of parameters such as the target temperature, hydrogen impact energy and flux [2]. When hydrogen atoms of thermal energy

($E \lesssim 0.2$ eV) impinge on carbon materials, several kinds of hydrocarbons can be formed. The reaction rate depends on the structure of the carbon surface layer. Crystalline graphite has a reaction rate smaller than 10^{-3} desorbed carbon atom per incident ion, but the yield increases when the surface is damaged. The highest yields (up to 10^{-1}) are obtained on amorphous carbon layers which are obtained by chemical plasma deposition [3].

In case of oxygen ions impinging with carbon materials, the reaction can lead to the formation of CO and CO_2. The overall yield ($CO + 2CO_2$)/O is near the unity [4]. These reactions cause the presence of additional carbon and oxygen impurities into the plasma.

Even in devices in which graphite limiters and/or wall are used the most abundant desorbed impurity is oxygen, with a typical concentration, relative to n_e, in the range 0.5-5% [1]. Oxygen comes from the adsorption of H_2O vapour when the machine is brought up to air, and then it is released by desorption during the discharges. Other frequent desorbed elements are carbon, nitrogen and chlorine, depending on the materials in the wall and/or the limiter.

1.1.2 Erosion

Erosion of atoms from solid surfaces is due to sputtering, unipolar arcs and evaporation.

Physical sputtering is the most important mechanism of impurity release, it occurs for all materials independently of the chemical nature, wall condition and wall temperature. Sputtering consists in the removal of atoms from the surface of a solid as a result of impact by plasma ions, charge-exchange neutrals and impurity ions. It takes place when the transferred energy from the incident particle to the lattice atom exceeds the surface binding energy.

Unipolar arcs can be formed locally due to a potential difference between the plasma and the surface of limiters or probes, and cause localised erosion of the material. The applied potential is produced by the plasma sheath and it is of the order of $\sim 3T_e$; a local electron temperature of only 5-10 eV is necessary to sustain an arc [5]. When the arc is initiated, electrons from the cathode spot are accelerated away from the surface by the sheath potential. Arcs give rise to erosion of the cathode spots. The material is released in the form of ions, neutral vapour, molten and solid drops. Arcing in fusion devices occurs normally during the current rise phase, when the plasma is unstable, and so, in long pulse length experiments, it is a relative less important impurity production mechanism.

Evaporation is linked to the material heating due to the power flux coming from the plasma. This flux, either by conduction or convection, results in localised power deposition at the limiters or in the divertor since the power transfer is predominantly along field lines. This power deposition can result firstly in evaporation of material, i.e. erosion of the surface and contamination of the plasma, and secondly in thermal shock, leading to the loss of structural strength of the components. Power can also be deposited on the walls during malfunctions, such as the occurrence of disruptions or runaway electrons.

Eroded materials are the components of the limiters and/or the wall, i.e. carbon for graphite wall devices (RFX-mod), tungsten for ITER-like wall devices (JET, Asdex Upgrade, Tore Supra), Fe, Ni, Mo (FTU), Al (MST), ... Eroded impurities are less abundant compared to desorbed ones: typical concentrations being in the 0.1-1% range [1].

1.1.3 Recycling

In most devices the pulse length is at least one order of magnitude longer than the particle replacement time. This means that on average each plasma ion goes to the target and returns to the plasma many times during the discharge. This process is called *recycling*. The particle replacement time may be defined as the ratio of the total particle content within the last closed magnetic surface to the total particle influx (and efflux) across the surface.

When a plasma ion or neutral arrives at a solid surface, it undergoes a series of elastic and inelastic collisions with the atoms of the solid. It may either be backscattered after one or more collisions, or slow down into the solid and be trapped. Trapped atoms can subsequently reach again the plasma diffusing back to the solid surface. The ratio of the flux returning to the plasma from the solid, to the incident flux, is known as the *recycling coefficient*. This recycling coefficients can be significantly greater than one in case of desorption of particles from the wall. Large quantities of hydrogen can built up in wall materials in contact with the plasma and then can be released into it, becoming a serious concern for density control. This is especially true for non-metal materials; graphite, commonly used as limiter or wall material, is porous and hydrogen can permeate into the bulk of the material and become trapped at lattice defects, with a saturation level of about 0.44 H atoms per carbon atom [6]. Carbon as a first wall material has therefore the serious problem of a high hydrogen retention. In the final design of the ITER first wall it has been rejected indeed, due to its high retention of tritium, which may become problematic due to the strict limit of the tritium inventory in the reactor.

1.1.4 Wall conditioning

Under normal vacuum conditions a surface will be covered by a layer of adsorbed gas coming from the surrounding atmosphere. The adsorbed atoms have a binding energies ranging from weakly bound physical adsorption, ~0.3 eV, to strongly bound chemical absorption ~3 eV [5]. The weakly bound species can be removed thermally and at any given temperature there will be a dynamical equilibrium between the arrival rate and the desorption rate. Although hydrogen can be absorbed on the surface, impurities species such as carbon monoxide and water molecules are the typical adsorbents, accounting for the carbon and oxygen frequently observed as impurities in fusion plasmas.

Desorption can lead to impurity accumulation in the plasma or, in the case of desorption of the plasma species, to lack of density control. In order to minimise the desorption processes various procedure have been adopted for reducing adsorption on the wall. These are frequent referred to as *wall conditioning*. They include:

- baking the vacuum vessel, typically to 200-350 °C;
- using a variety of plasma discharges to remove the adsorbed gas from the wall, known as *cleaning discharges*;
- gettering, in which the wall is covered with a clean metal film by evaporation;
- covering the wall with a low Z film such as carbon, boron or lithium, known as *carbonisation*, *boronisation* and *lithisation*.

Baking

Heating of the vacuum surfaces reduces the concentration of absorbed molecules by thermal desorption. A great limitation is that baking can only release weakly bound molecules (the main outgassing species being water vapour). So, in order to remove more tightly bound molecules, other cleaning methods are used. In any case baking can be used together with other techniques, i.e. cleaning discharge, to minimise re-adsorption of gas.

Cleaning discharge

The cleaning discharges can be of various types, such as glow discharges or pulsed discharges. In each case the aim is to optimise the removal of the adsorbed particles by energetic ions, neutrals or electrons. These processes are more effective than simple thermal desorption because more energy is transferred to the adsorbed species. Glow discharge cleaning (GDC) is the most widely used technique. Although many gases have been tested for discharge cleaning, the light ions hydrogen and helium have generally been used, as this reduces sputtering of the substrates, which can lead to thin films of sputtered material being deposited on windows and insulators. When using hydrogen, surface cleaning is enhanced by chemical action with the formation of hydrocarbons, such as CH_4 and C_2H_4, together with H_2O and CO. Since these species are volatile they can be pumped away. In systems with mainly carbon walls, GDC in helium has been found to release oxygen, usually by forming CO. Helium GDC also desorbs implanted hydrogen isotopes in the wall, thus reducing recycling. Helium atoms are not trapped in graphite at temperature above 300 K [5].

Gettering

Gettering consists in the evaporation of wires to produce layers of chemically active metals which react with active gases such as O_2, CO, H_2, and CO_2 binding them tightly to the surface. Sequential deposition results in the adsorbed gas being buried. Gettering appears to work by reducing outgassing from the substrate as well as by removing unwanted impurity species from the gas phase. Titanium, chromium and beryllium have been most widely used in tokamaks.

Carbonisation and boronisation

Coating the wall with low Z non-metallic films, such as carbon or boron, minimise the release of high Z impurities. Carbonisation is carried out introducing into the vacuum vessel a gaseous compound, typically methane, and dissociating it in a glow discharge, depositing a thin layer of amorphous carbon on the wall. The optimum wall temperature is about 300 °C. Boronisation is similar: boranes such as B_2H_4 and B_2H_6 are introduced into the vacuum vessel at 400 °C. They thermally decompose and deposit a layer of boron on the wall. Boron acts as a getter and thin boron films pump both oxygen and hydrogen.

Lithisation

Lithium has also been used in coating wall material in several devices, both tokamaks and RFPs. Lithium can be introduced into the vacuum vessel in various ways: by means of evaporators which inject streams of lithium vapour [7], using a liquid lithium limiter employing a capillary

porous system [8] or injecting solid lithium pellets [9]. In any way lithium gets deposited on the first wall surface and reduces recycling of hydrogen leading to improved operating performance. They include better control of the plasma density, decrease in inductive flux consumption and increase in the electron temperature, ion temperature and energy confinement time [7].

All the coating techniques using the plasma itself (carbonisation, boronisation and lithisation) lead to inhomogeneous layer deposition because the ionised species are guided by the magnetic field. Furthermore, boron has the practical disadvantage of being explosive and highly toxic while lithium is highly reactive and flammable.

Successful wall conditioning removes impurities and generally results in access to a much wider range of operating conditions. In particular it allows higher densities to be obtained without excessive radiation. Higher densities in themselves tend to reduce the impurity concentration because, for a given power input, an increase in density reduce edge temperature and hence sputtering yields.

1.2 Impurity effects

The impurities have profound effects, some deleterious and some beneficial, on the plasma, justifying extensive experimental and theoretical work towards understanding impurity transport and effects in the plasma, impurity production mechanisms and towards developing schemes for reducing impurity influxes and removing impurities from the plasma.

One of the most important effects of impurities is their contribution to the energy balance through their radiation losses. Especially dangerous are heavy impurities, since they are incompletely stripped over the entire plasma and radiate strongly. As the impurity concentration increases, there is a point at which all the input power will be radiated away. For this reason, high Z impurities must be kept away from any high-temperature plasma.

On the other hand, the radiative role of light impurities is significantly different. Light impurities are ionised and radiate predominantly at the plasma periphery; this is not necessarily a deleterious effect, since low Z ion radiation at the plasma edge helps in transferring the plasma energy rather harmlessly to the wall. Moreover, they also cool the edge and force the current density (and hence the temperature and power input) distribution to become more centrally peaked, thus reducing the influx of high Z impurities, presumably by reduced sputtering. However, even light impurities if present in high concentration may prevent the plasma being heated, especially during the start-up phase, when the walls are covered with adsorbed gas, the various desorption processes can lead to high levels of radiation from oxygen and carbon.

Further problems arising from impurities in a fusion device are changes in collisional transport coefficients across the confining magnetic field, reduction of the penetration of neutral beams (used for additional heating) due to the large cross sections for electron capture by highly stripped impurities for hydrogen isotopes, and, in a fusion reactor, the fuel dilution, i.e. for a given total particle density, there is a displacement of reacting ions by the large number of electrons produced by the impurities. Generally, as the impurity content increases, confinement and stability decrease and instabilities (including major disruptions in tokamaks) develop progressively at lower n_e and I_p values.

Impurities also affect the plasma by determining the *effective charge*

$$Z_{\text{eff}} = \sum \frac{n_z Z^2}{n_{\text{e}}} \tag{1.1}$$

where the sum is over all the existing ions of charge Z and density n_z. Z_{eff} enters into the formula for the plasma resistivity, i.e. it plays a role in shaping the plasma current and, consequently, the input ohmic distribution. In this context, low Z impurities are the worst offenders, since the lower density of high Z impurities does not usually affect significantly the plasma resistivity.

1.3 Plasma radiation

The presence of impurities in the plasma produces energy losses through radiation. There are two types of process involved. The first is the enhancement of bremsstrahlung because of the higher value of the ionic charge for impurities. The second is the radiation which occurs through the atomic processes of line radiation and recombination.

1.3.1 Continuum radiation

Continuum radiation is emitted by plasmas as a result of free-free and free-bound radiation. Free-free transitions (bremsstrahlung) are due to the interaction of electrons with positively charged ions of charge Z and density n_z; neglecting a correction factor (the Gaunt factor), the free-free spectral power density, for a Maxwellian electron distribution at a temperature T_{e}, is given by

$$I_\nu \sim \bar{Z}^2 \frac{n_{\text{e}} n_z}{T_{\text{e}}^{1/2}} \exp(-h\nu/T_{\text{e}}) \tag{1.2}$$

[10, 11]. $\bar{Z}$ is the effective charge for bremsstrahlung emission, which is generally different from Z, due to the partial screening of the nuclear charge Z_N, by the $(Z_N - Z)$ electrons [12]. Relationship 1.2 shows that the logarithmic slope of the spectrum gives the electron temperature T_{e}. When the electron distribution function is not Maxwellian, it is in principle possible to deconvolute it from the high photon energy non-thermal spectrum (since free-free radiation is very sensitive to high-energy tails).

In free-bound (recombination) radiation, a free electron (kinetic energy E_{e},) is captured by an ion of charge Z in a bound level n of the ion of charge (Z - 1) (ionisation energy χ^n_{Z-1}) and a photon of energy $h\nu = E_{\text{e}} + \chi^n_{Z-1}$ is emitted. The photon energy is a function of E_{e}, but only photons with $h\nu > \chi^n_{Z-1}$ are emitted. The spectra therefore show discontinuities, generally called recombination edges. Above the edges, the spectral dependence is the same as for free-free radiation, and T_{e}, can therefore again be deduced from the logarithmic slope. Non-thermal electrons do not contribute to the free-bound spectrum, since the recombination cross section decreases rapidly for $E_{\text{e}} \gg \chi^n_{Z-1}$ [12].

As an example, Fig. 1.1 shows the theoretical emission spectrum of a Maxwellian plasma in which $T_{\text{e}} = Z^2 R_y$, where R_y is the Rydberg energy (13.6 eV). Significant steps occur at the recombination edges $\hbar\omega = Z^2 R_y / n^2$, where the next level begins to participate.

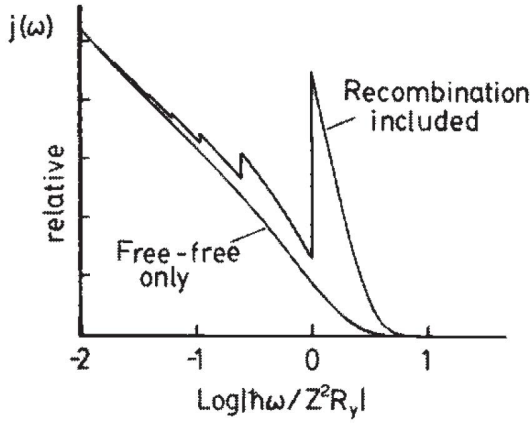

Figure 1.1: Emissivity of a plasma, illustrating the addition of recombination to the free emission spectrum [13].

1.3.2 Line radiation

Line radiation is emitted by radiation decay of ion or atom excited states. The emissivity of a spectral line, i.e. number of photons emitted per unit time and per unit volume, is equal to $A_{ji}n_{\rm exc}$, where $n_{\rm exc}$ is the population density of the emitting upper state and A_{ji} the transition probability. Thus, the calculation of spectral lines intensities is more complicated than continuum radiation since account has to be taken of the processes by which the upper level of the transition is populated. For the interpretation of line emission, the excited level population must, therefore, be known. It turns out also that spectral line radiation often contributes the largest fraction to the total radiated power loss, especially in the presence of high Z incompletely stripped impurities. Moreover, line radiation offers an important method of identification of the impurities from the characteristic wavelengths of the radiation.

1.3.3 Total radiated power

The total radiated power may be found by adding and integrating the radiation from the various processes described above. From the experimental point of view, this requires measurement of the absolute intensity of all spectral lines (plus continuum) emitted in the entire spectrum: this is carried out by the bolometer diagnostic [14]. From a simulating point of view, the total plasma emission is obtained through the use of a model, for example assuming that the plasma obeys the coronal model approximation (see Section 1.5.1). Fig. 1.2 shows the radiation losses for several elements often found in fusion devices, assuming coronal equilibrium. Note that radiation losses decrease with increasing electron temperature, a consequence of the stripping of impurities to higher, less radiating, charge states; when the ions are fully stripped only bremsstrahlung radiation remains. Note also that, at a given electron temperature, radiation losses increase with increasing nuclear charge, thus emphasising the importance of high Z impurities.

For low Z impurities such as carbon or oxygen the maximum radiation occurs at very low temperature, of the order of tens of eV. The ions of these impurities are fully stripped at a temperature of 1 keV and in the hot plasma of a medium size fusion device they would only radiate through bremsstrahlung. At the plasma edge radiation losses arise from the incompletely

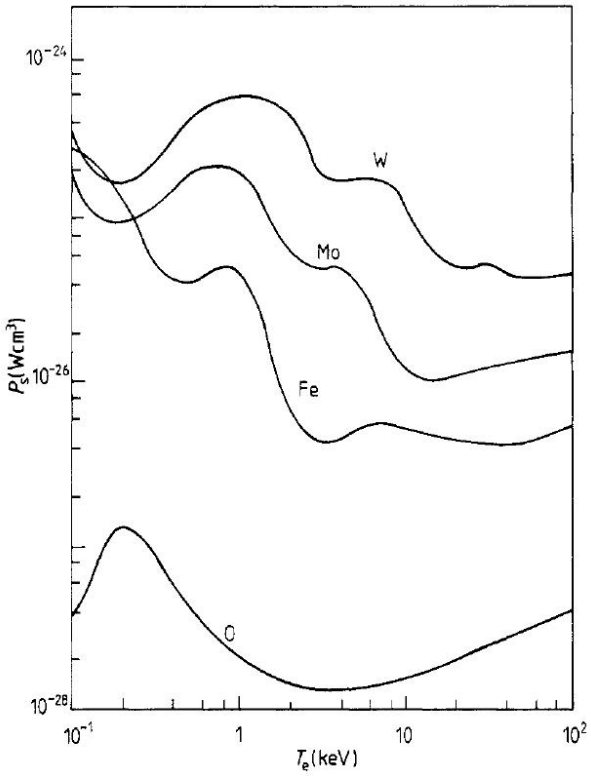

Figure 1.2: Total radiation losses at corona ionisation equilibrium for several elements as function of electron temperature [15].

stripped impurities which enter the plasma as neutral atoms. For high Z impurities, typically the metals of which the device is constructed, the first maximum in radiated power occurs at a somewhat higher temperature. For temperatures above 100 eV the radiation per ion is much greater than for low Z impurities. Even at reactor temperatures these ions are not fully stripped and the radiated power is such that the level of high Z impurities must be very small.

These calculations have been performed at ionisation equilibrium, that is the charge-state distribution at steady-state; however, if impurity diffusion processes are important, the charge-state distribution, and consequently the total radiation losses, are considerably altered. These effects will be discussed in Section 1.6.

1.4 Atomic physics and fusion plasmas

We shall now describe the atomic physics processes of interest in the distribution of ions among different ionisation states and the exited level populations of different ions. The electron processes of importance are generally:

1. Radiative processes
   (a) transitions between bound states;
   (b) free-bound transitions: recombination/photoionisation.

2. Collisional processes

   (a) electron impact excitation/deexcitation;

   (b) impact ionisation/three-body recombination;

   (c) dielectronic recombination/autoionisation.

1.4.1 Radiative processes

Transitions between two energy levels (i, j) of a particular atomic species can be made in three distinct ways. First, an atom with the electron in the upper level, energy E_i say, can decay spontaneously to the lower level E_j with the emission of a photon whose frequency is ν_{ij}:

$$h\nu_{ij} = E_i - E_j \tag{1.3}$$

The probability per unit time for this transition is the spontaneous transition probability, denoted A_{ij}. Second, an atom with the electron in the lower level may absorb a photon by a transition to the upper level. If the energy density per unit frequency of electromagnetic radiation at the atom is $\rho(\nu)$, then the probability of absorption per unit time is written $B_{ji}\rho(\nu_{ij})$. Third, induced decay from E_i to E_j can occur due to the presence of the radiation. The probability of this event per unit time is written $B_{ij}\rho(\nu_{ij})$. The numbers A_{ij}, B_{ij}, B_{ji} are called the Einstein coefficients for this transition. They are related by certain identities that can readily be deduced from fundamental thermodynamics. See [13] for the respective expressions.

Radiative recombination has already been introduced in Section 1.3.1. The inverse of this recombination is photoionisation: the absorption coefficient is important above the ionisation potential and decreases as ν^{-3}. Photoionisation is important for high-energy electrons ($h\nu > T_e$).

1.4.2 Collisional processes

Excitation and ionisation of positive ions are mainly caused by electron collisions. The collisional processes 2(a) and 2(b) correspond to the radiative ones [l(a) and l(b)] except that the transitions are induced by electron collisions and there is no spontaneous decay. Three-body recombination is the inverse process of impact ionisation (the non-recombining electron carrying away the excess energy and momentum).

Dielectronic recombination is a three-step process: the incident electron is resonantly captured by the recombining ion in a level with large principal quantum number, the excess energy being spent in the excitation of a bound electron. Subsequently, the doubly excited recombined ion can radiationless autoionise (either in the ground state or in an excited state of the recombining ion), or be radiatively stabilised below the ionisation potential by emission of a photon (generally by the initially bound electron, at a wavelength slightly different from that of the recombining ion, due to the presence of the "spectator" captured electron). In this second case, one is dealing with a recombination process, since a level of the recombined ion below the ionisation limit is reached. The collisional processes are usually described by individual cross sections $\sigma_{ij}(v)$ (for any specific processes $i \rightarrow j$).

For electron densities obtained in magnetic fusion experiments ($n_e \lesssim 10^{20}$ m^{-3}) the dominating recombination processes are radiative and dielectronic recombination.

Finally, a further recombination process is charge-exchange recombination with neutral hydrogen isotopes. This is a mechanism by which a bound electron is transferred or exchanged between two atoms in a collision. Under normal circumstances the influence of charge exchange upon the excited states is very low because for hot plasmas the number of neutrals is much less than the number of electrons (which are responsible for the competing collisional processes). In special cases however, in which neutral density reaches high values, charge-exchange effects can be important, for example when neutral beams are deliberately injected into the plasma either for plasma heating (NBI) or for diagnostics (charge-exchange recombination spectroscopy). In this circumstances the ionisation stage of highly ionised impurities can be significantly depressed by charge-exchange recombination.

1.5 Types of equilibria

1.5.1 The ionisation equilibrium

An impurity atom is ionised by electron impact to successively higher charge states as it penetrates progressively into the discharge (where it finds an increasing electron temperature). The radial velocity of this movement perpendicular to the field lines is much smaller (of the order of the limiter radius divided by the confinement time, i.e. typically 10 m/s) than the thermal velocity of the unimpeded movement along the magnetic field line (having typical values larger than 10^3 m/s), which leads rapidly to a uniform spread over the magnetic surfaces. For this reason the impurity ion emission is generally uniform around the torus. After the initial breakdown phase, as a consequence of the centrally peaked electron temperature profile, low and intermediate ionisation potential ions are located in shells having thicknesses of a few centimetres; the charge-state distribution progresses continuously from low degrees of ionisation at the periphery to higher ionisation states at the centre. On the other hand, central ions, existing in a region where the electron temperature is often flat, are peaked and have half-width thicknesses of several centimetres. The position of these shells depends only on the electron temperature profile, provided that impurity diffusion effects can be neglected; the impurity ions are then at *ionisation equilibrium*. The peak of the density profile of a given ion always occurs at the same electron temperature, $T_e \cong (\frac{1}{3} - 1)\chi_z$ (χ_z is the ionisation energy), and therefore as T_e increases the shell position moves outwards [1].

The calculation of the equilibrium populations of the atomic states would require the solution of a complex system of rate equations, describing the population and depopulation of all levels by the processes described in the preceding section, i.e. ionisation, recombination, collisional excitation and deexcitation, radiative decay and absorption (both for line and continuum radiation), and possibly also stimulated emission. A given charge state is connected with its two neighbouring states by ionisation and recombination. We can write simultaneous equations for all states i that set the total rate of transitions to and from that state equal to zero:

$$0 = \sum_{j \neq i} \left[n_i A_{ij} - n_j A_{ji} + (n_i B_{ij} - n_j B_{ji}) \rho(\nu_{ij}) + n_e n_i \langle \sigma_{ij} v \rangle - n_e n_j \langle \sigma_{ji} v \rangle \right] \tag{1.4}$$

where the sum j is over all other states (including free-electron states) accessible to the state i by all types of transitions. For compactness of notation we include three-body recombination as a rate coefficient even though the coefficient is then proportional to n_e [13].

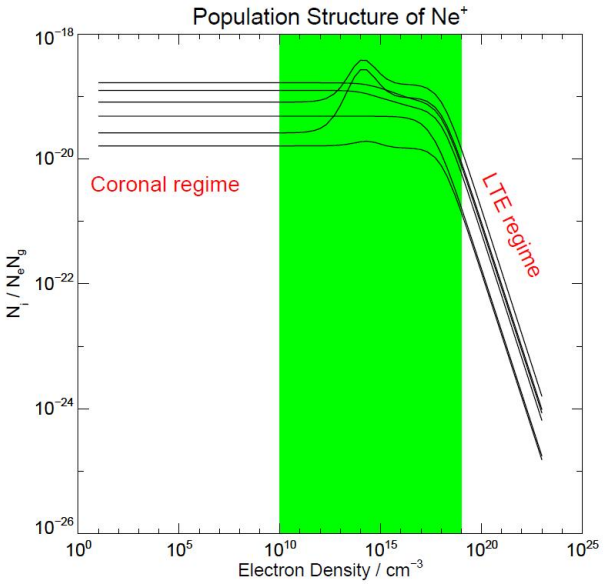

Figure 1.3: Population structure of Ne^+ as a function of electron density. Between the two extremes (Coronal and LTE) there exists a more complicated regime, the collisional-radiative regime. For many ions this is right at fusion plasma densities [16].

To solve this system of equations, even for simple atoms, requires some sort of simplifying assumptions, since the number of equations is (effectively) infinite. The approach normally adopted, even when all transition processes are retained in the equations, is to truncate the system at some high level, ignoring transitions to or from all higher levels. This works rather well in many cases because the populations of the higher levels are often very small. The system is thus reduced to a finite matrix system that may be solved numerically given all the appropriate coefficients. Its resolution allows the charge-state distribution at steady-state to be obtained (the ionisation equilibrium, IE). The results are usually expressed by means of the fractional abundances $f_z = n_z / \sum n_z$ of the ions of charge z as functions of n_e and T_e (n_z is the total ion density, i.e. the sum of excited plus ground state densities). Due to the difficulty of solving the full problem, further approximations are generally used (in order of increasing n_e value, see Fig. 1.3): the corona equilibrium (CM), the collisional-radiative model (CRM) and local thermodynamic equilibrium (LTE).

1.5.2 Coronal equilibrium

At low densities a rather simple model may be used, which acquires its name from its applicability to the solar corona. In coronal equilibrium the fundamental approximation is that all upward transitions are collisional (since the radiation density is low) and all downward transitions are radiative (since the electron density is low). Let's explain better this assumption: upward radiative transitions (i.e., absorption) use up a photon that was presumably emitted by the same transition (downward) in an atom elsewhere in the plasma. Therefore, if the plasma is optically thin, so that most photons simply escape without being reabsorbed, then upward radiative transitions will be negligible compared with downward. On the other hand, the rate at which an excited state is depopulated by spontaneous downward transitions is independent of density. Therefore, if the

electron density is low enough, the rate of collisional deexcitation becomes negligible compared with spontaneous emission. Moreover, if an excited state can be populated by collisional excitation from the ground state, this process is the dominant one, so that the excited state population is determined by balancing this excitation against radiative deexcitation:

$$\frac{n_i}{n_1} = \frac{n_e \langle \sigma_{1i} v \rangle}{\sum_j A_{ij}} \tag{1.5}$$

Ionisation/recombination balance is governed by collisional ionisation and recombination, and again essentially only the ground state is important because of its dominant population. Two neighbouring ionisation states, of charge z and $(z + 1)$, are then connected by

$$n_z n_e S_z(T_e) = n_{z+1} n_e \alpha_{z+1}(T_e, n_e)$$

or

$$\frac{n_z}{n_{z+1}} = \frac{\alpha_{z+1}(T_e, n_e)}{S_z(T_e)} \tag{1.6}$$

where we have neglected charge-exchange recombination. S_z and α_{z+1} are the ionisation and recombination rate coefficients, respectively. Relationship (1.6) is, to a first approximation, independent of n_e (it only depends on n_e through the dielectronic part of the recombination rate coefficient).

This model requires that the electron density be sufficiently low for collisions not to interfere with radiative emission. This condition is generally satisfied in fusion devices. However, as n_e increases, de-population with total collision rate Q_j^* starts to interfere with radiative decay; at a critical density such that $\sum_{r<j} A_{jr} = n_e Q_j^*$, the CM approximation fails for the level j. This limit condition (since A_{jr} decreases, whereas Q_j^* increases with principal quantum number n) implies that it always exists a limit level n_T such that for $n > n_T$ collisions dominate. Above n_T, LTE with the neighbouring higher ionisation state is assumed. A rough estimate of this limit can be obtained for hydrogen-like ions taking j=6: CM requires that [12]

$$n_e < 5.9 \times 10^{16} Z_N^6 T_e^{1/2} \exp\left(\frac{10^{-1} Z_N^2}{T_e}\right) \tag{1.7}$$

(m^{-3}, eV). For instance, taking $Z_N = 6$ and $T_e = 1200$ eV, this limit will be of the order of 10^{23} m^{-3}, much higher than normal fusion densities. So, CM approximation is sometimes applied to fusion plasmas for describing impurity abundances, nevertheless it is a inaccurate model, especially because it does not consider radial transport phenomena, which greatly modify impurity distribution. Indeed, it is a general observation that for low ionisation potential light ions the electron temperature of maximum abundance is always higher than the corresponding temperature at CM. At a given radius, therefore, light atomic species are less ionised than at CM, a consequence of their inward movement [1].

Moreover, in some isoelectronic sequences excited levels can have a non negligible population with respect to the ground state (even at low densities); they are called *metastable states*, since they can decay to the ground state only through low A_{jr}, non-allowed, transitions. In these cases, the CM must always be suitably modified.

It has already been pointed out that the IE in Eq. (1.6) does not include the charge-exchange recombination mechanism, which can become important in the presence of high neutral hydrogen (or deuterium) densities. This additional recombination process is particularly important for H- and He-like ions (and partially also for Li-like ions), for which radiative recombination is the dominant electron ion recombination mechanism. The (mostly radiative) recombination rates of these ions are typically smaller than the (mostly dielectronic) recombination rates of lower-charge state ions at their corresponding temperatures of maximum abundance, and they are, therefore, more sensitive to added contributions. Moreover, charge-exchange cross-sections are increasing functions of the ion charge. The main effect of this additional recombination mechanism is that stripping of impurities to high (relatively non-radiating) ionisation states with increasing electron temperature can be postponed or entirely prevented when a high neutral hydrogen (deuterium) density n_{n} is present. Equation (1.6) must then be written

$$n_z S_z = n_{z+1}(\alpha_{z+1} + \frac{n_{\mathrm{n}}}{n_{\mathrm{e}}}\alpha^{\mathrm{cx}}_{z+1}) \tag{1.8}$$

($\alpha^{\mathrm{cx}}_{z+1}$ being the charge-exchange rate coefficient) and now depends on the $n_{\mathrm{n}}/n_{\mathrm{e}}$ ratio. Relatively low $n_{\mathrm{n}}/n_{\mathrm{e}}$ ratios (of the order of $10^{-6} - 10^{-5}$) are sufficient to considerably lower the ionisation equilibrium of the highest-charge states.

1.5.3 Local thermodynamic equilibrium

The approximation opposite to the CM is the local thermodynamic equilibrium model (LTE). In this approximation, it is assumed that the distribution of population densities is determined only by particle collision processes taking place with sufficient rapidity for the distribution to respond instantaneously to any change in plasma conditions. As a consequence, each process is accompanied by its inverse, and these pairs of processes occur at equal rates by the principle of detailed balance. The distribution of population densities of the energy levels is, therefore, the same as it would be in a system in complete thermodynamic equilibrium.

The level populations of an ion are determined by the Boltzmann equation

$$\frac{n_j}{n_i} = \frac{w_j}{w_i}\exp\left(-\frac{\Delta E_{ji}}{kT_{\mathrm{e}}}\right) \tag{1.9}$$

where w is the statistical weight (the number of degenerate states in a particular level). For a Maxwellian distribution of free electrons, the charge state is determined by the Saha equation

$$n_{\mathrm{e}}\frac{n_{z+1}}{n_z} = 2\frac{w_{z+1}}{w_z}\left(\frac{2\pi m_{\mathrm{e}} kT_{\mathrm{e}}}{h^2}\right)^{3/2}\exp\left(-\frac{\chi_z}{kT_{\mathrm{e}}}\right) \tag{1.10}$$

where the populations n_{z+1} and n_z are at the ground level and χ_z is the ionisation energy.

To achieve LTE generally requires high enough density for collisional transitions to dominate radiative transitions between all states; otherwise, the absence of thermal radiation will cause deviations from the thermal populations. The conditions for LTE to be satisfied (less than 10% deviation) is [17]

$$n_{\mathrm{e}} \geq 1.8 \times 10^{20}\, T_{\mathrm{e}}^{1/2}\Delta E_{ji}^3 \tag{1.11}$$

(m^{-3}, eV). This criterion must be satisfied for the largest energy level difference in the level scheme. For instance, if the largest transition has an energy difference of 1200 eV with equal electron temperature, the limit density will be of the order of 10^{31} m^{-3}. These densities are never achieved in fusion plasmas and so this model is never used. LTE model is instead applied in laser-produced plasmas.

Calculations for LTE are relatively easy to implement as a consequence of the relatively low importance of atomic data; for given n_e and T_e values, line intensities can be calculated from a knowledge of ionisation potentials, excitation energies and transition probabilities. Note that the IE here depends on the n_e value (at given T_e, the average charge state decreases as n_e increases).

1.5.4 Collisional-radiative model

In the intermediate density range neither of the two previous approximations can be safely used, and a full collisional-radiative (CR) model is necessary.

The CR model solves a set of collisional-radiative equations which determine the populations of the emitting ions in a plasma. These equations consist of a set of time-dependent differential equations with one equation for each level i in every ion stage of the model. That is,

$$\frac{dn_i}{dt} = \sum_j C_{ij} n_j \tag{1.12}$$

where the summation on the right-hand side extends over all levels of all ion stages. The terms in the collisional-radiative matrix C_{ij} represent the contributions from all collisional and radiative processes (i.e., collisional excitation and deexcitation, collisional ionisation and three-body recombination, autoionisation and dielectronic capture, photoexcitation and radiative decay, and photoionisation and radiative recombination).

Often, the assumption of *quasi-static equilibrium* is made in order to simplified the system [18]. This assumption naturally divides the levels into two categories: the metastable levels (including the ground state) that are relatively long lived and the excited levels, which comprise the remaining levels. Physically, the quasistatic approach means that the excited level populations within an ion stage are considered to be in instantaneous equilibrium with the metastable levels of the element under consideration. Mathematically, this approach requires that the time derivatives for all of the excited level populations in Eq. (1.12) be set to zero, while those for the metastables must be solved directly. The metastables are assumed to contain a large majority of the population within a given ion stage and so a determination of these populations will provide the ionisation balance of the system. On the other hand, a determination of the excited level populations is required for spectral quantities, such as the radiated power loss.

The result is a system of equations that is divided into two pieces: the ionisation balance calculation, which determines the metastable populations, and the excited level population calculation, which requires as input the metastable populations from the previous calculation. The time-dependent metastable populations can be taken in from other codes, such as plasma transport codes. The excited populations may then be obtained from these data at each time interval for which the metastable populations have been provided (we shall see in the next chapter that the code used in this thesis is actually a CR code coupled to a transport code).

At ionisation equilibrium the total ion densities of two successive ionisation states of charge z and $(z + 1)$ are connected by

$$n_z S_z = n_{z+1}(\alpha_{z+1} + n_e \beta_{z+1} + \frac{n_n}{n_e}\alpha^{cx}_{z+1}) \tag{1.13}$$

where S_z is the ionisation rate coefficient, α_{z+1}, β_{z+1} and α^{cx}_{z+1} are the recombination (radiative plus dielectronic), three-body recombination and charge-exchange rate coefficients, respectively. Three-body recombination dominates at high densities, when n_z/n_{z+1}, tends to the Saha equation value. At low electron densities, on the other hand, this term is negligible, and relationship (1.13) tends to (1.8) (and, moreover, excited state populations become negligible with respect to the ground-state population).

1.6 Impurity transport

In situations where impurity diffusion processes cannot be neglected (i.e. if diffusion times are shorter than the relevant atomic-process characteristic times), the results of charge-state distribution calculations are considerably modified. In the general case, one has to use the full diffusion theory of impurities, coupling a code describing the charge-state distribution for given n_e and T_e values, to a transport code describing the impurity fluxes according to the plasma evolution.

The continuity equations to be solved for the ions of charge z and density n_z of the species with atomic number Z_N are

$$\begin{aligned} &\frac{\partial n_z}{\partial t} = -\frac{1}{r}\frac{\partial}{\partial r}(r\Gamma_z) + S_{z-1} n_e n_{z-1} - ((S_z + \alpha_z)n_e + \alpha^{cx}_z n_n)n_z + (\alpha_{z+1} n_e + \alpha^{cx}_{z+1} n_n)n_{z+1} \\ &z = 0, 1, \ldots, Z_N \end{aligned} \tag{1.14}$$

where Γ_z is the radial particle flux density (positive when directed outwards), S_z is the ionisation rate coefficient, α_z the recombination rate coefficients (radiative + three-body + dielectronic) and α^{cx}_z the charge-exchange rate coefficient. n_n is the hydrogen (deuterium) neutral density. n_z is here expressed in cylindrical coordinates and has been averaged over a flux surface, which is equivalent to assuming poloidal and toroidal symmetry.

Generally speaking, this system should be used together with all the other plasma physics equations (the magnetohydrodynamic (MHD) system), which determine the time evolution of the plasma macroscopic parameters. This is a quite complicated and expensive procedure. A simplification is therefore generally used by decoupling the MHD system from system (1.14), i.e. specifying $n_e(r)$, $T_e(r)$ and $T_i(r)$ profiles (possibly including their time variations), thus considering impurity transport in a known background plasma. The principal advantage of using the measured density and temperature profiles is to separate as much as possible impurity transport effects from uncertainties in the transport of the background plasma. One disadvantage is, however, that this limits the validity of these calculations to conditions where the impurity density is small compared to the main plasma density. However, this is not especially restrictive, since most present fusion devices satisfy this condition. Even with this simplification, the number of equations in the impurity system can be very large (for high-Z elements) and the system solution is quite heavy. Thus, the system is very often only solved for light impurities. For heavier

species, like tungsten, superstage treatment is applied [19]: the number of working populations is reduced to less than Z with each such population consisting of a "bundle" of contiguous ionisation stages - called a "superstage". The base model of the superstage description is that the ions bundled in each superstage are constrained to be in coronal equilibrium between each other. From the numerical point of view, the treatment of a heavy impurity in superstages cuts down the number of equations to be solved.

For the impurity flux Γ, in the system (1.14), theoretical formulations must be used. For the species j, this flux is driven by the radial gradients $\partial n_j/\partial r$ and $\partial T_j/\partial r$, being related to them by a matrix of coefficients. Thus, if the fluxes for each species depend only on the gradients for that species, the equations for the flux can be written

$$\Gamma_j = -\alpha_{11}\frac{\partial n_j}{\partial r} - \alpha_{12}\frac{\partial T_j}{\partial r} \tag{1.15}$$

The diagonal elements of the matrix are the diffusion coefficients D_j, which have different expression depending on the theory used to describe the transport. These will be depicted in the next section.

The radial flux of charged impurities is accompanied by an incoming flux of neutral atoms from the wall. This neutral influx can be deduced at steady-state from the intensity of a given spectral line [20]:

$$\Gamma_0 = 4\pi\frac{S_0}{X_0\mathcal{B}_0}I_0 \tag{1.16}$$

where I_0 is the measured intensity of a line of excitation rate X_0 and branching ratio $\mathcal{B}_0$. S_0 is the ionisation rate. The branching ratio can be defined as the portion of electronic transitions that are made from a particular upper level down to a specific lower level divided by the total amount of electronic transitions from the same upper state to any lower level. Branching ratio from level i to j is then given by

$$\mathcal{B}_{ij} = \frac{A_{ij}}{\sum_k A_{ik}} \tag{1.17}$$

The necessary ratios $S/X\mathcal{B}$ in Eq. (1.16) are normally determined from known ionisation and excitation rates, which have been either deduced from experiments or calculations. In other cases a CR model has to be set up which calculates the population of the excited levels from a set of rate equations.

1.6.1 Classical and neo-classical transport

Let us consider, to start with, a pure plasma consisting of electrons and hydrogen ions. Classical transport (which gives the minimum level of "leakiness" from a confinement system) results from binary Coulomb collisions, causing the particle guiding centres to move from one orbit centred on a given magnetic surface to another orbit centred on a neighbouring magnetic surface. In a straight magnetic field, the step size is the gyration radius ρ and the diffusion coefficient is

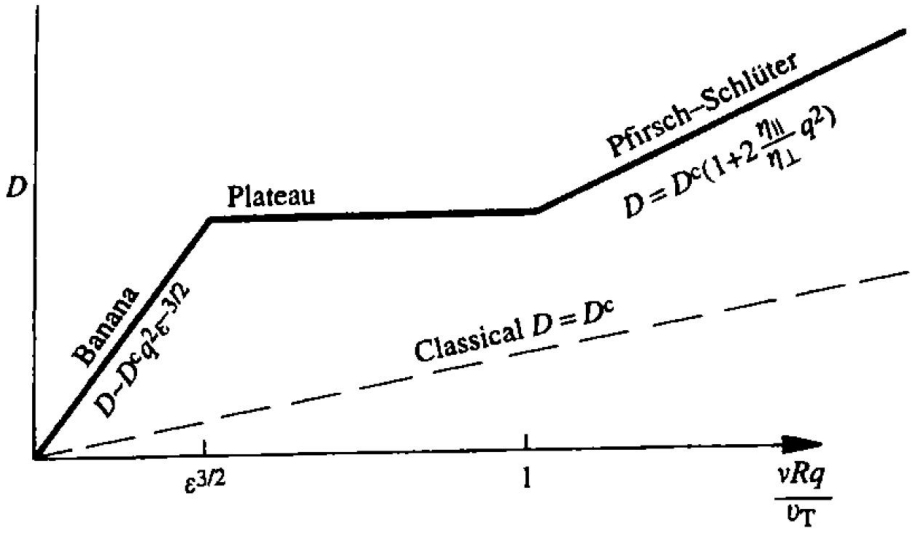

Figure 1.4: Variation of neo-classical diffusion coefficient with collision frequency. $\varepsilon = a/R$ is the inverse aspect-ratio. [5]

of the order of $\nu\rho^2$ where ν, is the 90° scattering collision frequency. However, in a toroidal geometry the particle orbits involve excursions away from a magnetic surface considerably larger than the gyration radius. In particular, trapped particles not making a free toroidal revolution make "banana" orbits, having a width considerably larger than ρ. As a consequence, transport is enhanced over the classical value. Cross-field transport of this type, in which non-local properties of the magnetic configuration play a role in determining the transport coefficients, is called "neo-classical" transport. The main outcome is that the transport matrix (1.15) has different expressions depending on the collision frequency value.

The lowest collision frequency regime is the collisionless, or "banana", regime, in which several complete orbits are traced out before collisional scattering occurs; in this regime the diffusion coefficient is a factor $(a/R)^{-3/2}q^2$ larger than the classical value [21].

As the collision frequency increases, collisions become too frequent to permit a trapped particle to complete its banana orbit, but typical untrapped particles still make many transits around the torus before colliding with another particle. This is called the "plateau" regime, since the diffusion coefficient is here independent of collision frequency [22].

At higher collisionality, collisions become too frequent for even an untrapped particle to complete a single transit around the torus before colliding. This is called the "collisional" or "Pfirsch-Schlüter" regime, having a diffusion coefficient a factor of $\sim q^2$ larger than the classical value [23].

Fig. 1.4 displays the variation of neo-classical diffusion coefficient with collision frequency for these three regimes at large aspect-ratio ($R/a \gg 1$).

Both electrons and ions diffuse across the magnetic field by these neo-classical processes. However, the diffusion coefficient for ions is larger than that for electrons by a factor of the order of $(m_\mathrm{i}/m_\mathrm{e})^{1/2}$ in all three regimes. Charge neutrality must, of course, be preserved. However, due to the constraint of momentum conservation for ion-ion collisions, no ambipolar radial electric field is necessary and the overall particle diffusion coefficient is of the order of the electron diffusion coefficient.

When more than one atomic species is present (the impurity problem), classical and neo-classical theories must be modified, because of the friction between the various different ion components. Since the collision frequency of ions with impurities can greatly exceed that for ions with electrons, such collisions can induce a corresponding greater impurity flux and an opposite directed ion flux. This will modify the impurity density profile until the frictional forces vanish.

In classical theory, the ion component with higher Z, feels a frictional force that causes it to concentrate near the centre of the discharge or, more precisely, near the location where the density of the lower Z, component (e.g. hydrogen) is maximum (a consequence of the ambipolarity of the ion particle fluxes, which transports inwards impurity ions as the hydrogen ions diffuse outwards due to collisions with them, in such a way that there is no net transport of charge). This tendency persists in neo-classical theory, and moreover the rate of inward impurity transport tends to be greater.

We shall now calculate the impurity radial fluxes for the classical and neo-classical cases and the resulting estimates for the impurity density profiles at the steady-state.

Classical impurity radial flux

Let the plasma be composed of electrons, primary single charged ions i ($Z_\mathrm{i} = 1$) and multi-charged ions z. The radial impurity flux Γ_z for the impurity species of charge Z due to collision with main ions is given by [24]

$$\Gamma_z^{\mathrm{cl}} = \frac{\nu_{\mathrm{i}z}\rho_\mathrm{i}^2 n_\mathrm{i}}{2Z}\left[\frac{1}{n_\mathrm{i}}\frac{\partial n_\mathrm{i}}{\partial r} - \frac{1}{Zn_z}\frac{\partial n_z}{\partial r} - \left(\frac{1}{2}+\frac{1}{Z}\right)\frac{1}{T}\frac{\partial T}{\partial r}\right] \tag{1.18}$$

where

$$\nu_{\alpha\beta} = \frac{16\pi^{1/2}}{2^{3/2}3} n_\beta \ln\Lambda \left(\frac{T}{m_\alpha}\right)^{1/2}\left(\frac{Z_\alpha Z_\beta e^2}{4\pi\varepsilon_0 T}\right)^2 \tag{1.19}$$

is the collision frequency between species. ρ_i is the ion gyro radius. $\ln\Lambda$ is the Coulomb logarithm (for its precise calculation see Appendix of Ref. [5]). Assuming $m_z \gg m_\mathrm{i}$ and $T_\mathrm{i} = T_z = T$ as a consequence of the short equipartition time.

In Eq. (1.18) the term proportional to $\partial n_z/\partial r$ is the diffusion flux which tends to flatten the impurity density profile. The term proportional to $\partial n_\mathrm{i}/\partial r$ typically corresponds to a radially inward component of main ion flux, causing a steepening of the impurity density profile. The term proportional to $\partial T/\partial r$ is normally positive in the classical case, corresponding to an outward flux. A balance between these opposing forces leads to an equilibrium profile, obtained by setting the radial flux equal to zero:

$$\frac{n_z(r)}{n_z(0)} = \left(\frac{n_\mathrm{i}(r)}{n_\mathrm{i}(0)}\right)^Z \left(\frac{T_\mathrm{i}(r)}{T_\mathrm{i}(0)}\right)^{-\frac{Z}{2}-1} \tag{1.20}$$

Thus, in the absence of temperature gradients, the impurities would be relatively peaked at the magnetic axis. The presence of the thermal gradient term, however, opposes the inward flux of impurities (at least for the normal case $\partial T/\partial r < 0$) if the density of primary ions grows slower

than $T^{(Z_I+2)/2(Z_I-1)}$. This can screen the impurities from accumulating in the discharge and it is generally called the *temperature screening effect*.

Equation (1.18) provides the flux of impurity ions due to collisions with the main ions only. Collisions with other impurities could, in principle, significantly modify impurity transport. Let us now consider a fully ionised multi-species plasma of electrons, main ions and several species of ions in different charge states. We shall assume all species and main ions to have the same temperature profile. The radial flux of the particle of species α due to collisions with main ions and other impurity ions will be [25]

$$\begin{aligned}\Gamma_\alpha^{\mathrm{cl}} =& n_\alpha \rho_\alpha^2 \sum_\beta \left(\frac{m_\beta}{m_\alpha + m_\beta}\right)^{1/2} \nu_{\alpha\beta} \left\{ \frac{Z_\alpha}{Z_\beta n_\beta} \frac{\partial n_\beta}{\partial r} - \frac{1}{n_\alpha} \frac{\partial n_\alpha}{\partial r} + \right. \\ & \left. - \left[1 - \frac{Z_\alpha}{Z_\beta} + \frac{3}{2} \frac{m_\beta}{m_\alpha + m_\beta} \left(\frac{m_\alpha Z_\alpha}{m_\beta Z_\beta} - 1\right)\right] \frac{1}{T} \frac{\partial T}{\partial r} \right\}\end{aligned} \tag{1.21}$$

We note that now the sign of the term in square brackets in front of the temperature gradient can be either positive of negative. In case of collisions with ions of lower mass and charge number, that term is positive and a negative temperature gradient produces an outward flux. Instead, in case of collisions with ions of greater mass and charge number, that term is negative and the resulting flux is inward.

Neo-classical impurity radial flux

The particle transport across a magnetic field in toroidal systems essentially differs from the classical transport discussed above. The main peculiarity of the transport phenomena in toroidal systems is the fact that the transport of particles across the magnetic field is defined in terms of longitudinal components of the friction force. The longitudinal transport of particles along the magnetic field lines must occur to compensate for the charge separation in the inhomogeneous toroidal magnetic field because of the gradient and centrifugal drifts of particles. Such fluxes of particles are ensured by the constituent of the electrical field $\mathbf{E}$ along $\mathbf{B}$ which produces the force balancing the longitudinal friction force between the particles. The difference of drift velocities $\mathbf{E} \times \mathbf{k}/B$ at the internal and external lines of the torus due to the decreasing field $\mathbf{B}$ at the external profile creates a flux of plasma particles across the magnetic field which after averaging over the magnetic surface turns out to be q^2 times more than the flux due to classical diffusion of particle across the field.

The precise formulation of the radial fluxes in the toroidal system depends on the regime of collisionality, and it will not be treated here. For the original derivation see the review paper by Hirshman and Sigmar [26]. In all cases the impurity flux can be written, like in the classical case, as the difference between the impurity density gradient and the main ion gradient, acting in opposite ways, plus the term arising from the temperature gradient, which can be either positive (outward) or negative (inward).

$$\Gamma_z = k \left(\frac{1}{n_\mathrm{i}} \frac{\partial n_\mathrm{i}}{\partial r} - \frac{1}{Z n_z} \frac{\partial n_z}{\partial r} - \alpha \frac{1}{T} \frac{\partial T}{\partial r} \right) \tag{1.22}$$

where $k(>0)$ and α depend on the collisional regimes of both plasma ions and impurities. The steady-state impurity profile is then given by

$$\frac{n_z(r)}{n_z(0)} = \left(\frac{n_\mathrm{i}(r)}{n_\mathrm{i}(0)}\right)^Z \left(\frac{T_\mathrm{i}(r)}{T_\mathrm{i}(0)}\right)^{-\alpha Z} \tag{1.23}$$

In the absent of a thermal force, this equation implies a concentration of impurities towards the magnetic axis. However this can be counteract if the parameter α is positive, leading to the already mentioned temperature screening effect.

Let us see, for example, what is the condition for the parameter α to be positive if impurities lie in the Pfirsch-Schlüter regime. This is a relevant case for tokamaks because it is generally found that impurities are in this regime while hydrogen ions are in the banana regime (however, light impurities may be marginally in the plateau regime). Generally, impurities are in a higher collisionality regime than the hydrogen ions.

In the case of a two-ion species plasma, one of which corresponds to the main ions of plasma ($Z_\mathrm{i} = 1$) and the other to the ions of the impurity which are in the singularly possible charge state of Z, the expression for the impurity ion flux in the Pfirsch-Schlüter regime, assuming $m_z \gg m_\mathrm{i}$ and $n_z Z^2 \gg n_\mathrm{i}$, is given by [25]

$$\Gamma_z^\mathrm{ps} = \frac{\nu_{\mathrm{i}z}\rho_\mathrm{i}^2 n_\mathrm{i}}{2Z} q^2 \left[\frac{1}{n_\mathrm{i}}\frac{\partial n_\mathrm{i}}{\partial r} - \frac{1}{Z n_z}\frac{\partial n_z}{\partial r} - \left(\frac{1}{Z} - \frac{1}{3} + \frac{2}{3}\frac{n_z}{n_\mathrm{i} Z}\right)\frac{1}{T}\frac{\partial T}{\partial r}\right] \tag{1.24}$$

As we have seen before, the temperature screening of impurities due to thermal diffusion is possible if the term in brackets in front of $\frac{\partial T}{\partial r}$ is positive. It is realisable when

$$\frac{n_z}{n_\mathrm{i}} > \frac{Z-3}{2} \tag{1.25}$$

from which it follows that the temperature screening of impurities becomes possible only for the impurities with small Z, in fact only at $Z \leq 3$ in the areas of abrupt decreases of temperatures. When the characteristic scales of changing densities and temperatures are similar, screening is possible only if $n_z > (2Z-3)n_\mathrm{i}$, i.e. only for the impurity with the charge $Z = 1$.

According to this discussion, avoidance of impurity accumulation in the plasma centre is not foreseen, since common impurities (C^{+6}, O^{+8}) do not fulfil requirement (1.25). But, if multiple-ion species plasma is considered, the theory must be modified. In this case, it has been theoretically determined that a condition exists that allows purification of the plasma by the ion temperature gradient when impurities are in the Pfirsch-Schlüter regime. The condition for this is that $v_\mathrm{Ti}^2 \tau_\mathrm{Di}\tau_\mathrm{Mi}(qR)^{-2}$ increase through a value ~ 1 (v_Ti^2, τ_Di and τ_Mi are the thermal velocity and the relaxation times for deflection and Maxwellization of main ions, respectively) [27].

Applying the neo-classical theory of impurity transport to present day experiments, it is found that the parameter α in Eq. (1.23) is predicted to be positive in all devices, and also for ITER [28]. Its value ranges approximately from 0.2 to 0.5 when "collisionality" ν_z^* is increased ($\nu_z^* = \nu_z qR/v_{\mathrm{T}z}$, where $v_{\mathrm{T}z}$ is the impurity ion thermal velocity and ν_z the collision frequency of a test impurity ion on all other particle species of the plasma). α is an asymptotically decreasing function of Z. The screening is stronger in situations where the classical flux contributes strongly to the neoclassical flux [29].

However, in most cases, the outward flux due to the ion temperature gradient is not sufficient to balance the inward flux due to the ion density gradient, and impurity accumulation in the

plasma centre is predicted, with a peaking factor ($n_z'/n_z = v/D$) increasing with Z. Neoclassical impurity accumulation is thus expected to be more serious for heavy species.

Comparison with experiments

Calculations employing neo-classical expressions for the impurity ion fluxes often show that they cannot explain the experimental results. Generally speaking, these simulations show impurity accumulation towards the centre, accompanied by a reduction of the density of less ionised peripheral ions. These predictions are rarely matched exactly by the observations across most of the plasma radius [29, 30], with the exception of some particular plasma regions. The impurity diffusion within a strong internal transport barrier is observed to be close to its neoclassical value [31] and it is observed in ASDEX Upgrade that tungsten strongly accumulates in the plasma core in accordance with neoclassical theory [32].

The anomalous part of the observed transport, which generally mitigates the neoclassical accumulation, is admitted to originate from turbulence. It has become customary, therefore, to add a supplementary term to the neo-classical flux, in order to have the total flux in the form

$$\Gamma = \Gamma^{\mathrm{neo}} + \Gamma^{\mathrm{turb}} \tag{1.26}$$

Either flux term is in turn assumed to be the sum of a diffusive flux and a convective flux

$$\Gamma_z = -D\nabla n_z + v n_z \tag{1.27}$$

The total transport coefficients D and v will thus be the sum of their neoclassical and turbulent components.

This anomalous transport is believed to arise from turbulence diffusion caused by fluctuations in the plasma. There may be fluctuations in the electric field, either electrostatic or electromagnetic, and fluctuations is the magnetic field with an associated change in the magnetic topology. In the next Section we shall calculate the anomalous transport originating from magnetic fluctuations.

1.6.2 Anomalous transport due to magnetic fluctuations

Stochastic magnetic fields have an effect on impurity ion transport. At sufficient turbulence levels, the ion transport in the stochastic field is comparable to neoclassical rates. Rapid transport of electrons as compared with ions may give rise to a positive ambipolar potential of the order of the electron thermal energy, resulting in an outward convection of the impurity ions which may offset the inward neoclassical convection.

The effect of low-frequency ($\omega \ll \omega_{\mathrm{ci}}$), long-wavelength ($k_\perp p_{\mathrm{i}} \ll 1$) magnetic fluctuations on the guiding centre distribution function f of any particular species of a plasma can be described as a diffusion at constant energy [33]. In the presence of a radial electric field E_r, this diffusion is described by an operator given in cylindrical coordinates by the expression [34]

$$\left|v_\parallel\right|\left(\frac{\partial}{\partial r} + \frac{\mathrm{e}E_r}{m}\frac{\partial}{\partial v_\parallel^2/2}\right) D_{\mathrm{m}} \left(\frac{\partial}{\partial r} + \frac{\mathrm{e}E_r}{m}\frac{\partial}{\partial v_\parallel^2/2}\right) f \tag{1.28}$$

D_m is the diffusion coefficient of the stochastic magnetic field for the collisionless regime, given by the Rechester and Rosenbluth's formula [35]

$$D_\mathrm{m} = L_\mathrm{c} \sum_{m,n} \left| \frac{b_r(m,n)}{B} \right|^2 \times \delta\left(\frac{m}{q} - n\right) \tag{1.29}$$

where L_c is the correlation length of the magnetic field lines; physically, L_c represents the length over which two exponentially diverging field lines become decorrelated from each other. In the "collisionless" limit the mean free path λ exceeds the correlation length L_c. A particle subject to collisions performs a random walk with a diffusion coefficient $D = v_\parallel D_\mathrm{m}$.

Taking f to be a Maxwellian and integrating over velocity, Eq. (1.28) leads to a cross-field particle flux [36]

$$\Gamma_x = -\frac{D_\mathrm{m}}{\pi^{1/2}} \left(\frac{\partial}{\partial r} n v_\mathrm{T} - \frac{2\mathrm{e}E_r}{m v_\mathrm{T}} n \right) \tag{1.30}$$

In steady-state, the radial electric field in Eq. (1.30) can be determined by invoking the ambipolarity condition $\Gamma_\mathrm{i} = \Gamma_\mathrm{e}$. In the large mass ratio limit $m_\mathrm{i} \gg m_\mathrm{e}$, assuming equal temperatures for all species, the ambipolar electric field is given by

$$E_r = -\frac{T}{\mathrm{e}} \frac{\partial}{\partial r} \ln(n T^{1/2}) \tag{1.31}$$

Equation (1.31) gives a radial electric field large enough to retard the electron motion so that there is not net cross-field electron flux. This radial electric field does not depend on the amplitude of the magnetic field perturbations.

Applying Eqs (1.30) and (1.31) to impurity ions of charge Z and mass m_z, we obtain the expression for the anomalous flux due to magnetic fluctuations

$$\Gamma_z^\mathrm{st} = D_\mathrm{m} \left(\frac{2T}{\pi m_z} \right)^{1/2} n_z \left[-\frac{Z}{n_\mathrm{i}} \frac{\partial n_\mathrm{i}}{\partial r} - \frac{1}{n_z} \frac{\partial n_z}{\partial r} - \frac{(1+Z)}{2T} \frac{\partial T}{\partial r} \right] \tag{1.32}$$

We find again the structure of the radial flux as the sum of three terms, but now an important difference is the sign of the density gradient term, which is negative. The resulting anomalous outward convection originates from the expulsion of ions by the positive ambipolar potential, whereas the corresponding term in the neoclassical expression leads to the inward impurity convection (see Eq. (1.24)).

1.6.3 Transport coefficients estimation

The transport coefficients in Eq. (1.27) can be estimated by reproducing through a transport code the plasma measurements related with the presence of impurities. Quantitative analysis of the impurity behaviour can be performed simulating the experimental signals by a one-dimensional (1D) impurity transport code, where poloidal symmetry of the impurity density is supposed. This is possible is circular cross section devices like RFPs or tokamaks with no divertor, if the considered plasma region is the inner part of the confined plasma, where poloidal and toroidal

asymmetries due to the three-dimensional distribution of the plasma-wall interaction can be neglected. In the case of divertor plasmas, which are poloidally asymmetric, the simulated results are applicable only to the equatorial plane (i.e., in a region where 2D effects can, to some extent, be neglected). Simulation of the impurity behaviour in diverted discharges should be done by coupling a core impurity transport code with a divertor impurity transport code, thus taking into account both core and divertor plasma experimental data [37].

The easiest way would be to measure the radial profiles of impurity ions and then adjust the transport coefficients in the code until a match is achieved within the experimental uncertainties. Unfortunately this measure is quite hard to be carried out and often other plasma measurements are reproduced by the code and used to estimate the transport coefficients. These may be profiles of visible Bremsstrahlung, line emissions, radiation power and soft X-ray intensity.

Transport calculations can be performed for intrinsic impurities or for deliberately injected impurities. Time modelling of intrinsic impurity transport is difficult, mainly because the peripheral impurity sources are very poorly known and very often irreproducible. Often, a simulated situation is that corresponding to the injection (gas puff or laser injected) of a small controlled amount of impurities. Among other advantages, this situation results in perfect knowledge of the injection time and good knowledge of the injection source (for the gas puff). Typically, in an experiment of this type one chooses an element not naturally present in the plasma, so that there is no background emission. One also typically chooses an impurity not recycling on the walls, thus allowing the recycling coefficient to be taken equal to zero.

In a steady-state situation an ambiguity problem arises in determining the transport coefficients. In fact, if we consider the continuity equation (1.14) in a steady-state situation in source-free region, the impurity profile will be given by

$$n_z(r) = n_z(0) \exp\left(\int_0^r \frac{v(r)}{D(r)} \mathrm{d}r \right) \tag{1.33}$$

We see that only the ratio v/D (called *peaking factor*) can be determined in this situation. In order to resolve the two coefficients separately, transient experiments are needed. In these experiments the impurity content changes in time, due for example to an impurity injection, and this variation is followed and reproduced by the code.

Chapter 2

The reversed-field pinch

This chapter describes the RFP configuration in the magnetic fusion devices and presents a theoretical description of the particle transport in this magnetic configuration.

2.1 The RFP configuration

The Reversed-Field Pinch (RFP) is an axisymmetric toroidal system in which the plasma is confined by a combination of a toroidal field B_ϕ, produced largely by poloidal currents in the plasma, and a poloidal field, B_θ, produced by the plasma current flowing around the torus.

The term *pinch* defines any linear or toroidal plasma where the plasma column shrinks due to the Lorentz force generated by the interaction of a current carried by the plasma and the induced magnetic field.

Differently from tokamaks where $B_\theta \ll B_\phi$, in RFPs the magnetic field amplitude is compatible between the two components ($B_\theta \approx B_\phi$).

RFP is characterised by its natural tendency to relax in a configuration in which the toroidal field component reverses near the plasma edge, as shown in Fig. 2.1. In terms of safety factor $q = aB_\phi/RB_\theta$, RFP has $q < 1$ all along the minor radius and it becomes negative near the edge, as plotted in Fig. 2.2.

2.1.1 The dynamo effect

According to the linear MHD theory, in a resistive plasma the currents would decay with a characteristic time τ, which would tend to flatten the toroidal field profile and thus to loss the magnetic reversal. In fact the RFP, as a static conductor subjected to resistive diffusion, is described by the following equation

$$\frac{\partial \mathbf{B}}{\partial t} = \frac{\eta}{\mu_0}\nabla^2\mathbf{B} \tag{2.1}$$

The toroidal component of the magnetic field is expected to decade exponentially with the time constant τ. Generally, the experimental evidence demonstrated that the RFP configuration lasts as long as the plasma current is sustained, thus also longer than the predicted resistive diffusion time (Fig. 2.3). This suggests that some mechanism is necessary to regenerate the magnetic field continuously lost through resistive diffusion.

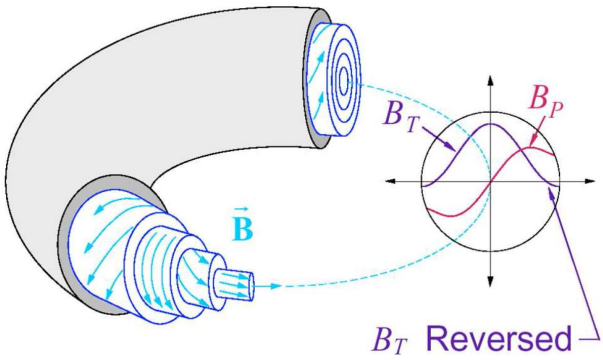

Figure 2.1: Sketch of the RFP magnetic field configuration with radial profiles of B_ϕ (violet) and B_θ (red).

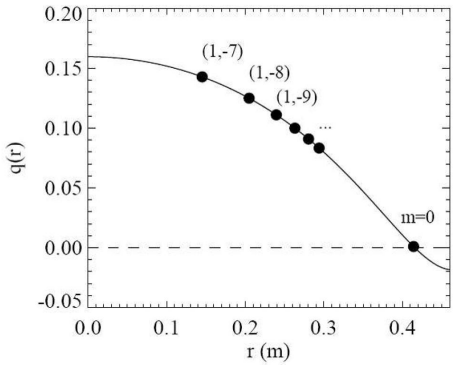

Figure 2.2: Typical RFP radial profile of the safety factor $q = aB_\phi/RB_\theta$. Many resonant surfaces for the MHD instabilities (marked with the poloidal and toroidal Fourier components m, n) are present in the internal plasma layers. The $q = 0$ region is a resonant surface for all the MHD instabilities with $m = 0$ toroidal periodicity.

In order to formally display the presence of this peculiar RFP mechanism, we can write the Ohm's law for the component parallel to the mean field

$$E_\parallel = \frac{(\mathbf{E} + \mathbf{v} \times \mathbf{B}) \cdot \mathbf{B}}{B} = \eta j_\parallel \tag{2.2}$$

$E_\parallel$ has the same form of B_ϕ, reversing its sign at the edge. On the contrary, from Eq. (2.2), $E_\parallel$ should follow the $j_\parallel$ profile, which experimentally is found to flow always in the same direction (see Fig. 2.4).

This discrepancy is usually related to the so called *dynamo effect* [38]. In fact, by separating each quantity (magnetic and velocity fields) in a mean-field plus a fluctuating term ($\mathbf{B} = \mathbf{B}_0 + \tilde{\mathbf{b}}, \mathbf{v} = \mathbf{v}_0 + \tilde{\mathbf{v}}$), a new electric field term arises in the parallel Ohm's law, which is called dynamo electric field E_d, and is given by the coherent interaction of the velocity and magnetic field fluctuations

$$E_\parallel + E_d = E_\parallel + \langle \tilde{\mathbf{v}} \times \tilde{\mathbf{b}} \rangle = \eta j_\parallel \tag{2.3}$$

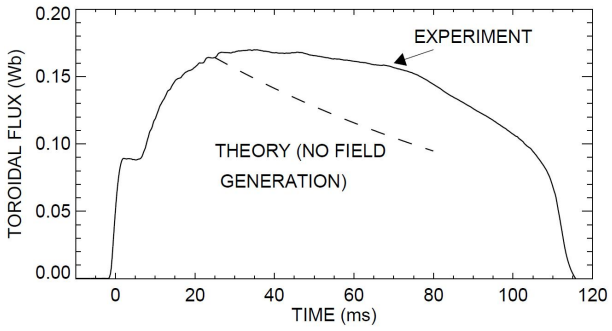

Figure 2.3: Experimental evolution of the toroidal flux and comparison with the prediction of a resistive diffusion cylindrical model without dynamo (dashed line).

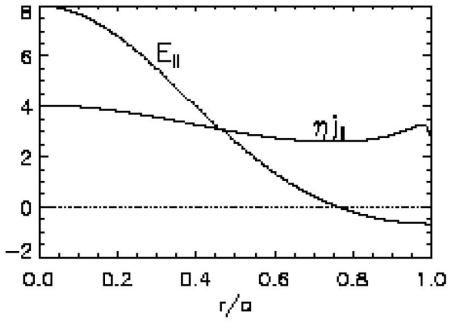

Figure 2.4: Typical radial profiles of $E_{\|}$ and $\eta j_{\|}$ in a RFP configuration. The discrepancy is accounted for the dynamo term E_d.

The sustainment of the RFP configuration is hence strongly related to the presence of a self-organised velocity field in the plasma (the dynamo). The origin of the dynamo is believed to be due to the magnetic activity peculiar of the RFP's q and in particular in the non-linear interaction of $m = 1$ modes, which are continuously excited according to the shape of the safety factor profile.

2.1.2 Multiple and quasi-single helicity

In its standard operation the RFP is characterised by a broad spectrum of resonant MHD instabilities, which were supposed necessary for the sustainment of the reversed-field configuration through the dynamo mechanism. In particular, these instabilities are driven unstable by a gradient in the current density parallel to the magnetic field and they are known as *tearing modes* [5]: the magnetic field lines tear and reconnect during the mode evolution. The magnetic configuration is characterised by the formation of *magnetic islands*.

The q profile shown in Fig. 2.2 highlights the presence of several resonant surfaces in the region internal to the reversal surface. In particular, all the tearing modes with periodicity $m = 1$ and $|n| \leq 2R/a$ can be simultaneously destabilised (multiple helicity). The superposition of the islands due to these resonant magnetic perturbations tends to destroy the magnetic surface in the innermost plasma with a detrimental effect on the global confinement, and usually leads to a

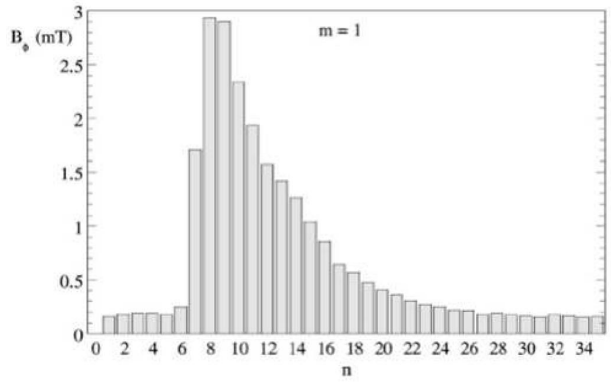

Figure 2.5: Typical RFP spectrum of the MHD tearing instabilities.

complete stochastisation of the field lines [39].

Moreover, at the edge where well conserved magnetic surfaces could exist unperturbed, the presence of the reversal surface ($q = 0$) destabilises all the modes with $m = 0, |n| > 1$ periodicity, being itself a resonant surface for these instabilities.

Finally, a complex non-linear interacting mechanism between $m = 1$ and $m = 0$ modes leads to the growth of a localised plasma deformation. This is due to a coupled $m = 0, n = 1$ instability, also known as *locked mode*, which causes a strong stationary plasma wall interaction [40].

A reversed configuration sustainment is also possible with the presence of a single dominant tearing mode, the so called single-helicity state (SH), where only one of the core-resonant resistive modes would provide the dynamo effect. Up to now, this has been predicted only theoretically [41]. Experimentally, the best approximation of the SH state is the quasi-single helicity state (QSH) observed in several RFPs [42], in which the innermost resonant $m = 1$ mode dominates over the others, the so called secondary modes, which maintain a finite amplitude. They are an intermediate state between the multiple-helicity and the theoretical single-helicity ones, because the secondary modes are still present [43]. This state will be described in more detail in Chapter 4.

2.2 Particle transport in the RFP

In RFPs the comparable strength of the poloidal and toroidal magnetic fields reduces the field-line connection length in comparison with tokamaks (the length along a magnetic field line connecting the toroidally inboard and outboard regions of a magnetic flux surface). The decrease of the connection length results in the reduction of the radial width of the banana orbit (the width of the banana-shaped path traced out by magnetic-mirror-trapped particles in a toroidal plasma). The width of the banana orbit is in turn proportional to the deviation of a particle from a magnetic surface. Inevitably transverse diffusion coefficients should be smaller than those computed for a typical low-β, large aspect-ratio, toroidal plasma, such as a plasma in tokamak, where the assumption than the toroidal magnetic field is much larger than the poloidal one is often made (see Galeev and Sagdeev's computation [44]).

Wakatani and Itatani [45] investigated the collisional diffusion in a large aspect-ratio toroidal

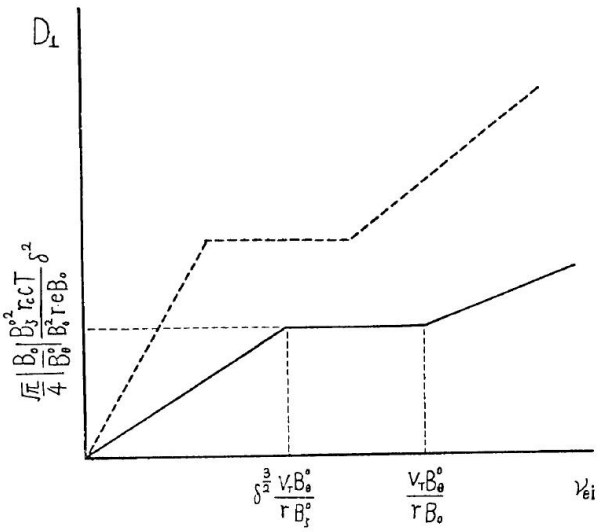

Figure 2.6: Transverse diffusion coefficient as a function of the electron-ion collision frequency. Solid line shows the transverse diffusion coefficient in a toroidal pinch with $B_\theta \sim B_\phi$ and dotted line shows that given by Galeev and Sagdeev for a low-β toroidal plasma with $B_\theta/B_\phi \ll 1$. [45]

pinch with $B_\theta \sim B_\phi$ for three regions of collisional frequencies, following the scheme of Galeev and Sagdeev for tokamaks. They considered the particle trapped in local magnetic mirrors related to the inhomogeneity of both toroidal and poloidal magnetic fields. Transverse diffusion coefficients including these effects result smaller than those given by Galeev and Sagdeev. In the banana region $D_\perp \simeq D_{\rm GS}\sqrt{\delta/\varepsilon}$ is obtained and in the plateau region $D_\perp \simeq D_{\rm GS}(\delta^2/\varepsilon^2)$, where $\varepsilon = a/R$ and the small parameter δ denotes the inhomogeneity of the toroidal and poloidal magnetic fields, being defined as

$$\delta = \frac{\Lambda B_\theta^2 + \varepsilon B_\phi^2}{B_\theta^2 + B_\phi^2} \tag{2.4}$$

where Λ is an asymmetric parameter which depends on the distribution of the plasma pressure and the poloidal magnetic field [46]. Note that the safety factor included in $D_\perp$ may be smaller than or comparable to unity.

Oshiyama and Masamune [47] computed the transverse diffusion coefficient for a RFP plasma ($B_\theta \sim B_\phi$, small q) in the MHD region (high collisionality, negligible trapped particles) by solving the equation of Ohm's law and the equilibrium equation. They found a transverse diffusion coefficient almost the same as the classical diffusion coefficient, also on the magnetic surface where $B_\phi = 0$.

The diffusion coefficients are plotted in Fig. 2.6 as a function of the collision frequency. Also plotted are the diffusion coefficients given by Galeev and Sagdeev (see Fig. 1.4). The poloidal magnetic field comparable to the toroidal one diminishes the diffusion coefficient and the slope of the line in the banana and MHD regions. In addition, the collision frequency at which trapped particles are effective in transport phenomena increases.

Monte Carlo simulations for neo-classical transport in a RFP compare well with theoretical predictions, indicating that the neo-classical transport due to guiding centre drift is one or two

orders lower than classical transport [48].

In conclusion it is possible to say that in the RFP particle transport due to collisions only can be considered classical for all collisionality regimes.

However, in presence of MHD fluctuations Monte Carlo simulations show that particle diffusion is much higher than classical or neoclassical expectations due to anomalous transport [48]. Under MHD fluctuations with high stochasticity Monte Carlo calculations agree with theoretical predictions given by Rechester and Rosenbluth [35] (see Eq. (1.29)). In a standard RFP plasma, anomalous electron diffusion and thermal conductivity due to inherently existing MHD fluctuations are the primary loss mechanisms compared to classical and neoclassical transport.

Indeed, large amplitude magnetic fluctuations and associated field-line stochasticity in RFPs have historically caused transport much larger than the classical expectation, thus masking classical transport in experiments. In recent years, in the two main RFPs in operation, the achievement of new regimes characterised by lower level of stochasticity has led to a better confinement and lower values of the diffusion coefficient of the main gas.

At RFX-mod in the multiple helicity regime (MH) the diffusion coefficient of the main gas was found in agreement with theoretical predictions for stochastic transport [35], thus confirming the stochastic nature of the transport especially in the core plasma [49]. In recent years, the spontaneous generation of quasi-single helicity (QSH) regimes (configurations with a dominant mode in the spectrum of magnetic field fluctuations) has produced regions with a reduced level of chaos. QSH states are characterised by an improvement in global plasma performance in terms of electron temperature and energy confinement time [43]. Perturbative experiments through H pellet injections evidenced that particle diffusion coefficient is significantly reduced in the core in the improved confinement regime [50].

At MST RFP, suppression of magnetic fluctuations through the PPCD technique has significantly improved the device's performance [51, 52, 53]. Low level of stochasticity has led to good confinement and reduced transport. The electron diffusion coefficient is found 2 orders of magnitude lower than the one of a standard plasma with no suppression of magnetic fluctuations, and roughly independent on velocity, inconsistently with theoretical expectation for transport from magnetic stochasticity (see Section 1.6.2) [54]. This suggests that such RFP plasmas have transitioned to a new regime no longer dominated by magnetic stochasticity.

Regarding the impurity transport, in RFX-mod experiments with Ni laser blow-off and Ne gas puffing in both MH and QSH regimes determined transport coefficients (diffusion coefficient and convective velocity) not in agreement with stochastic or classical expectations [55]. The diffusion coefficient was found almost equal for the two magnetic regimes, characterised by a high value in the core and low at the edge. The convective velocity was found outwardly directed over the whole plasma with a barrier (region of stronger outward velocity) in the external region. This barrier prevents impurities from penetrating to the core plasma. The barrier is less external and stronger in the QSH regime.

Outward convection of impurity ions was also reported in MST during the improved confinement regime (PPCD). Measurements of fully stripped carbon densities showed that at the onset between standard and improved confinement regime the C density profile becomes hollow, with a slow decay in the core region concurrent with an increase in the outer region, implying an outward convection of impurities [56].

Therefore, the transition to new regimes of enhanced confinement also strongly influences the transport of impurities. In Chapters 4 and 5 these experimental discoveries will be described

in more detail and, as part of the original work of this thesis, recent experiments, modelling and simulations will be presented, in order to better understand the behaviour of impurities in the RFP.

Chapter 3

Impurity collisional-radiative and transport code

The model employed in this thesis is a 1-D time dependent impurity transport code coupled to a collisional-radiative (CR) code for various species (Li, B, C and O). The transport code calculates the radial population of the ground states of the ions, by means of two radius dependent transport parameters: a diffusion coefficient D and a convective velocity v. For each radial positions the CR model is applied to describe the steady-state excited level populations of the helium-like and hydrogen-like ions. The CR model computes the photon emissivity of considered lines at electron density and temperature values corresponding to the experimental situations. Plasma emissions are then evaluated and simulated spectra are obtained along with impurity ion abundances.

3.1 Transport model

The impurity transport code describes in cylindrical geometry ionisation, recombination, charge-exchange and radial transport of the ions of a given atomic species. The system to be solved is the set of continuity equations (1.14).

The impurity flux density Γ_z is expressed as the sum of a diffusive and an outward convective term, as in Eq. (1.27):

$$\Gamma_z = -D \frac{\partial n_z}{\partial r} + v\, n_z \tag{3.1}$$

where D and v are the radially dependent diffusion coefficient and outward convection (or pinch) velocity, respectively, both considered to be independent of the charge of the ions.

The continuity equations (1.14) are initially solved for the ground states of the ions; then, for each radial position, the collisional-radiative model is applied to calculate the steady-state excited level populations of the He-like and H-like ions and finally the absolute intensities of the spectral lines.

3.2 Collisional-radiative model

The CR model redistributes the ion population deduced by the transport equation among the energy levels of H-like and He-like ions for carbon, oxygen, boron and lithium.

Collisional radiative models (CRM) were built for carbon and oxygen in order to reconstruct the intrinsic impurity emissions from RFX [57]. Afterwards, CRM for boron was also built in order to simulate boron emission following a boronisation [58]. Recently, a preliminary version of Li CRM has been built in order to reconstruct lithium emission after lithisation [9].

CRM considers only H-like and He-like ion isoelectronic sequences. For both sequences, excited levels up to the principal quantum level $n = 5$ are included, this limitation being determined by the following two reasons. At first, for these two elements detailed l-resolved atomic physics calculations are available in the published literature only up to $n = 5$. Second, the emitting levels of all the lines to be considered for the simulation of experimental brightnesses and/or emissivities from fusion devices are included in the model as well as the levels predominantly populated by charge-exchange recombination.

In Fig. 3.1 are shown the considered energy levels for carbon and oxygen H-like and He-like ions. The populations of these excited levels are determined by the balance of the following processes: electron collisions from the ground state, two-body radiative and dielectronic recombinations, radiative decays and cascades and, finally, $\Delta n = 0$ redistributive collisions. Electron excitation from $n = 2$ to $n = 3$ levels and ionisation from the same $n = 2$ level are also included. Photon emissivity coefficients are evaluated for the most important lines, e.g., the Lyman and Balmer series lines for H-like ions and the resonance and intercombination lines for He-like ions.

Reliable atomic data are a prerequisite to the impurity simulations, since they are supposed to be well known and adjustments of the simulations to the experimental line and/or continuum brightnesses and emissivities are done by varying only D and v. Atomic data include cross sections and rate coefficients for various processes such as ionisation, excitation, recombination, charge exchange, and also transition probabilities for line emission. The world largest atomic database for modelling the radiating properties of ions and atoms in plasmas is the Atomic Data and Analysis Structure (ADAS) [59], created by the University of Strathclyde and the JET Joint Undertaking. Recent data coming from this and other sources are incorporated in the CR model and are periodically reviewed. A complete list of the literature employed in the CRM can be found in [57].

3.2.1 CR model for H-like ions

The CRM is obtained by solving the system of balance equations for a plasma composed of a nearly equal number density n_e of electrons and protons (or deuterons), with equal (or different) electron and ion temperatures T_e, and T_i. Neutral hydrogen (or deuterium) atoms of number density n_n are also present with the same temperature as the ions. The plasma contains fractions of fully stripped and H-like impurity ions with known number densities n_str and n_hy, respectively. n_i is the population density of the level i of the H-like ions (according to the previous discussion, 21 levels are included, since levels up to $n = 4$ included are j-resolved, and $n = 5$ levels are only l-resolved). A_{ij} is the radiative transition probability from the level i to the lower level j, Q_{ij} is the collision excitation or deexcitation rate coefficient from the level i to the level j (excitations and deexcitations being related through the detailed balance relation). Moreover, R_i^rad and R_i^cx

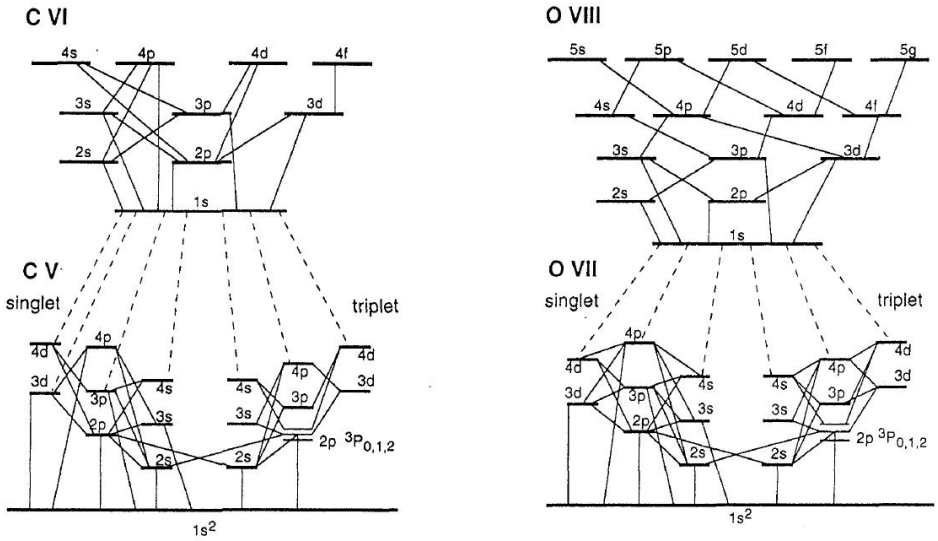

Figure 3.1: Energy levels considered in the CR model for carbon and oxygen helium-like and hydrogen-like ions. Dashed lanes correspond to charge-exchange processes, solid lines to collisional excitations, deexcitations and radiative decays. [60]

are, respectively, the rate coefficients for radiative recombination and charge-exchange recombination of fully stripped ions into the level i, and S_i^{ion} is the stepwise ionisation rate coefficient from the level i. For each excited level i a statistical balance equation is written as the difference between an output term given by

$$\sum_{j\neq i} Q_{ij} n_{\mathrm{e}} n_i + \sum_{j\neq i} A_{ij} n_i + S_i^{\mathrm{ion}} n_{\mathrm{e}} n_i \tag{3.2}$$

and an input term given by

$$\sum_{j\neq i} Q_{ji} n_{\mathrm{e}} n_j + \sum_{j\neq i} A_{ji} n_j + R_i^{\mathrm{rad}} n_{\mathrm{e}} n_{\mathrm{str}} + R_i^{\mathrm{cx}} n_{\mathrm{str}} n_{\mathrm{n}} \tag{3.3}$$

Moreover, another constraint is given by $\sum_i n_i = n_{\mathrm{hy}}$. In all sums the ground level has to be included. Having solved this system, it is possible to calculate the photon emissivity of any selected line as the product of the upper level number density times the transition probability.

3.2.2 CR model for He-like ions

For He-like ions, the CRM does not differ from the one described in the previous section for H-like ions. The plasma now contains fractions of H-like, He-like and Li-like impurity ions with known number densities n_{hy}, n_{he} and n_{li}. n_i is the population density of the level i of the He-like ions (according to the previous discussion, 31 levels are included, since only the three ls2p $^3\mathrm{P}_{0,1,2}$ levels are j-resolved). Eq. (3.2) remains the same while Eq. (3.3) now becomes

$$\sum_{j\neq i} Q_{ji} n_{\mathrm{e}} n_j + \sum_{j\neq i} A_{ji} n_j + R_i^{\mathrm{rad}} n_{\mathrm{e}} n_{\mathrm{hy}} + R_i^{\mathrm{cx}} n_{\mathrm{hy}} n_{\mathrm{n}} + R_i^{\mathrm{die}} n_{\mathrm{hy}} n_{\mathrm{e}} \tag{3.4}$$

Dielectronic recombination determines the supplementary term in Eq. (3.4), where R_i^{die} is the rate coefficient for dielectronic recombination into the level i. For the two ls2s levels a supplementary term is necessary in Eq. (3.4), which is equal to $S_i^{\mathrm{ision}} n_{\mathrm{li}} n_{\mathrm{e}}$, where S_i^{ision} is the rate coefficient for innershell ionisation into the level i. The final constraint becomes now $\sum_i n_i = n_{\mathrm{he}}$. As for H-like ions, solving the system allows to calculate the photon emissivity of any selected line as the product of the upper level number density times the transition probability.

3.3 Code inputs

Several plasma parameters are needed to evaluate the impurity populations and reproduce the plasma emissions. They enter the code as inputs and they can be either direct measurements or assumptions made following the measurements. The main plasma parameters are the electron temperature and density, whose profiles are needed to evaluate the required atomic physics rates. Their central value time evolutions come directly from plasma measurements: usually, $T_{\mathrm{e}}(r = 0, t)$ is measured through the double filter technique and $n_{\mathrm{e}}(r = 0, t)$ is the central line-averaged interferometry measurement. Their profiles are usually kept fixed in time. The electron temperature profile is generally assumed to be in the form

$$T_{\mathrm{e}}(r) = \left[T_{\mathrm{e}}(0) - T_{\mathrm{e}}(a)\right]\left[1 - \left(\frac{r}{a}\right)^{\alpha}\right]^{\beta} + T_{\mathrm{e}}(a) \tag{3.5}$$

This profile follows the indications from the electron temperature diagnostic (usually the Thomson scattering) and the value at the edge, $T_{\mathrm{e}}(a)$, is deduced from edge diagnostic measurements.

The electron density profile is assumed to be in the form

$$n_{\mathrm{e}}(r) = \left\{1 - \left[1 - \frac{n_1}{n_0} - \frac{n_a}{n_0}\right]\left(\frac{r}{a}\right)^{\alpha} - \frac{n_1}{n_0}\left(\frac{r}{a}\right)^{\beta}\right\} n_{\mathrm{e}}(0) \tag{3.6}$$

where n_0, n_1 and n_a are parameters describing the value of the density, respectively, in the core, in the mid-radius and at the edge; they are computed performing an inversion of the interferometry measurements.

For specific purposes, time variation of electron temperature and density profiles is possible, in order to have a detailed time dependent reconstruction of the plasma features along the radius. The time interval between different profiles is given by the acquisition rate of the related diagnostic.

Neutral density profile is a further input to the collisional-radiative code in order to evaluate the charge-exchange processes among highly ionised impurities and the main gas. It is assumed in the form

$$n_{\mathrm{n}}(r) = \left[nn_0 + (nn_a - nn_0)\left(\frac{r}{a}\right)^{B}\right] n_{\mathrm{e}}(0) \tag{3.7}$$

where

$$B = \left(\ln \frac{nn_m - nn_0}{nn_a - nn_0}\right) / \ln x_m \tag{3.8}$$

nn_0, nn_1 and nn_m are parameters describing the value of the neutral density, respectively, in the core, at $r/a = x_m$ and at the edge. Neutral profiles are calculated using the Monte Carlo neutral particle tracing code NENÈ [49] and are properly scaled to the measured emissions of neutral particles from the edge of the plasma.

They are normally found by matching the emission of neutral particles from the edge of the plasma with the simulations of a code based on a variety of neutral source profiles.

Impurity neutral influxes from the wall are also required by the code as boundary conditions. They are tuned to reproduce the measured line emissivities. The code also requires the diffusion velocity of neutral impurities from the wall, which is calculated from the neutral temperature at the edge and assuming thermal velocity.

Main gas ion temperature is a further input: it is simply inserted in the code multiplying the electron temperature by a constant factor taking into account the ratio between $T_e(0)$ and $T_i(0)$ but assuming the same profile.

The profiles of the transport coefficients, which enter the formula for the impurity flux (3.1), are also inputs to the code. They are usually chosen among a restrictive class of simple functions, linear between two consecutive spatial nodes. The reason of this simplification lies in the fact that this method of determination does not allow to have a more accurate deduction of the profiles of D and v.

3.4 Code outputs

The code reconstructs both the impurity population abundances and the plasma emissions. The transport code reconstructs the evolution of the radial profiles of the impurity density along the discharge. Those profiles can then be compared with measurements of the impurity density, for example carried out with charge-exchange recombination spectroscopy [61]. The code simulates also the plasma effective charge (Z_{eff}), which can be compared, for example, with Z_{eff} deduced from bremsstrahlung emission [62].

From the obtained ion populations the code computes the plasma emission composition. The code calculates the total radiated power following [63]. It computes the continuum emission in the visible range, evaluating the dependence of the Gaunt factor on the electron temperature and on the effective charge [64]. The free-free bremsstrahlung emission and the free-bound recombination emission in the SXR spectral range are also determined [65]. Emissivity of spectral lines is computed by the code for the lines of the considered impurities which are experimental available. Finally, SXR and line brightness profiles are computed in a post-process subroutine.

These reconstructed plasma emissions are then compared with the corresponding plasma measurements, depending on what diagnostic is installed and operative on the device, and on what plasma signal we are interested in observing and comparing with the simulation. Line emissions are compared with measured signals from spectrometers [66]. SXR emissions and profiles are compared with the data from a multichord tomographic system [62]. Total radiated power is compared with the measurements of a bolometer [55].

Through the comparison between simulated and experimental signals the transport coefficients (D and v) can be deduced. Those coefficients are varied until the best fit between the reconstructed and the measured signal is achieved within the experimental uncertainties. In case of transient experiments a discrimination between the two coefficients is possible, otherwise,

from a steady-state transport analysis, only their ratio can be determined.

3.5 Pellet ablation model

In order to simulate a solid pellet injection experiment, the transport code includes a pellet section. In this section the ablation of the pellet during its trajectory inside the plasma is reconstructed, together with the release of pellet's atoms into the plasma.

The ablation model used in the code is based upon Parks' calculations [67], and upon a preliminary application to RFX by Garzotti [68]. In this model it is assumed that the pellet is spherical and that the mass flow of the ablated material near the pellet undergoes a purely radial expansion. The ablatant then partially shields the pellet surface from the hot background plasma electrons, which stream through the cloud along magnetic field lines, heating the cloud through friction. The ablation process is self-regulatory because the shielding increases as the ablation rate increases. If the ablation cloud were too dense, the attenuation of the incident heat flux would be large, diminishing the production rate of ablated material; if it were too thin, the attenuation would be weak and the production rate would increase. Thus, the ablation cloud can attain a quasi-steady state at each instant by convecting away the hot electron heat input.

Electrons from the background plasma stream towards the pellet along the magnetic field lines. If the pellet were not shielded by its ablation cloud, the heat flux directed from the plasma to the pellet, averaged over its spherical surface, would be given by $f_{\mathrm{B}} \cdot q_\infty$, where q_∞, is the flux of energy crossing a plane perpendicular to the magnetic field lines asymptotically far from the pellet. The coefficient f_{B} accounts for the fact that the heat flux on the pellet surface is anisotropic in a magnetic field. Usually, f_{B} is slightly larger than one-half, its limiting value when the ratio of the electron gyroradius to the pellet radius tends to zero. For Maxwellian electrons, q_∞ becomes

$$q_\infty = \frac{1}{4} n_{\mathrm{e}} v_{\mathrm{e}} (2T_{\mathrm{e}}) \tag{3.9}$$

where n_{e} is the electron density, T_{e} is the background plasma electron temperature, $v_{\mathrm{e}} = (8T_{\mathrm{e}}/\pi m_{\mathrm{e}})^{1/2}$, and the product $\frac{1}{4} n_{\mathrm{e}} v_{\mathrm{e}}$ is the particle flux.

According to the model, the velocity of the receding pellet surface is given by

$$\dot{r}_0 = \frac{f_{\mathrm{B}}\, \eta\, q_\infty(T_{\mathrm{e}}, n_{\mathrm{e}})}{n_0(\Delta H + 2.7 T_1)} \tag{3.10}$$

where η is the heat flux attenuation coefficient, n_0 and ΔH are, respectively, the solid density and the sublimation heat of the pellet material and T_1 is a temperature of the order of 0.2-0.5 eV. The parameters f_B, η, and T_1 are self-consistently calculated in the model.

In the transport code the model gets as inputs: the pellet radius, its radial trajectory usually recorded by cameras and/or detectors inside the chamber, along with the local electron temperature and density. Then, the model computes the pellet ablation and consequent release of particles, which corresponds to an additional source term, time and space dependent, in the continuity equation (1.14). In this way, during the simulation of pellet injections, the code is able to reproduce the enhancement in electron density and radiative emission of the plasma, which are of crucial importance in order to evaluate the transport coefficients.

Chapter 4

Impurity transport analysis on RFX-mod

This chapter presents the experiments carried out on RFX-mod through impurity injections with the aim of studying the transport of different species. Solid pellets of carbon and lithium have been injected and the transients originating in the plasma features have been reproduced with the transport code, allowing a determination of the transport coefficients. Tungsten has been injected through the laser blow-off technique and its behaviour has been monitored through the acquisition of different plasma signals.

4.1 RFX-mod experiment

RFX-mod (Reversed-Field eXperiment) is a large RFP located in Padua, Italy. Its main parameters are listed in the following table.

Major radius	2 m
Minor radius	0.46 m
Toroidal magnetic field	≤ 0.7 T
Plasma current	≤ 2 MA
Electron density	$\approx 1 \div 10 \times 10^{19}$ m^{-3}
Discharge duration	≤ 0.5 s

RFX-mod is the renewed and upgraded version [69] of the former RFX device [70], and started its operation in 2004. The original RFX thick stabilising shell was replaced with a thinner one, in order to reduce the magnetic field penetration time constant. Moreover, RFX-mod is equipped with an advanced system for feedback control of MHD stability, based on 192 active saddle coils, which cover the whole plasma boundary [71].

RFX-mod is characterised by two different magnetic regimes: the plasma self-moves from one to the other after an increase in the plasma current. At low current ($I_p < 1$ MA) many kink-tearing MHD modes ($m = 1, |n| \geq 2R/a$) are simultaneously present and nonlinearly interacting. This is the Multiple Helicity (MH) regime where magnetic chaos dominates the plasma and drives anomalous transport [72]. At higher current ($I_p > 1$ MA) the magnetic topology spontaneously self-organises into an ohmic helical symmetry, the Quasi-Single Helicity (QSH) regime,

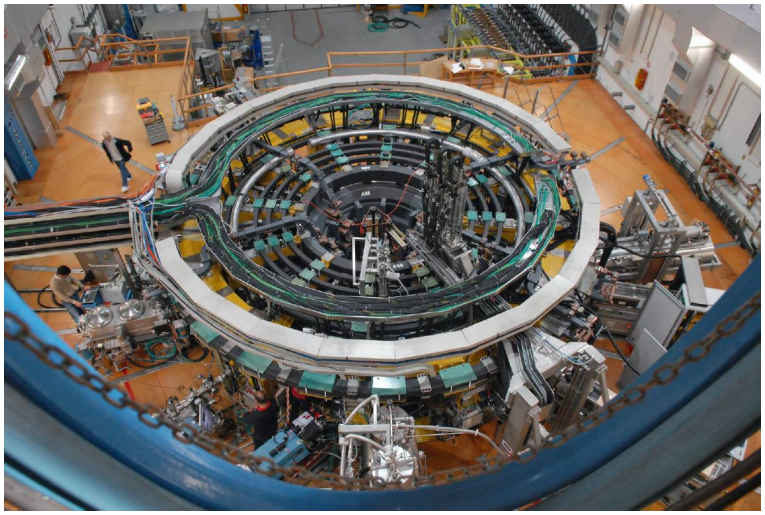

Figure 4.1: The RFX-mod experiment.

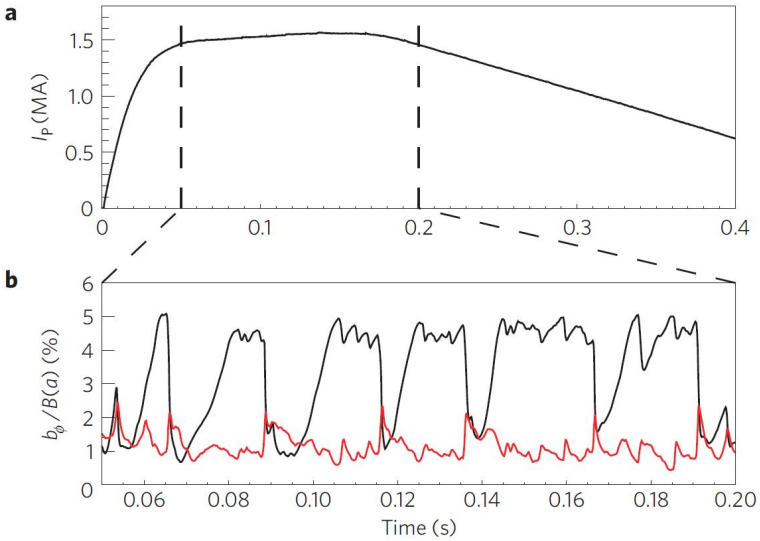

Figure 4.2: (a) Plasma current as a function of time. The vertical dashed lines delimit the so-called flat-top phase of the discharge. (b) The black curve shows the amplitude of the $m = 1$ / $n = -7$ dominant mode during the flat-top phase of the discharge, and the red curve shows the amplitude of the secondary modes ($m = 1$ / $n = -8$ to -23), defined as the square root of the sum of their squared amplitudes. It is clearly seen that the system oscillates between two states, one where all of the modes have similar amplitudes (MH) and another one where there are a dominant mode and secondary ones (QSH). [43]

in which the magnetic dynamics are dominated by the innermost resonant mode ($m = 1, n = -7$), with the new magnetic axis helically twisting around the geometrical axis of the torus [42]. Theoretically, the dynamo mechanism required to sustain the RFP equilibrium fields can be provided by the nonlinear saturation of a single kink-tearing mode: the Single Helicity (SH) regime [41]. The QSH regime approximates this state since the secondary mode amplitudes are low but not

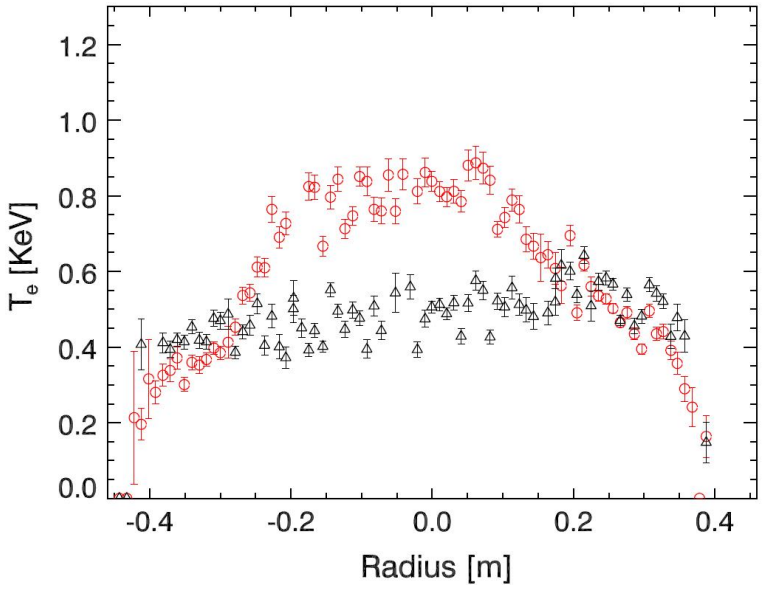

Figure 4.3: Electron temperature profiles obtained by Thomson scattering diagnostics for the same high current discharge during QSH (red symbols) and in MH phases (black symbols). [74]

negligible (see Fig. 4.2).

The high current discharges in RFX-mod are characterized by intermittent QSH phases that occupy a significant fraction (up to 85%) of the discharge flat-top [73]. Inside the helical structure energy confinement is enhanced and electron temperatures exceeding 1 keV are measured, with steep gradients, which identify an internal transport barrier (see Fig. 4.3). The steep temperature profiles obtained in QSH conditions correspond to an electron thermal diffusivity reduced by up to more than one order of magnitude [74]. Pellet injection experiments evidenced an improvement by a factor 2-3 of the main gas confinement time from MH to QSH state [50].

An upper critical density $n_C = 0.3 \div 0.4\, n_G$ (n_G Greenwald density) is found to limit the operational space for the QSH regime: magnetic topology reconstructions and diagnostic observations suggest that this limit is due to a helical plasma-wall interaction which determines toroidally and poloidally localised edge density accumulation and cooling [75].

RFX-mod has no limiter and the plasma interacts directly with the first wall. This is composed by graphite tiles that cover completely the inner part of the vacuum vessel (see Fig. 4.4). The shape of the tiles was designed to improve plasma-wall interaction by reducing the heat flux peaking on leading edge. Graphite was chosen for its low atomic number and for its capability to withstand high power loads. The main disadvantage of this choice is the great hydrogen retention of graphite, which makes density control very difficult with resulting negative effects on operation and performance, preventing the development of the QSH states for $n_e > n_C$.

To overcome the described limitation different techniques of wall conditioning have been applied on RFX-mod. Baking the vacuum vessel, at the limit temperature of 170 °C to avoid damage to the in vessel probes, for outgassing of contaminating atoms from tiles (H_2O, H_2, O_2, N_2, He,...). RF-assisted glow discharges (GDC) with flowing gas, performed through two anodes at 180 toroidal degrees with a voltage up to 1000 V [58]. GDCs are carried out in He to remove H_2 by physical sputtering and in H_2 to remove O_2 and C by chemical sputtering. Boronisation

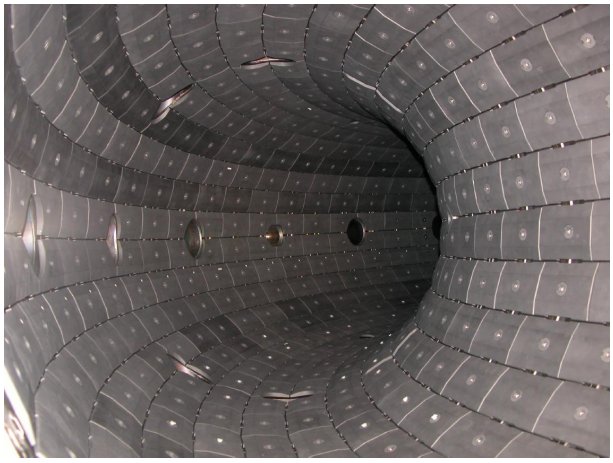

Figure 4.4: RFX-mod's inner wall.

by the GDC plant using a mixture of B_2H_6 (diborane) 10% and He 90%, with a getter effect for O_2 and a reduction of H_2 fuelling from the wall [76]. Lithisation with different techniques: by depositing a controllable amount of lithium on the wall through a room temperature pellet injector [9], or by evaporation through a liquid lithium limiter [77]. Lithisation has proven to best method for wall conditioning, lowering hydrogen wall recycling to a value smaller than that of boronised graphite, with the effect lasting 20-30% more than in the boronised case. Recently, an action for a more uniform coating, with a significant amount of injected Li, has been performed testing a multi-pellet injector developed at PPPL [77].

Within the machine upgrade planned for the next years, a tungsten first wall is currently under consideration for replacing the graphite wall and solving the problem of the difficult density control due to the high H retention of carbon.

Main intrinsic impurities in RFX-mod are carbon, coming from the graphite tiles as result of plasma-wall interactions, and oxygen from the adsorption of H_2O vapour when the machine is brought up to air and consecutive release into the plasma during the discharges. After boronisation or lithisation, amount of B or Li are present in the device. Also very small traces of N coming from the atmospheric air can remain in the vacuum vessel despite the pumping system.

4.2 The state of knowledge of the impurity transport in RFX-mod: nickel and neon

In the years 2009-10 a series of transient experiments were carried out in order to study the impurity transport in the different regimes of the RFX-mod plasma [55]. Those experiments were based on the injection of non-intrinsic impurities (Ni and Ne) into the plasma and on the successive reproduction of the plasma emissions following the injection through collisional-radiative and transport codes for Ni and Ne, described in Chapter 3. The injections were performed through nickel laser blow-off and neon gas puffing in the MH and QSH magnetic confinement regimes. The experimental signals, acquired and simulated, were line emission, continuum soft x-ray radiation and total radiated power. The collisional-radiative model assumed as inputs the transport coefficients D and v, an electron temperature and density radial profile and time evolu-

tion based on experimental measurements. The transport coefficients were varied until a match was achieved between the simulation and the measurements.

The D and v obtained for Ni and Ne in the two magnetic regimes are shown in Figs 4.5 and 4.6. The pinch velocity is directed outwards and has a large barrier in the external plasma and no reversal. The diffusion coefficient is an order of magnitude lower in the edge than in the core. The transition region in D and v is more external for the MH plasmas and the barrier in velocity is weaker. Despite the differences in mass, the transport coefficients derived for both the Ni and Ne impurities were of a similar form and magnitude. The outward pinch velocity and barrier acts to prevent the impurities progressing into the core and prevent impurity accumulation especially in the improved confinement QSH regime.

In the same work [55] the classical and stochastic D and v had also been evaluated to compare the determined transport coefficients with theoretical predictions. Classical coefficients were calculated applying Eq. (1.21). Stochastic transport was evaluated computing the diffusion coefficient of the stochastic magnetic field from the measured magnetic amplitude fluctuations, following Eq. (1.29). They are included in Figs 4.5 and 4.6. D is at least one order of magnitude greater than both classical and stochastic predictions, and also v is not compatible with the theoretical models. In both QSH and MH regimes, the experimental determination of D and v is not consistent with the classical evaluation or the transport through a stochastic magnetic field: a theoretical frame is still missing.

Laser blow-off and gas puffing are techniques which introduce impurities into the edge of the plasma: information on the impurities inside the barrier, at the core of the plasma, is more restricted. Furthermore, the profiles of T_e and n_e vary little in the central region. Due to these reasons the transport coefficients are scarcely sensitive in the core region; we have few information in order to determine the value of D and n in the core. A better understanding of the transport coefficient in the core plasma can be gained by directly injecting into the core: in this way we would have a centrally located impurity source which will modify the profiles of temperature and density, giving enough information to fully determine the behaviour of impurities in the core. With this regard, experiments have been carried out during my Ph.D. activity using solid pellets of light elements to achieve this necessary centrally located impurity source.

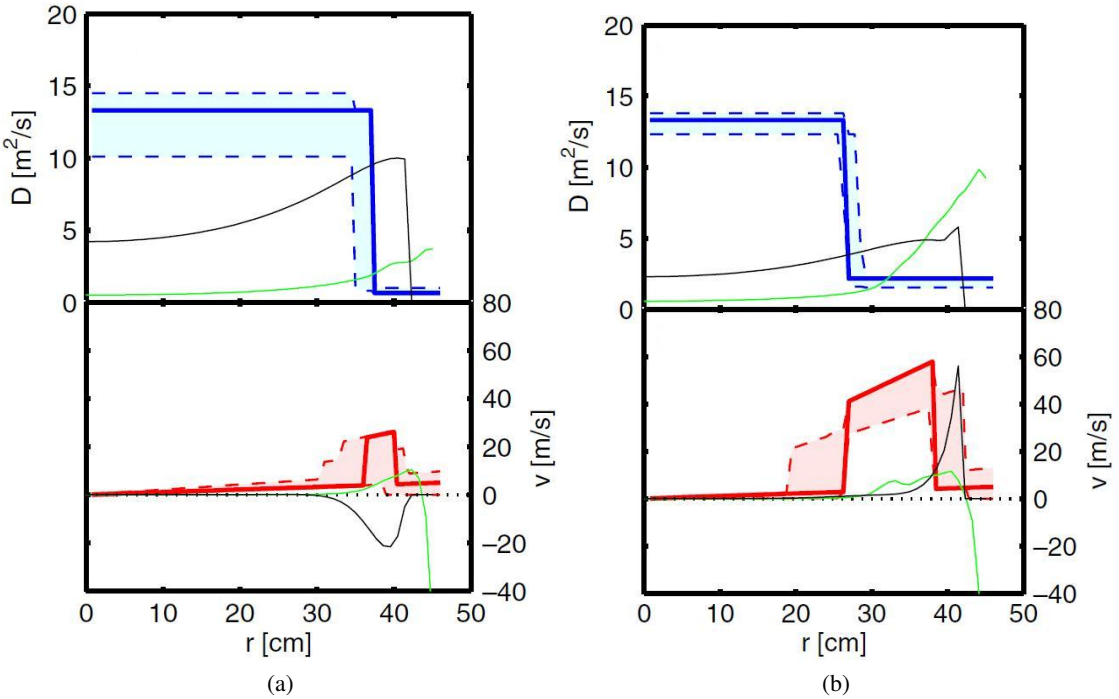

Figure 4.5: Profiles of the transport coefficients D (thick blue) and v (thick red) for Ni determined in MH (a) and QSH (b) regimes with estimated uncertainty ranges indicated by the respective shaded areas. The classical (green) and stochastic (black) D are multiplied by a factor of 10 in (a) and 100 in (b). The classical (green) and stochastic (black) v by a factor of 0.25 in (a) and 4 in (b). [55]

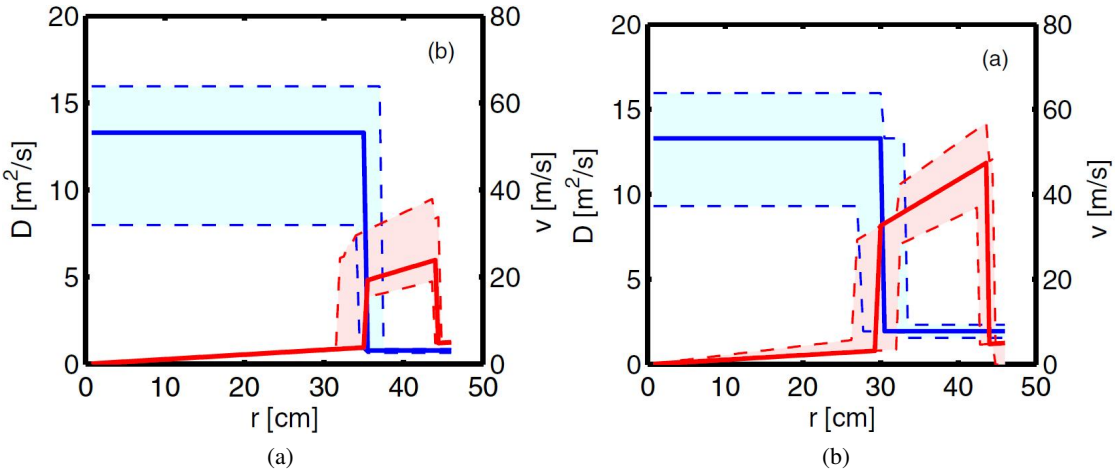

Figure 4.6: Transport coefficients D (blue) and v (red) with estimated uncertainties (shaded areas) for the Ne injection simulation in (a) MH case and (b) QSH case. [55]

4.3 Impurity code for RFX-mod

The code used in this chapter for reproducing experimental plasma emissions is the 1-D collisional-radiative code described in Chapter 3. Here are listed the main inputs to the code. If not explicitly indicated, the profiles assumed in the code have the form described in Section 3.3.

Central electron density, $n_e(r = 0, t)$, comes from the central line-averaged density measured by the two color multichord infrared interferometer [78, 79]. Central electron temperature, $T_e(r=0, t)$, is measured by the double-foil technique Diagnostic Soft X-rays Multifilter (DSXM) [80].

Electron temperature profile, $T_e(r)$, is assumed on the basis of the measurements from the Thomson scattering diagnostic [81] and/or the Diagnostic Soft X-rays multiChannel (DSXC) [82]. In MH regime its profile is in the form described by Eq. (3.5). During QSH phases, in order to account for the steepening of the temperature profiles (Fig. 4.3), the form of the temperature profile in the code is assumed to be

$$\begin{cases} T_e^{QSH}(r) = T_e^{MH}(r) + \left(T_e(0) - T_e^{MH}(0)\right)\left[1 - \left(\frac{r}{r_p}\right)^{\alpha'}\right]^{\beta'} & \text{if } r < r_p \\ T_e^{QSH}(r) = T_e^{MH}(r) & \text{if } r > r_p \end{cases} \tag{4.1}$$

where $T_e^{MH}(r)$ is the temperature profile of the last MH time interval before the beginning of the QSH phase; r_p is normally taken equal to the mid-radius.

Electron density profile, $n_e(r)$, is assumed on the basis of multi-chord interferometer measurements. The interferometer system measures the line-averaged density along 15 chords, and with inversion, yields the full density profile. In the code the profile is fixed in shape and the time evolution is done on the central value (see Eq. (3.6)).

During the pellet penetration into the plasma, the code gets as inputs the actual $T_e(r)$ and $n_e(r)$ profiles directly from the measurements, with their own time resolutions. This allows to better simulate the pellet ablation and the plasma radiative emissions caused by the pellet's particles. $T_e(r)$ comes either from the Diagnostic Soft X-rays multiChannel (DSXC) [82] or the Diagnostic Soft X-rays 3-arrays (DSX3) [83] according to the availability. Both diagnostics determine T_e along several lines-of-sight (LOS) through the double-foil technique with a time resolution of 0.5 ms; the DSXC has 10 LOS while the DSX3 has 19 LOS. $n_e(r)$ is obtained by inverting interferometry measurements up to every 0.1 ms.

Neutral density profile is calculated with the Monte Carlo code NENÈ [49], properly scaled to the measured H_α line emission at the edge of the plasma.

Impurity neutral influxes are calculated by acquiring the light from particular spectral lines with interference filters. For carbon influxes we measure the C II line at 6578 Å, for oxygen the O II line at 4415 Å and for lithium the Li I line at 6707 Å. Particle influxes are calculated using calibrated brightness measurements together with atomic ionisation per photon coefficients S/XB (see Eq. (1.16)) from [59]. In Fig. 4.7 influxes of C and O versus density are shown for high current discharges ($I_p \geq 1$ MA) with different wall conditionings.

Main gas ion temperature is a further input. $T_i(r, t)$ measurements are not available on RFX-mod yet. LOS integrated Doppler broadening measurements on several impurity lines (O VIII, O VII, O V, C V) coupled to simulations of impurity emission profiles indicate $T_i \sim 0.7\, T_e$. T_i is then inserted in the code multiplying the electron temperature by 0.7 and assuming the same profile.

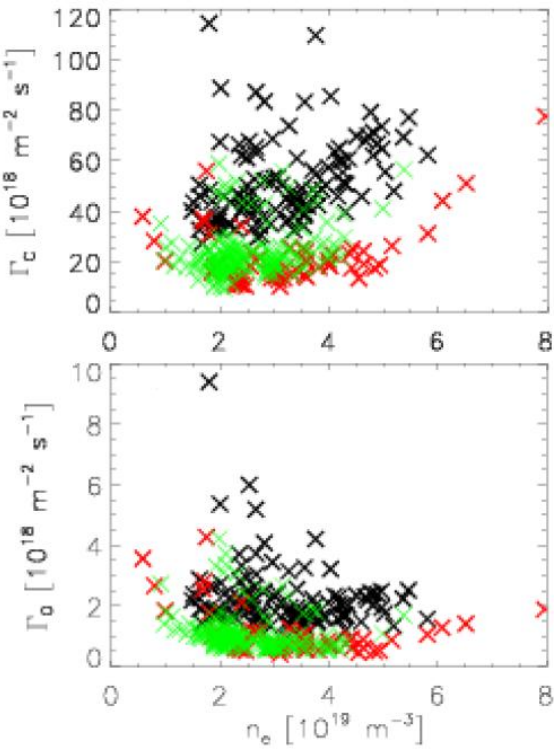

Figure 4.7: Variation of influx of C (up) and O (down) with n_e for 3 sets of discharges: far from wall conditioning (black); with boronised wall (green); and with lithised wall (red). [84]

4.4 Intrinsic carbon and oxygen impurities

My activity on the impurity transport in RFX-mod began with a reconstruction of the radiation emitted by the intrinsic impurities in a typical high current discharge, in which the plasma spontaneously moves back-and-forth from MH to QSH phase throughout the shot. To simulate the radiation from the plasma (SXR and total radiated power), collisional-radiative codes for C and O have been used, which simulate the transport of ions and their radiation, lines and continuum, as well as the continuum from the main gas.

The profiles of the transport coefficients used to simulate intrinsic impurities are shown in Fig. 4.8 for the MH and QSH plasma regimes. Those have been estimated starting from the coefficients found for Ni and Ne (Figs 4.5 and 4.6) and modifying them in order to simulate the emissions from intrinsic impurities. D and v for C and O in MH conditions are similar to what found for Ni and Ne. In QSH conditions the pinch velocity is lower but still outward and wide, confirming the external velocity barrier determined with Ni and Ne experiments. The diffusion coefficient in the core is found to be lower than in the MH regime, in agreement with an improved confinement in the core plasma observed in the main gas behaviour [50].

Those coefficients are changed in time during the simulation according to the plasma regime (MH or QSH), which is identified by the value of the magnetic spectral index N_s [71].

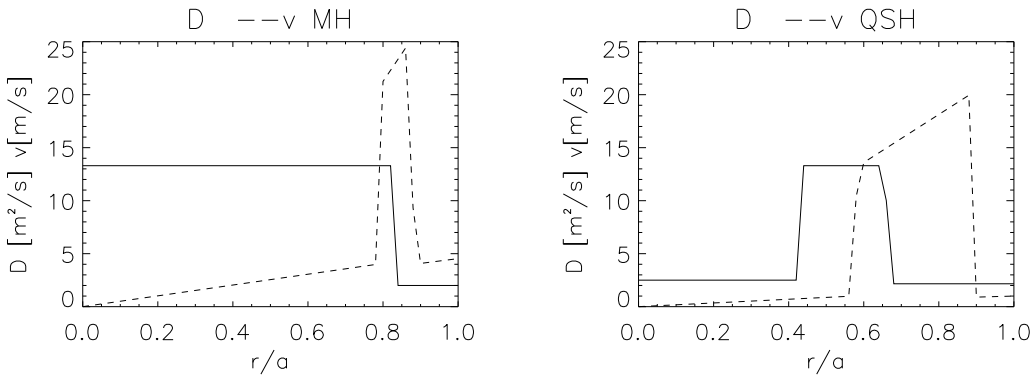

(a) (b)

Figure 4.8: Transport coefficients for carbon and oxygen in MH and QSH regimes.

$$N_s = \left\{ \sum_n \left[\frac{\left(\tilde{b}_\phi^{1,n}\right)^2}{\sum_{n'} \left(\tilde{b}_\phi^{1,n'}\right)^2} \right]^2 \right\}^{-1} \tag{4.2}$$

This spectral index is used to describe the shape of the $m = 1$ mode spectrum. $\tilde{b}_\phi^{1,n}$ is the amplitude of the toroidal component of the magnetic fluctuation due to the (1, n) mode. The plasma is considered to be in QSH when $N_s \leq 2$, while $N_s = 1$ describes a pure SH state.

The chosen shot to be reproduced is #24597, a high current (1.5 MA) hydrogen discharge. In Fig. 4.9 the plasma current and the spectral index (for this shot the QSH threshold has been chosen equal to 1.2). Fig. 4.10 shows the inputs to the code for reproducing the first 150 ms of the discharge.

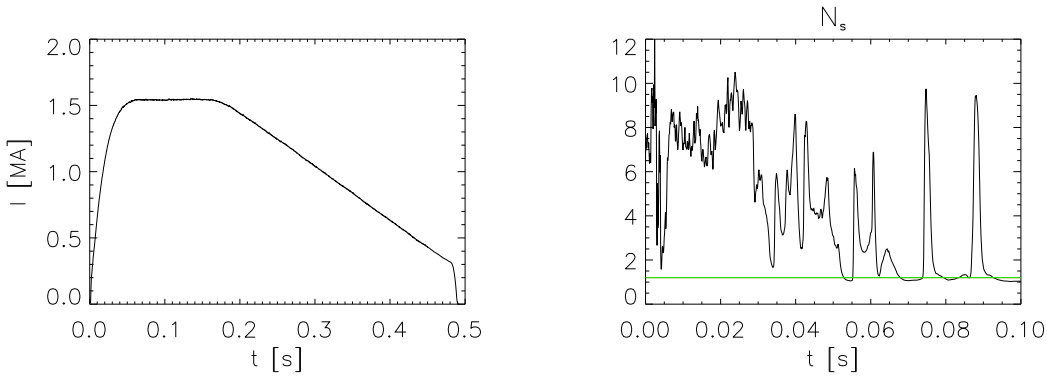

(a) (b)

Figure 4.9: (a) Plasma current. (b) Magnetic spectral index with a green line showing the threshold between MH and QSH regimes.

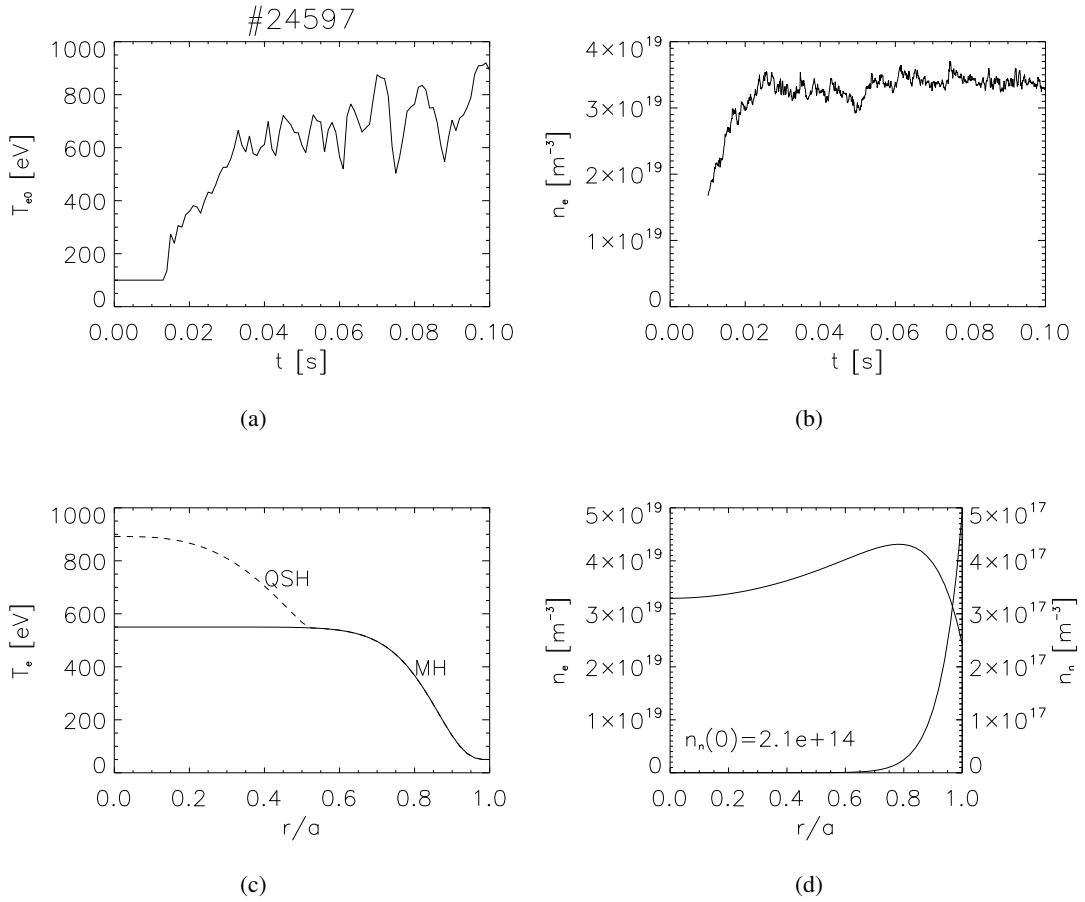

Figure 4.10: Code inputs: (a) Central electron temperature from the double-foil technique. (b) Electron density from the interferometer. (c) Electron temperature profiles for MH and QSH regimes. (d) Electron and neutral density profiles.

The simulation reproduces the central SXR brightness time evolution and brightness profiles which are compared with measurements from the Diagnostic Soft X-rays Tomography (DSXT) [85]. This diagnostic consists of 78 lines-of-sight at the same poloidal cross-section. The detectors are silicon photodiodes with a thickness of 200 μm; it defines the maximum energy of the acquired radiation. Each detector has a beryllium foil of chosen thickness interposed between it and the plasma; it defines the minimum energy of the acquired radiation. The simulation takes into account the absorption of the Si photodiode and the transmissivity of the Be filter in computing the plasma radiation. In this shot installed filters have a thickness of 31 μm to cut off Lyman lines of O. So, only bremsstrahlung and recombination radiation form impurity ions is acquired.

Fig. 4.11(a) shows the simulated SXR emissivity integrated along the diameter which is compared with the measured brightness of the central chord of the SXR tomographic system. Moreover, a precise reconstruction of the evolution of the SXR brightness profiles, as well as the ratio between C VI and C V resonant lines, is reproduced during one of the transitions from MH to QSH (86 - 100 ms). In this time interval the input profiles of electron density and temperature

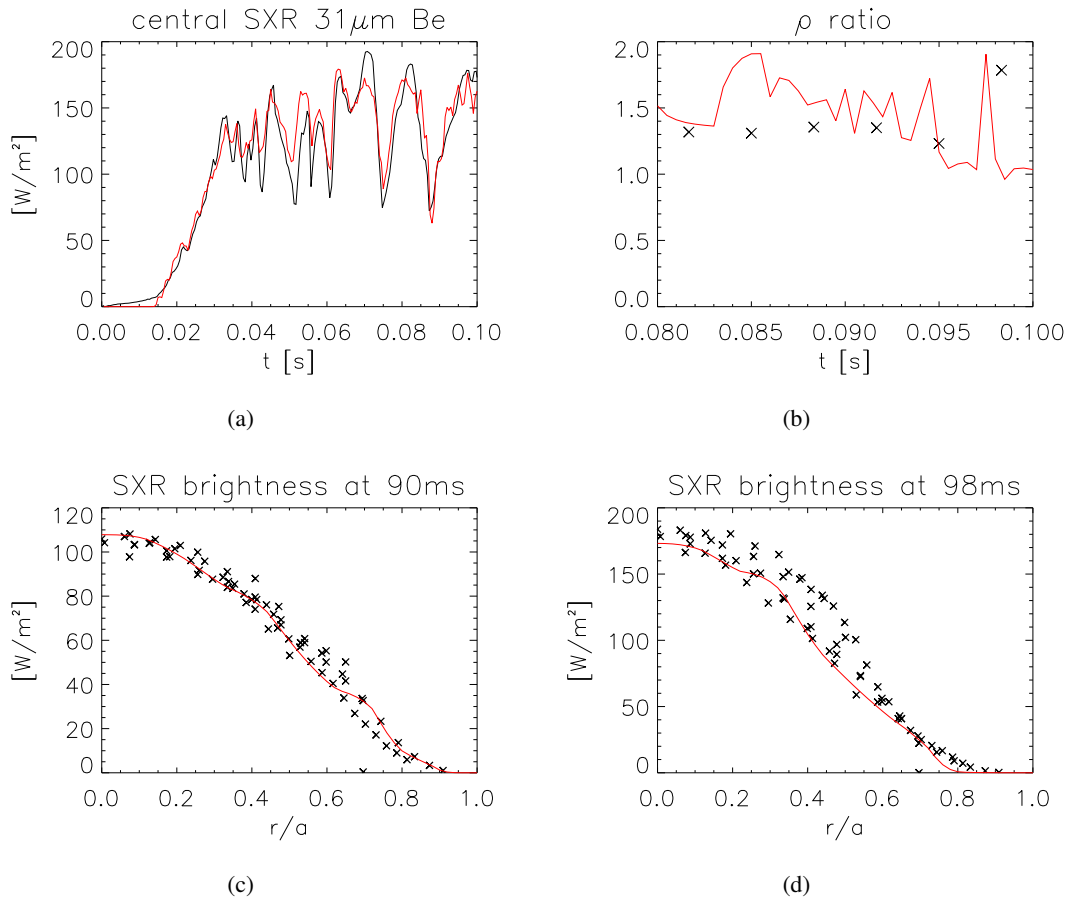

Figure 4.11: (a) Brightness of central chord SXR, measured (black) and simulated (red). (b) Experimental (×) and simulated (red line) ratio between C VI (33.7 Å) and C V (40.3 Å) resonant lines. (c)(d) SXR brightness profiles at different times, measured (×) and simulated (red lines).

come directly from the measurements. Temperature profiles are acquired by the DSXC. Density profiles are obtained by inverting interferometry measurements.

In Figs 4.11(c) and (d) are plotted radial profiles of SXR brightness for two different times corresponding to MH and QSH phases. In MH conditions SXR distributions are poloidally symmetric, apart from an in-out asymmetry due to the Shafranov shift of the plasma column which is ≈ 1 cm [86]. When mapping in MH the data points of various chords to a single radius the spread in the values is small. In QSH conditions strong poloidal asymmetries are present, larger and more localised than the plasma Shafranov shift, caused by the dominance of the single mode ($m = 1, n = -7$) in the magnetic spectrum which results in a local increased emission corresponding to the formation of a magnetic structure [85]. The radial location of this structure corresponds to the resonant radius of that mode, while its poloidal position coincides with the poloidal phases of the corresponding magnetic mode at the tomography toroidal location (Φ_{tor} = 202°). Therefore, internal-external asymmetries are present in the SXR brightness profile and when mapping the data points to a single radius in QSH the spread of the values can be large (see Fig. 4.11(d)).

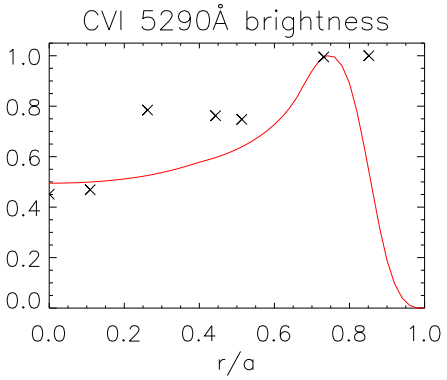

Figure 4.12: Experimental (×) and simulated (red line) brightness profile of C VI 5290 Å emission line.

Fig. 4.11(b) shows the time behaviour of the ratio between C VI (33.7 Å) and C V (40.3 Å) resonant lines; the measured value comes from a XUV grazing incident spectrometer [87]. The brightness of the 5290 Å C VI emission line is also reproduced consistently with the measurements. Brightness measurements of this line were performed on multiple lines-of-sight and averaged during flat-top phases of several discharges [88]. The line is excited by charge-exchange between neutrals and fully ionised carbon ions. The emission profile is shown in Fig. 4.12: it is strongly hollow, due to a combination between the neutral profile and the outward pinch velocity.

Furthermore, the total radiated power is simulated and compared with the radiation acquired by the bolometer [14]. The bolometer array system installed on RFX-mod consists of 36 vertical lines-of-sight, each of them hosting a gold foil resistor. A 4-μm-thick gold foil absorbs the vacuum ultraviolet and soft X-rays down to 0.2 nm. The bolometer has a fairly linear response to radiation power in the wavelength range up to 200 nm, where the reflectivity of gold begins to increase steeply; 40% of the radiation is reflected from 200 to 500 nm and 90% at higher wavelengths [89, 90]. The absorption capability of gold at different wavelengths is taken into account in modelling the radiation.

Total radiation emissivity is therefore dominated by line emission coming from carbon and oxygen, and it is typically concentrated in a small layer at the edge of the plasma. The measured total radiated power is plotted in Fig. 4.13(a) along with the simulation. While the experimental signal displays regular fluctuations, the simulation is nearly flat over the time trace, at a power level compatible with the minima of these fluctuations. The experimental periodicity is a feature of the helical deformation of the plasma column induced by the dominant mode ($m = 1, n = -7$), corresponding to a radial plasma shift on the equatorial plane. This $\Delta_{1,-7}$ shift, in turn, results in an enhancement of the plasma-wall interaction and, consequently, of the emitted radiation (see Fig. 4.13(b)) [75]. The growing in the emissivity is greater when the radial shift is towards the low-field side, because of the in-out asymmetry of the helical structure due to the Shafranov shift of the magnetic axis: the same helical flux surface is closer to the wall in the low-field side than in the high-field side [86]. So, the experimental radiated power in Fig. 4.13(a) is modulated by the $\Delta_{1,-7}$ shift, with higher values occurring when the $\Delta_{1,-7}$ shift points outwards. This magnetic phenomenon cannot be reproduced in a 1D cylindrically symmetric model. Moreover,

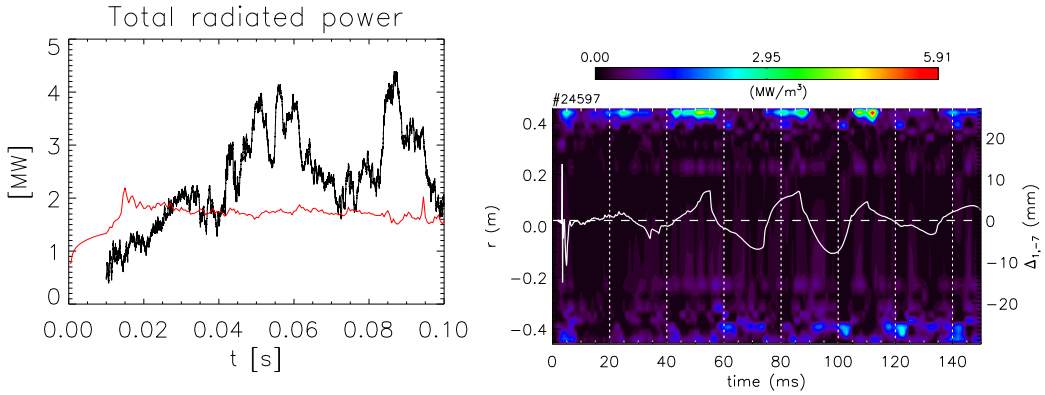

(a) (b)

Figure 4.13: (a) Experimental (black) and simulated (red) total radiated power. (b) Contour plot of the radiated power emissivity with $\Delta_{1,-7}$ shift (white line).

the computation of the radiated power is not very accurate because of a certain inaccuracy in valuating the low ionisation stages of impurity ions due to a poor knowledge of the profiles of T_e and n_e at the edge.

Fig. 4.14 displays the populations of C and O at 100 ms along with the profile of Z_{eff}.

In conclusion, we can say that the agreement between experimental data and simulations is good. The code is able to reproduce both SXR time evolution and brightness profiles, as well as the ratio between the resonant lines. Also the brightness profile of the C VI line is consistent with the measurements. Considering the total radiated power, the simulation is satisfactory coherent with the experimental measurements, strongly asymmetric.

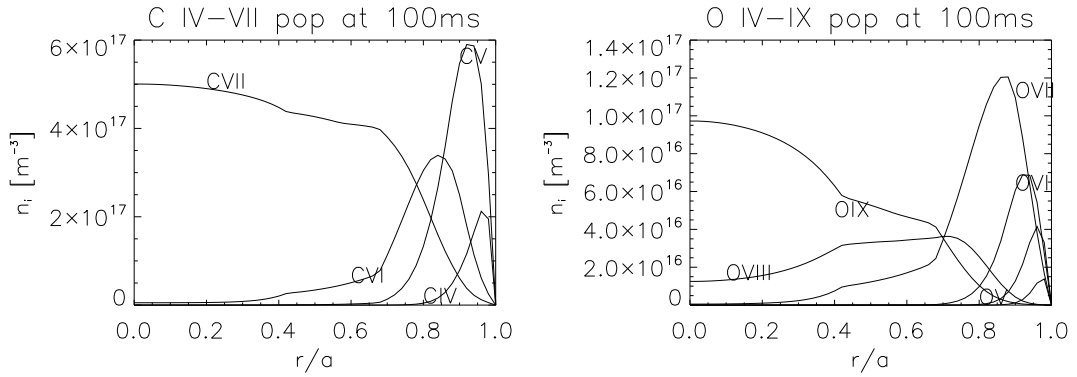

(a)

(b)

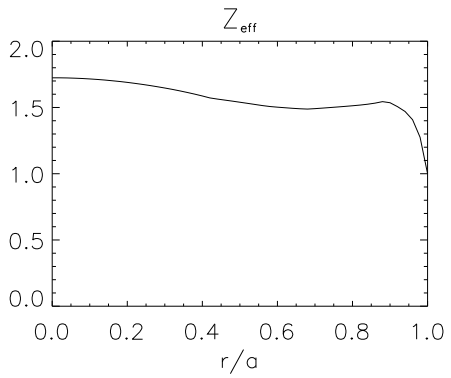

(c)

Figure 4.14: Radial profiles of (a) ion population of C, (b) ion population of O and (c) Z_{eff}.

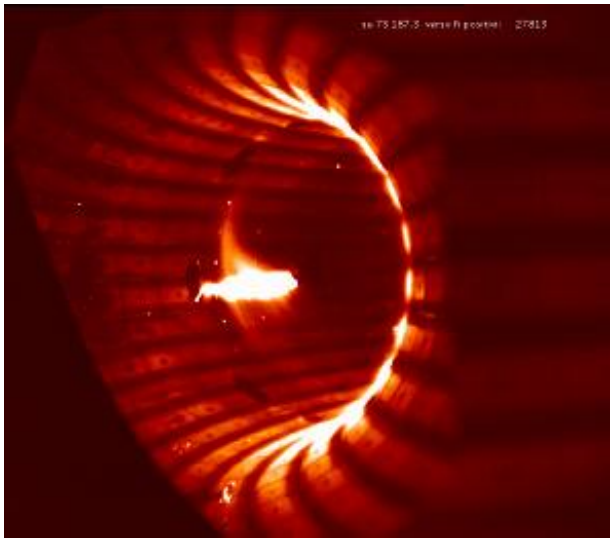

Figure 4.15: Lithium pellet injection seen by a CCD camera.

4.5 Transient experiments through solid pellet injections

Solid pellet injections are simulated in order to determine the transport coefficients separately. Pellet injections originate a variation of the plasma features, e.g. electron density and emitted radiation, which can be followed and reproduced by the code, allowing a better discrimination between the diffusive and convective terms of the particle fluxes. Moreover, pellet injection is a controlled impurity introduction, different from LBO or gas puffing, with well known impurity source dimension and space and time deposition.

Two different experiments are analysed. Lithium pellet injected during lithisation campaign and carbon pellet injected in order to study carbon transport. The ablation of the pellet is reproduced by the code through the ablation model described in Section 3.5.

4.5.1 The injection system and the pellet trajectory reconstruction

Pellets are injected into the chamber through a room temperature pellet injector [68]. The injector allows to inject cylinders of any solid material at room temperature with length from $l \leq 0.1$ mm up to $l = 4.5$ mm and diameter from $\varnothing \leq 0.1$ mm to $\varnothing = 1.5$ mm. Each pellet is contained in a sabot which is pneumatically accelerated along a barrel by a driver gas until it reaches a hollow bumper where it is stopped, while the pellet continues in free flight with the same velocity as before the sabot-bumper impact. With drive pressure of 1-10 bar, velocities of 50-400 m/s can be obtained.

In RFX-mod the injector is used for two different aims. The first is the wall conditioning through lithium pellet injections, with the deposition of a lithium layer on the first wall. The second is the analysis of the impurity transport through the injection of a known source of impurities. Smaller size pellets are the ones useful for plasma studies, while larger ones are for wall conditioning.

The injector is made of three main parts: the sabot loader, the gun and the sabot recovery system. An image is shown in Fig. 4.16. The loader is a vertical cylinder holding up to 25 sabots,

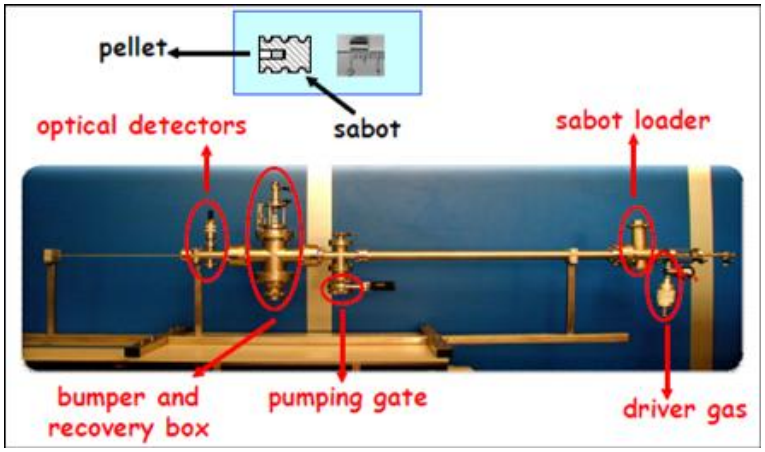

Figure 4.16: The room temperature pellet injector.

preloaded with the pellets. Below the loader a hollow cylinder keeps the gun barrel vacuum tight. A loading mechanism based on a pneumatic transducer pulls back the cylinder and allows one sabot into a U-shaped lodging at the end of the barrel. The cylinder is then advanced to shut the barrel again and to push the sabot into the barrel. The sabot is accelerated by opening a fast electromagnetic valve which lets in the driver gas. To recover the sabot a second pneumatic transducer lifts the bumper and permits the expulsion of the sabot into a recovery box, which is obtained by slightly raising the pressure in the barrel. The injector is also equipped with two optical detectors that provide the measurement of the pellet speed.

Once a pellet is launched from the injector inside the plasma, it is important to monitor its trajectory, which will then be inserted in the impurity transport code as input. To measure the trajectory it is exploited the radiation coming from the ablated particles surrounding the pellet, called *ablation cloud*. A system based on two absolutely calibrated two dimensional Position Sensitive Detectors (PSD) is used to collect the emitted light [91]. A PSD provides a measurement of the coordinates of the baricenter of the light incident on the detector sensitive area. The measurement of the angle of the pellet cloud by a PSD array is obtained by mapping the image of the cigar-shaped cloud on the array and fitting a line to the resulting sliced image baricenters.

Two PSDs are installed at the pellet injection section, one looking at the pellet from behind, to have a measurement of the toroidal and poloidal defections, one from the bottom, to have a measurement of the toroidal defection and of the radial motion. The deflections in both directions are most likely due to the presence of a distortion in the electrons Maxwellian distribution function that enhance the pellet ablation on the electronic drift side. Because of the momentum conservation, the asymmetry of the ablation process causes a "rocket effect" which accelerates the pellets along magnetic field lines in the direction of the electron drift [92]. Fig. 4.17 shows an example of the reconstructed trajectory of a pellet in the poloidal and in the toroidal planes.

4.5.2 Carbon pellet injection

Transient experiments with injection of small carbon pellets have been carried out during this Ph.D. activity in order to assess carbon transport and validate the transport coefficients previ-

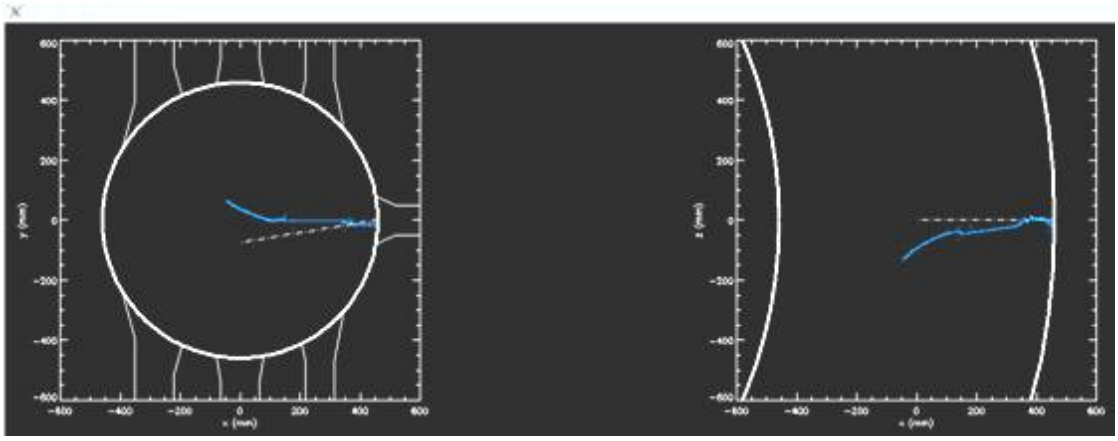

Figure 4.17: Carbon pellet trajectory (blue line) reconstructed by the PSD detectors in the poloidal and toroidal planes. Dotted line represents the pellet injection line.

ously determined for intrinsic impurities by reproducing the enhancement in the experimental signals (density and plasma radiation).

A first attempt was made using very small graphite spheres whose radius was about 200 μm. However the injector evidenced problems with such small pellets which almost invariably could not reach the plasma. After that, home-made graphite cylinders were created with larger size: $l \sim 1$ mm, $\varnothing = 0.7$ mm. With these pellets the succeeding rate increased and some shots resulted in a good penetration and were simulated. The results of this analysis are presented in the following.

During a carbon pellet injection the amount of C atoms entering the plasma is relatively small, of the order of 10^{19}, resulting in a limited perturbation of the plasma, whose original properties are quickly restored in a few tens of milliseconds after the injection. This allows the carbon pellet experiments to be carried out parasitically in high current discharges ($I_p \geq 1$ MA), normally at the end of the flat-top phase.

Shot #1

The first shot presented in this work is a He discharge. Plasma current is shown in Fig. 4.18. The pellet is injected at ~ 180 ms when the plasma current start decreasing. Its velocity is ~ 100 m/s. PSD detectors reconstruct the pellet trajectory in the poloidal and toroidal direction (see Fig. 4.17 which refers to this shot) and from this the pellet radial position is obtained. In this shot the pellet deflects from the centre of the chamber, leaving the area covered by the PSDs before being completely ablated. However, from the image recorded by a camera showing the pellet trajectory, it seems that the pellet radial position does not vary after the pellet leaves the detectors cones of view, as reported in Fig. 4.19(a).

The pellet is assumed to be spherical and is inserted in the code as a moving impurity source. Its ablation due to the incident electron flux is computed taking into account the local value of density and temperature (see Eq. 3.10). During the pellet penetration in the plasma the input profiles of electron density and temperature come directly from the measurements in order to have detailed time dependent information of the plasma characteristics surrounding the pellet. From the pellet ablation the impurity influx is determined. Fig. 4.19(b) shows the calculated

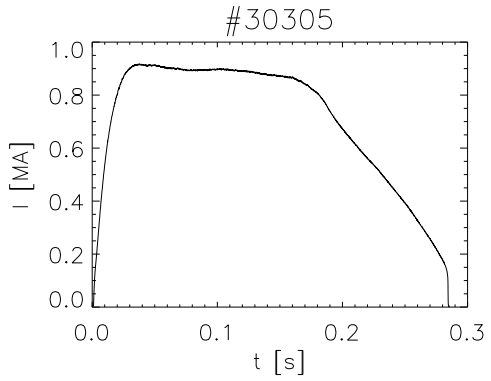

Figure 4.18: Plasma current.

reduction of the pellet radius due to its ablation.

The pellet is injected during a long-lasting MH period. It is totally ablated in about 13 ms. The simulation is compared with the experimental signals showing the effect of the pellet. In Fig. 4.20 the time traces of the experimental signals are compared with the corresponding simulations. The injection is clearly seen in the enhancement of the electron density, SXR emissions, total radiated power, as well as C VI line. The simulated n_e is obtained from the ionisation of the ablated carbon atoms, adding the pre-injection value of n_e. The pre-injection contribution of the radiative emissions from intrinsic impurities and main gas is calculated running the oxygen CR code along with the carbon CR code.

Fig. 4.21 shows normalised experimental SXR profiles along with their simulated counterparts for different times during (Figs 4.21(a)-(b)) and after the pellet ablation (Figs 4.21(c)-(d)). In the first profiles the spread of the experimental brightnesses mapped to a single radius is greater, due to the presence of radiated particles from the pellet. Once the ablation is completed the poloidal symmetry of the SXR emissions, property of the MH states, is restored and the spread of the points is reduced. The simulated curve well fits the experimental points.

The simulation reproduces satisfactorily the time evolution of the measured quantities as well as the SXR profiles. The used transport coefficients are those in Fig. 4.8 assumed for the intrinsic impurities. This transient experiment conducted during the MH phase confirms the MH transport coefficients for carbon.

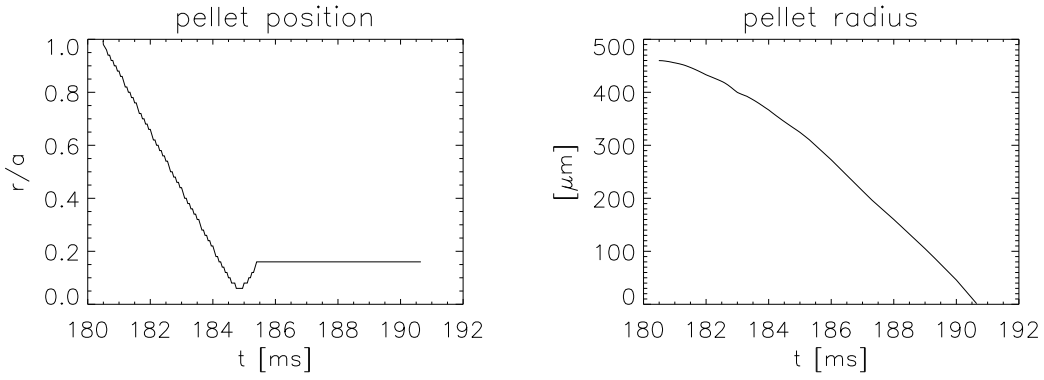

(a) (b)

Figure 4.19: Code inputs: (a) Pellet radial position. (b) Pellet radius.

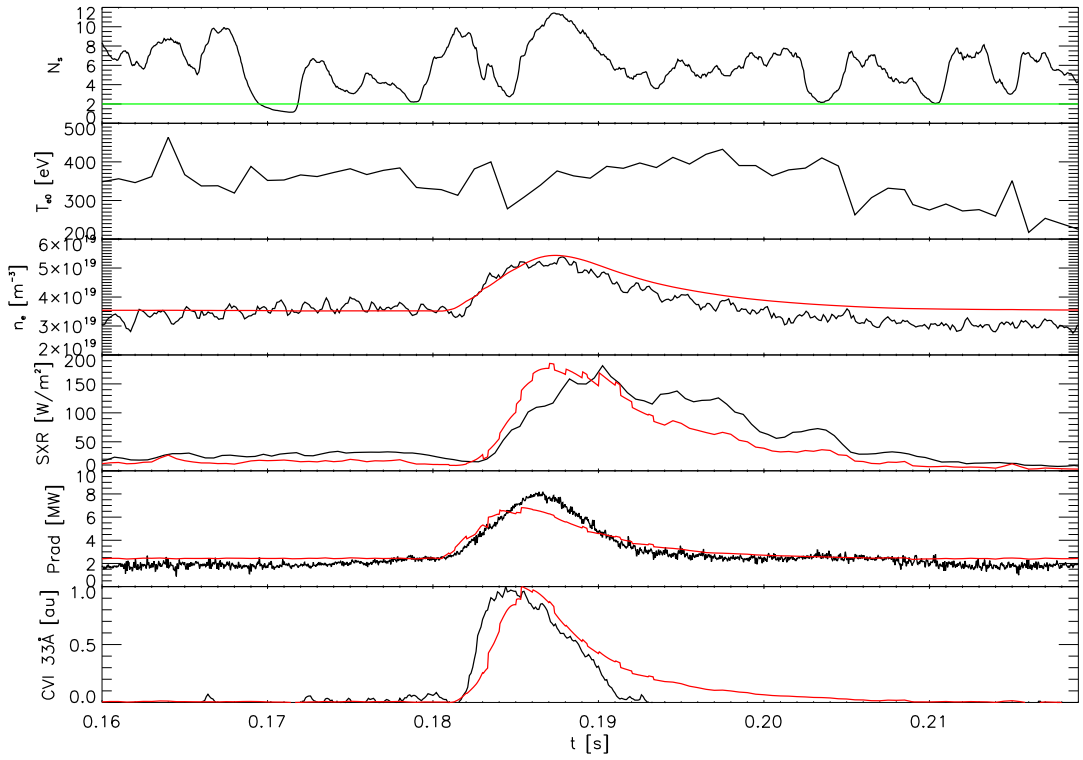

Figure 4.20: C pellet injection at 181 ms. Experimental (black) and simulated (red) plasma signals. [top to bottom] Magnetic spectral index with MH-QSH threshold in green. Central electron temperature. Line-averaged electron density. Central chord SXR brightness. Total radiated power. Normalised brightness of C VI 33 Å line.

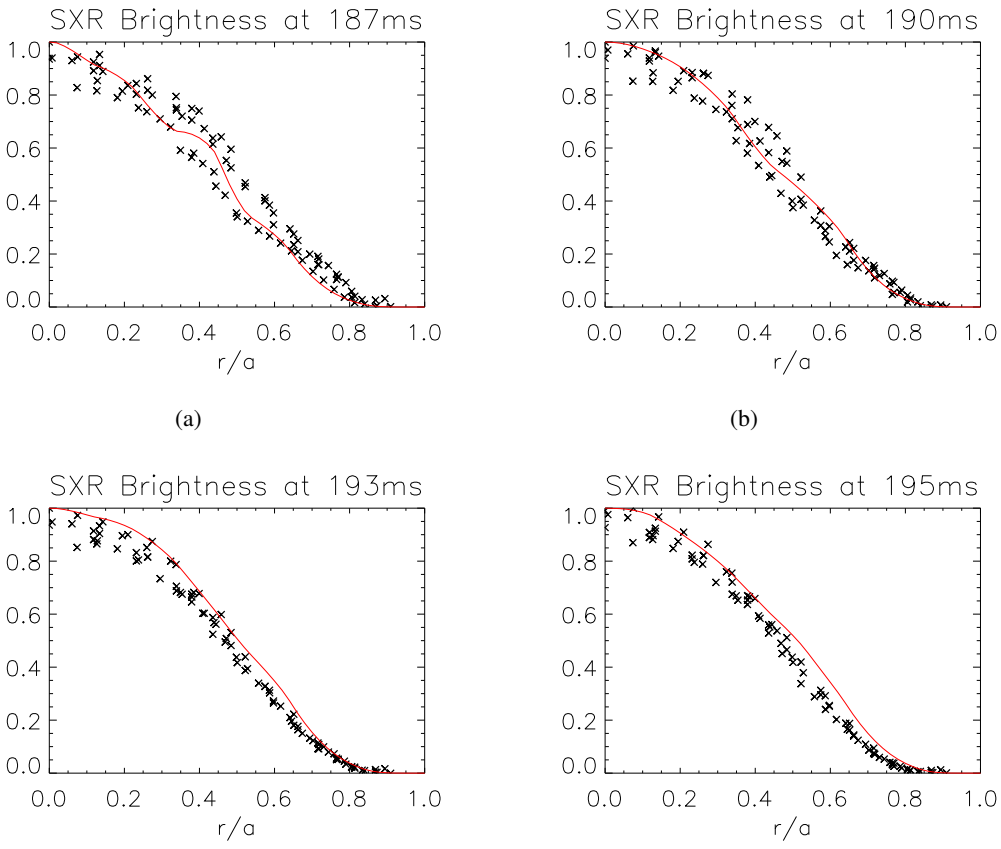

(a) (b)

(c) (d)

Figure 4.21: Normalised SXR brightness profiles after pellet injection. Experimental (×) and simulated (red).

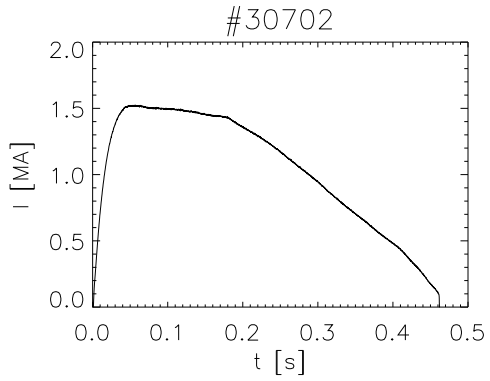

Figure 4.22: Plasma current.

Shot #2

The second shot with carbon pellet injection presented in this thesis is a H discharge. Plasma current is shown in Fig. 4.22. The pellet is injected at 177 ms, at the end of the flat-top phase, with a velocity of 120 m/s. Its trajectory inside the plasma is computed by the PSDs, the radial component is plotted in Fig. 4.23(a) and used by the code as the radial position of the penetrating carbon sphere. The pellet, once reached the plasma core, leaves the area covered by the detectors; in this case there are no sign of radial deflection as in the previous shot and, assuming constant radial velocity, the trajectory is extended to the second half of the chamber until the pellet is totally ablated. Fig. 4.23(b) shows the reduction of the pellet's radius computed by the ablation model.

The simulation is compared with the experimental signals showing the effect of the pellet. In Fig. 4.24 the pellet ablation and consequent ionisation of its atoms caused the electron density, SXR emissions and C VI line to raise. These experimental signals are reproduced by the code. Radiated power was not available during this shot, nor were SXR brightness profiles. Only the central chord SXR signal was available by the Diagnostic Soft X-rays Multifilter (DSXM); the chosen brightness to be reproduced is the one filtered by 300 μm of beryllium.

In this shot the pellet is injected during a QSH phase, which immediately collapses in MH due to the pellet perturbation which increases n_e close to the QSH critical density ($\approx 0.35\, n_G$, in this case $\sim 8 \times 10^{19} m^{-3}$). Following this collapse the temperature drops. Once the ablation is completed, the density diffuses leading its chord-averaged value to the original one; QSH phases return to appear and the temperature increases.

The simulation is able to reproduce the enhancement in the density and the peak value of the SXR emissions, corresponding to the end of the ablation. After the ablation SXR emissions remain at high values for a long time, despite n_e and C line emission return to low levels. This phenomenon can not be reproduced with the simulation.

The simulation is performed using the transport coefficients assumed for the intrinsic impurities (Fig. 4.8), changing between MH and QSH coefficients according to the plasma regime, identified by the magnetic spectral index.

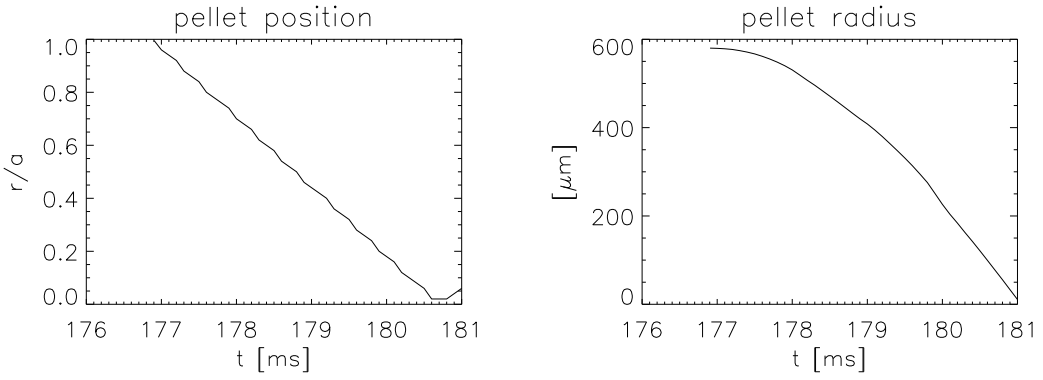

(a) (b)

Figure 4.23: Code inputs: (a) Pellet radial position. (b) Pellet radius.

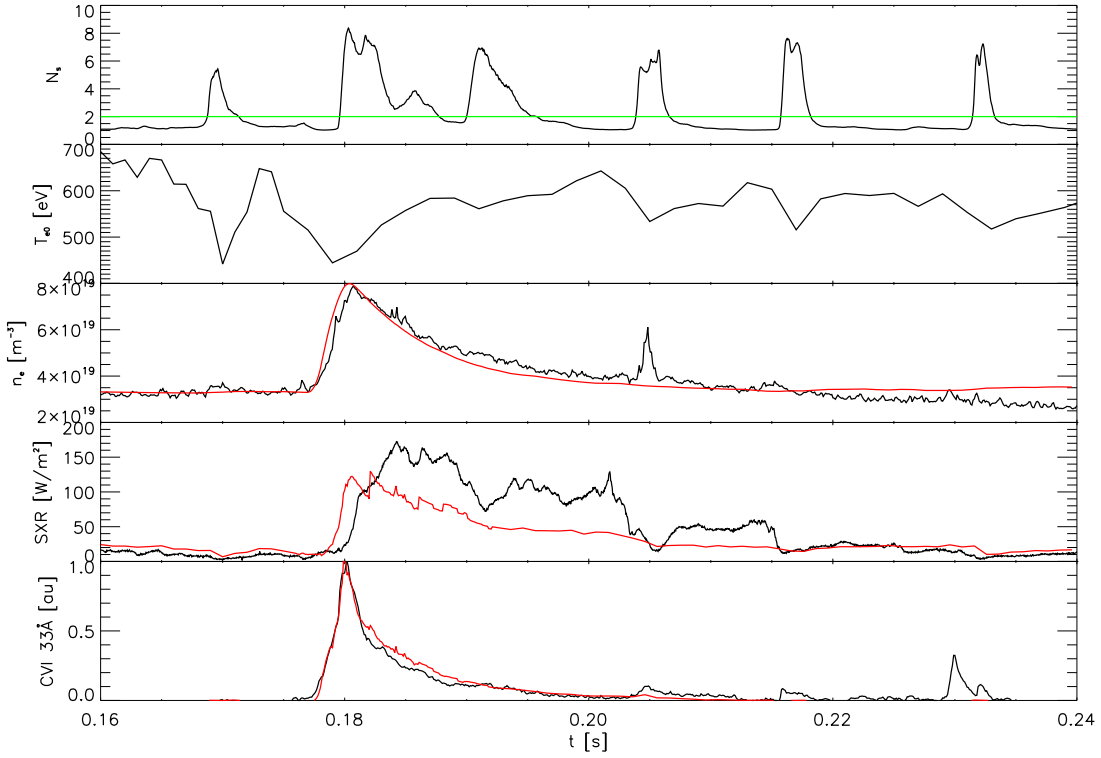

Figure 4.24: C pellet injection at 177 ms. Experimental (black) and simulated (red) plasma signals. [top to bottom] Magnetic spectral index with MH-QSH threshold in green. Central electron temperature. Line-averaged electron density. Central chord SXR brightness. Normalised brightness of C VI 33 Å line.

These simulations of transient experiments conducted through carbon pellet injections have been of great importance for validating the transport coefficients assumed for the intrinsic impurities. Unfortunately only a few shots have been carried out successfully, due to experimental problems with such small pellets, and so the simulation has had to rely only on a few discharges. More experiments are needed to fully validate those coefficients. However these reproductions can be considered satisfactory and lead to a first assessment of D and v.

4.5.3 Lithium pellet injection

As previously explained, injections of lithium pellet are routinely used in RFX-mod to condition the graphite wall. These experiments are also a very useful tool to characterise lithium transport by reproducing the variation of plasma emission and density after the injection through the Li CR code. This code has never been used and the simulation of those discharges is a useful benchmark.

Lithium pellets are cylinders with length $l = 4.5$ mm and diameter $\varnothing = 1.5$ mm. They contain about 4×10^{20} atoms and once ablated and ionised they produce an increase in the electron density of the order of 10^{20} m^{-3} which causes the density to exceed the QSH density limit ($0.35\, n_G$). For this reason these discharges are simulated in MH conditions.

Pellets are injected with a velocity in the range 100-130 m/s in order to provide a complete ablation of the pellet close to the plasma centre. From the pellet trajectory reconstructed by the PSD detectors the pellet radial position is obtained.

The shots analysed below belong to a lithisation campaign executed in high current H discharges. In Fig. 4.25 the plasma current of one of these discharges. The pellets are injected at the end of the flat-top phase.

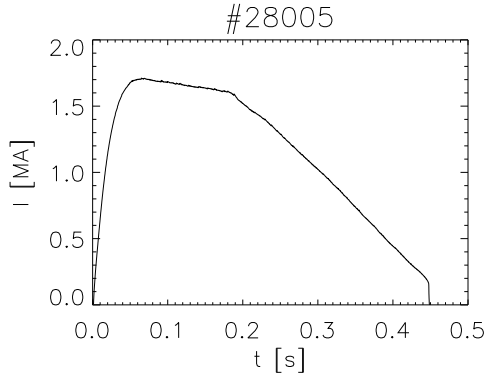

Figure 4.25: Plasma current.

Shot # 1

In this shot the pellet is injected at 185 ms with a velocity of $\sim$ 130 m/s. Pellet's radial position and radius evolution are shown in Fig. 4.26.

The simulation is compared with the experimental signals which show the effects of the pellet. The injection is clearly evident in the enhancement of the electron density and SXR emissions. The effects of the pellet can be seen in the time traces of the experimental signals

in Fig. 4.27, along with the corresponding simulations. The simulated n_e is obtained from the ionisation of the ablated lithium atoms, adding the pre-injection value of n_e. The pre-injection contribution of the SXR emissions from intrinsic impurities and main gas is calculated running the carbon and oxygen CR codes. Total radiated power is computed by the Li CR code but, since it results to be an order greater than the measurements, it is not plotted. The reason for this discrepancy will be given below.

Fig. 4.28 shows measured SXR profiles along with their simulated counterparts after pellet's ablation. The reproduction is good.

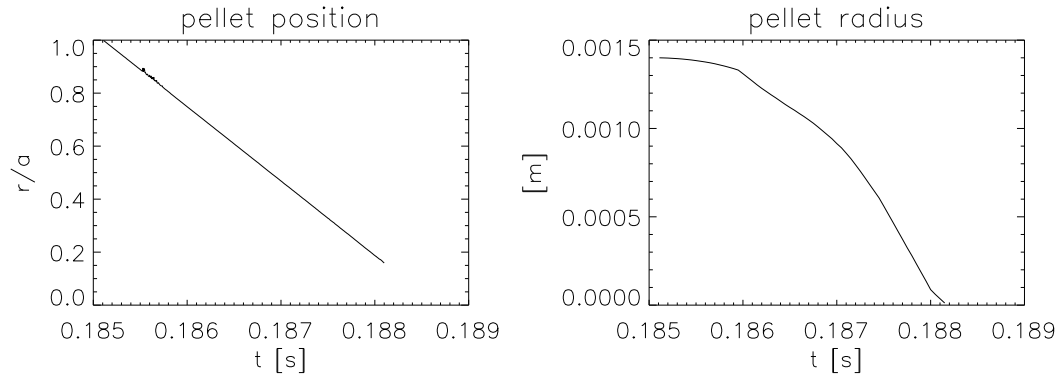

(a) (b)

Figure 4.26: Code inputs: (a) Pellet radial position. (b) Pellet radius.

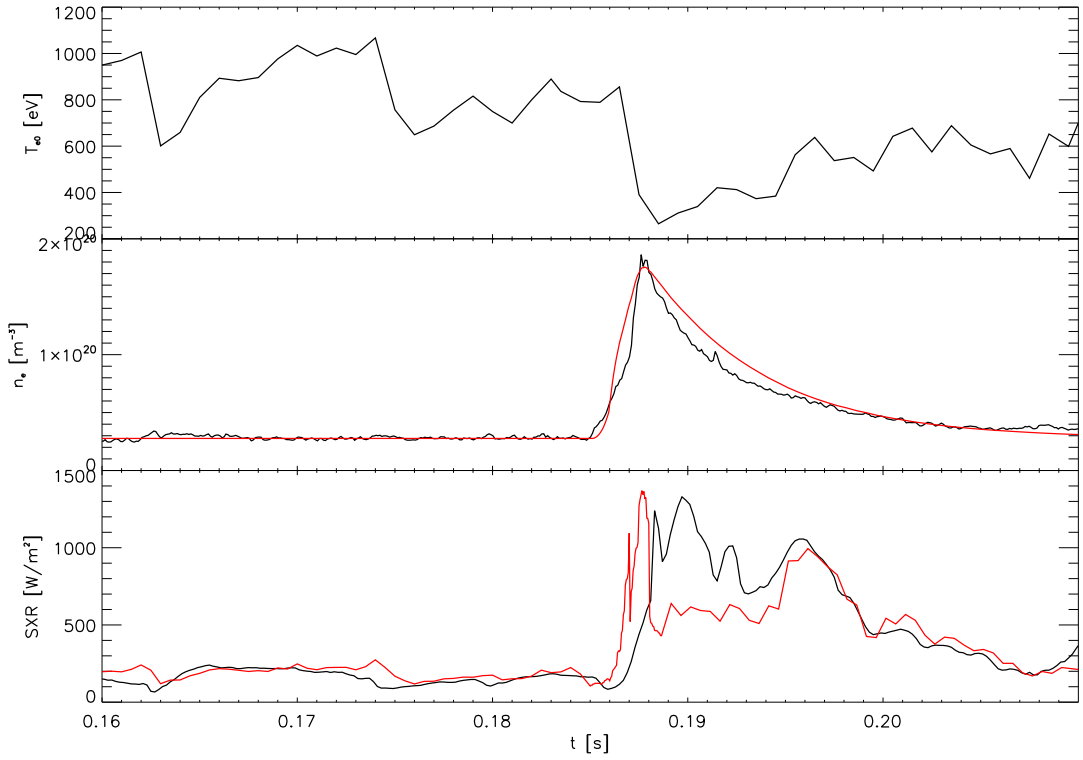

Figure 4.27: Li pellet injection at 185 ms. Experimental (black) and simulated (red) plasma signals. [top to bottom] Central electron temperature. Line-averaged electron density. Central chord SXR brightness.

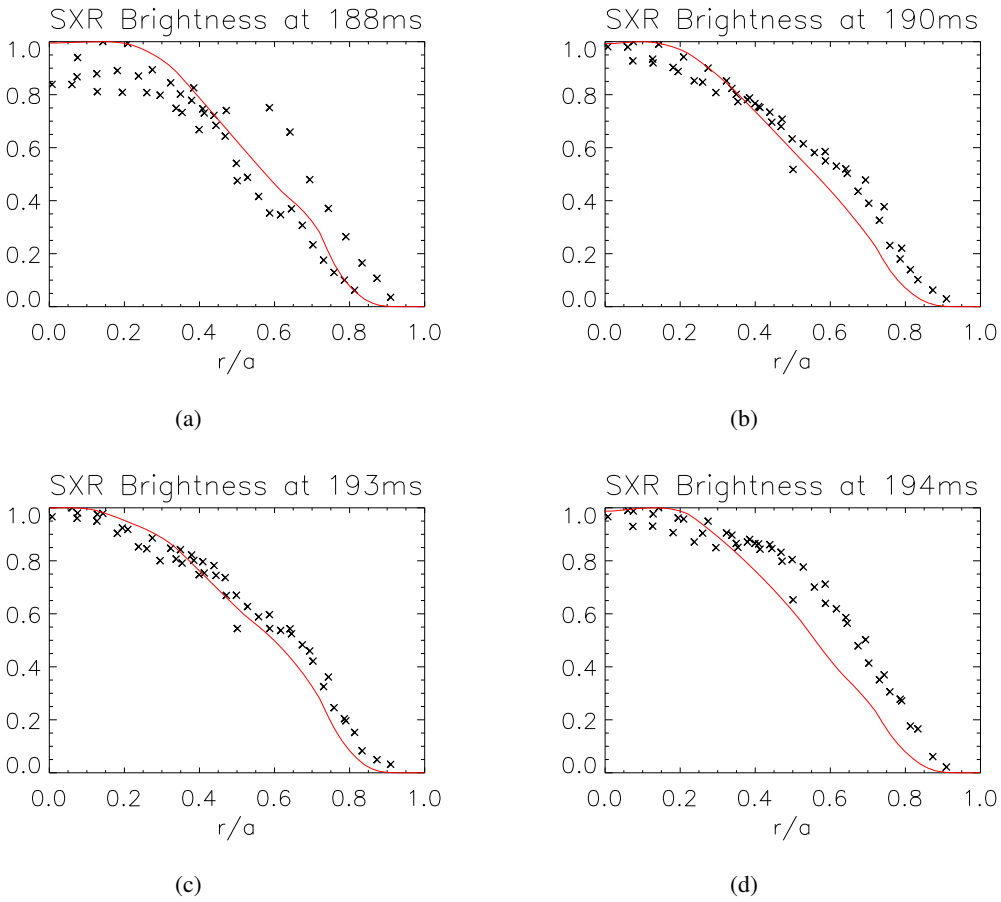

Figure 4.28: Normalised SXR brightness profiles after pellet ablation. Experimental (×) and simulated (red).

Shot # 2

In this shot the pellet is injected at 186 ms with a velocity of ∼ 120 m/s. Pellet's radial position and radius evolution are shown in Fig. 4.29.

In Fig. 4.30 are plotted the experimental signals showing the modification of the plasma properties due to the pellet ablation and the simulated counterparts. Fig. 4.31 shows measured and simulated SXR profiles after pellet's ablation. The reproduction is very good.

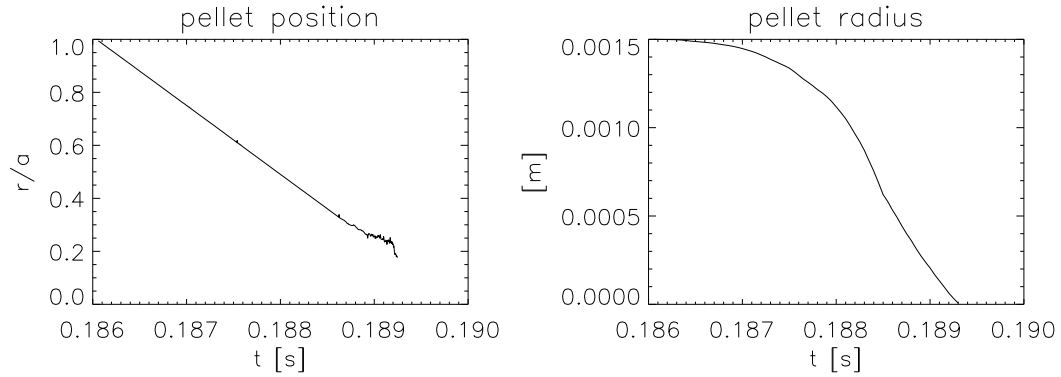

(a) (b)

Figure 4.29: Code inputs: (a) Pellet radial position. (b) Pellet radius.

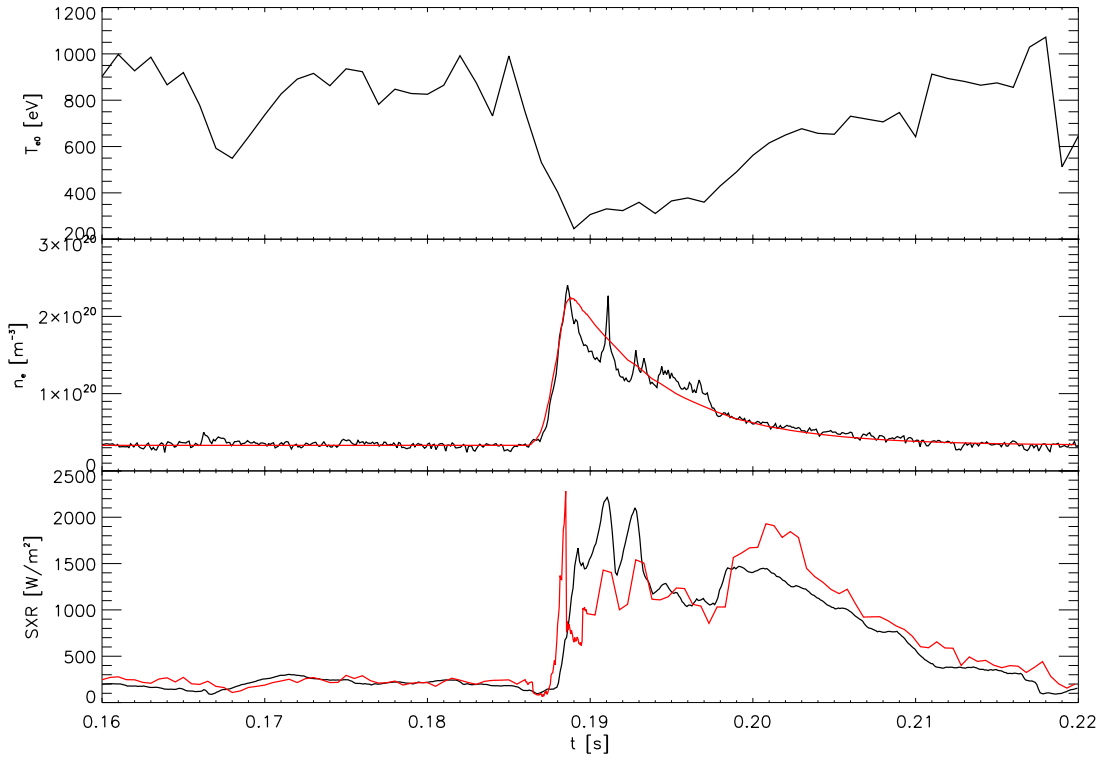

Figure 4.30: Li pellet injection at 186 ms. Experimental (black) and simulated (red) plasma signals. [top to bottom] Central electron temperature. Line-averaged electron density. Central chord SXR brightness.

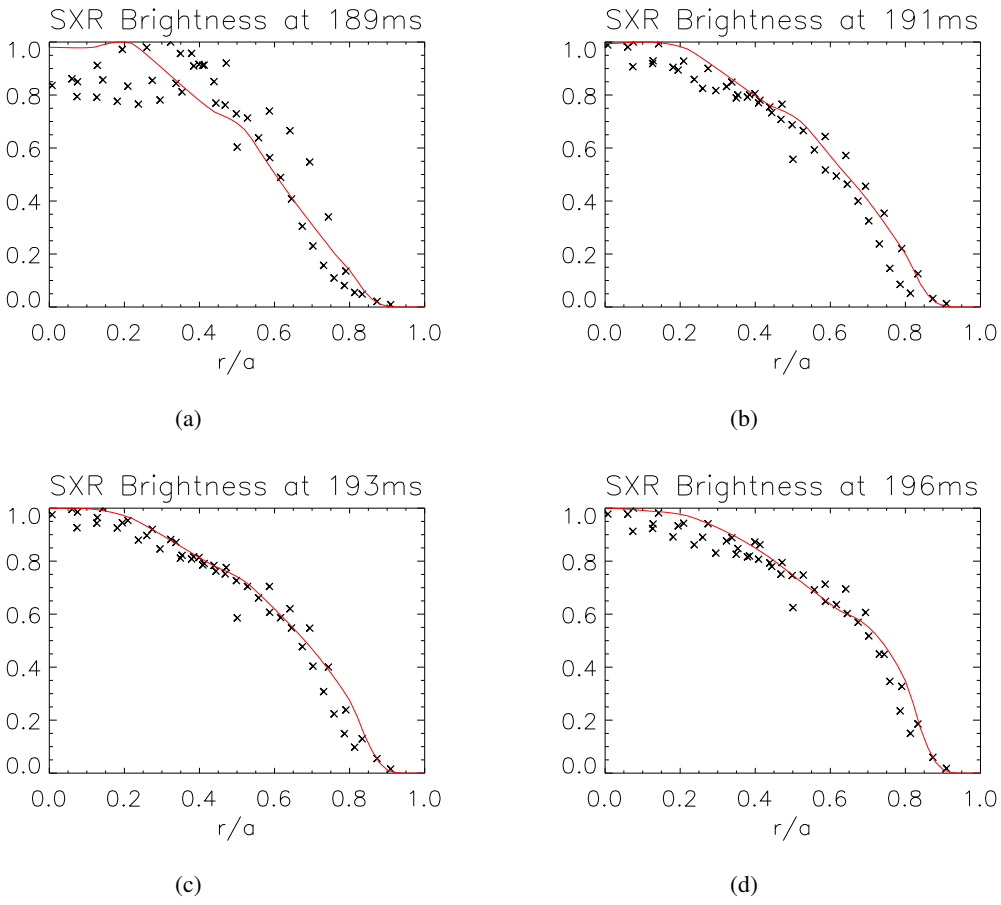

(a) (b) (c) (d)

Figure 4.31: Normalised SXR brightness profiles after pellet ablation. Experimental (×) and simulated (red).

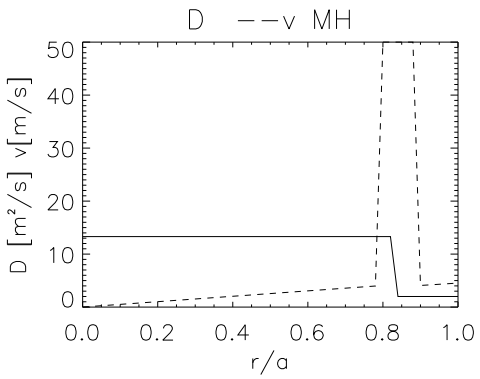

Figure 4.32: Transport coefficients estimated for lithium in MH conditions.

The estimated transport coefficients for lithium are plotted in Fig. 4.32. D is equal to what found in MH conditions for intrinsic impurities (Fig. 4.8(a)) and for Ni and Ne (Figs 4.5(a) and 4.6(a)). v is still outward and forms a barrier near the edge, but in this case it is found higher in magnitude. The principal features of the transport coefficients are therefore maintained between the different elements, confirming the weak dependence of the impurity transport in RFX-mod on the charge/mass of the species.

From the results of the lithisation campaign it turns out that Li deposition on the wall suffers of great non-uniformity. A strong localised Li deposition emerges; lithium gets deposited on $\approx 30-50\%$ of the total surface, along the direction of the plasma rotation [77]. This is thought to be the reason why the bolometer signal is well below the simulated radiation from Li ions. Since the bolometer is located far away from the injection point ($\Phi_{tor} = 202°$ for the bolometer, while the injector is located at $\Phi_{tor} = 262°$), and since the acquired radiation comes predominantly from low ionisation stages located near the edge, the actual signal measured by the bolometer is far below the simulated radiation.

Different is the case of the SXR radiation, measured at the same toroidal location of the bolometer. In this case the radiation comes predominantly from the plasma centre, as it is evident from the brightness profiles in Figs 4.28 and 4.31. Li ions in the core region move to the SXR detector position through the toroidal plasma rotation (which is faster in the central region). Therefore the measured SXR radiation is compatible with the 1D simulation.

4.6 Tungsten laser blow-off

A possible candidate for the renewal of the RFX-mod's first wall is tungsten. The principal reason of this wall change is to overcome the high H retention and recycling, property of the graphite wall, which is a great limitation for RFX-mod performance, making very difficult to control n_e. Tungsten instead has a lower H retention, very high melting point, high erosion resistance, which makes it an ideal candidate for a first wall of a fusion device. Indeed, it has been chosen as a suitable material for ITER's divertor.

On the other hand, moving to a higher Z element means that the radiation losses due to the impurities released by the wall will increase. This may be a serious concern especially if impurities penetrate towards the plasma core where the temperature is high but not enough to fully ionise W atoms; the line radiation emitted by W ions may be very strong and eventually lead to a cooling of the plasma and to a premature end of the discharge.

In this context a transport study of tungsten in the RFX-mod plasmas is mandatory to understand whether W tends to accumulate in the core or remains confined in the external region. A complete transport analysis would require to simulate the W behaviour in the plasma with a CR code. Unfortunately a W CR is not available; the fusion community only very recently has made efforts in order to build such code with a superstage treatment [19] (due to the high Z the number of equations in the impurity system is very large and the system solution is quite heavy). So, whether or not W penetrates the plasma core is qualitatively deduced from experimental data.

At RFX-mod W transport experiments have begun very recently by injecting low quantity of tungsten through laser blow-off (LBO). Below are discussed the experimental set-up and the results of the injections.

4.6.1 Laser blow-off system

LBO technique is intended as a weakly perturbative tool; the level of perturbation is low since the number of ablated particles is $1 \div 2 \times 10^{19}$, whereas those entering the plasma are much less. In normal conditions effects of local plasma cooling (due to enhanced radiative losses) are not important.

Tungsten film of a few micrometres is deposited over glass slides acting as substrate; these slides are mounted away from the plasma, looking at it with their metallised faces. Material injection is performed via laser ablation: a laser beam is directed to the slice and deposits its energy on the metal film which is vaporised and whose particles travel ballistically to the plasma, with velocities of the order of a few km/s.

The layout of the system installed at RFX-mod is shown in Fig. 4.33. The laser in use is a Q-switched ruby laser ($\lambda = 694.3$ nm) with a pulse length of 30 ns [93]. Its beam is intercepted and deviated with a group of 5 mirrors under the floor level of the experimental hall to reach the diagnostic port with LBO targets. Before the vacuum window, it is focused by a lens in order to obtain a spot of proper size ($\varnothing = 6$ mm) on the glass slide.

Multiple targets (dimensions 20×90 mm) can be mounted on a drum loader and are changed rotating the drum. To verify the spot, the target is seen by a CCD camera mounted behind the last mirror and looking at the target through the focusing lens.

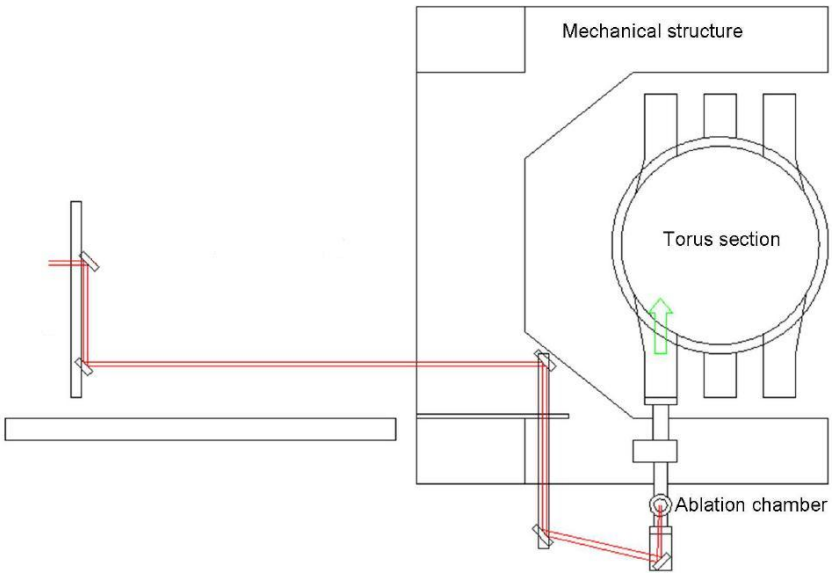

(a)

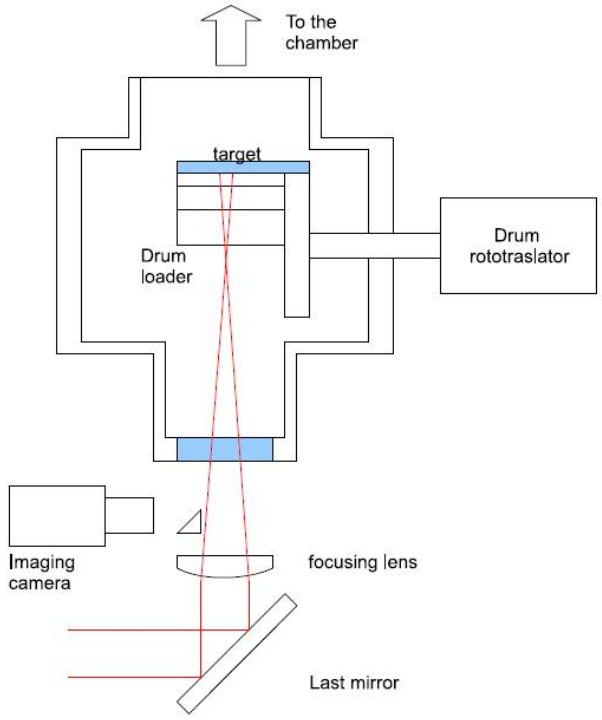

(b)

Figure 4.33: Sketch of the laser beam path to LBO system (a) and of the ablation chamber (b).

4.6.2 W injection and ionisation balance

LBO injections have been performed in high current ($\sim$ 1.4 MA) H discharges, in the flat-top phase, at $\sim$ 70 ms, during a QSH period. Fig. 4.35 shows the time traces of plasma properties during the tungsten injection. Central T_e is about 700 eV, while line-average n_e about 3×10^{19} m^{-3}. After the LBO SXR emissions and radiated power raise. The technique is weakly perturbative, the amount of injected particle being well below n_e, so we notice no effect on temperature and on the magnetic properties of the plasma which remains in QSH regime (look at the first plot in Fig. 4.35).

After having raised following the W injection, the decay of radiated power and SXR emission is fast: the time constant of the exponential decay is about 4 ms. In the past Ni LBO injections the exponential decay had a time constant of 8 ms in QSH conditions and Ni did not progress in the core plasma [55]. The shorter decay time of tungsten may be seen as a first indication that tungsten ions, like nickel, do not penetrate much in the plasma core and remain mainly near the edge, otherwise the radiation decay would have been slower.

Fractional abundances of tungsten ions in ionisation equilibrium are computed using ADAS405 without transport effects, using the values of temperature and density reported above. Ionisation and recombination rate coefficients were assembled by T. Pütterich for analysis at Asdex Upgrade [94]. Charge-exchange rate coefficients are still not available for inclusion in ADAS405. The result of this computation is plotted in Fig. 4.34. According to this model, the central region of RFX plasma is mainly populated by W^{+24} and W^{+25} ions, higher charge states are present in the core region in lower quantity, while ions from W^{+23} to lowest charge states are present in the external region.

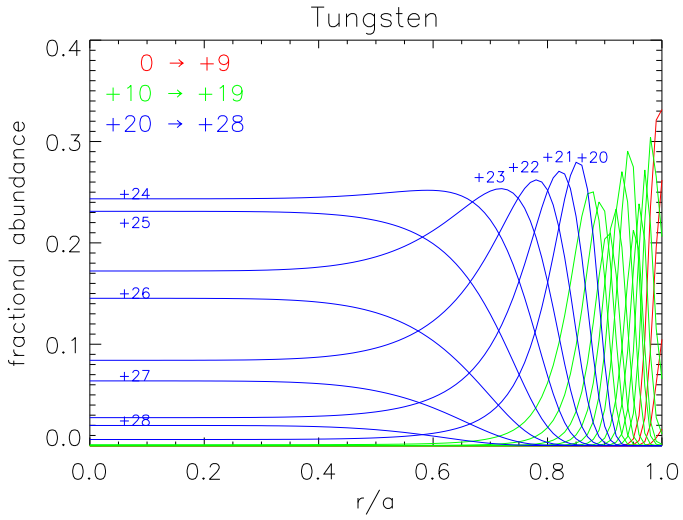

Figure 4.34: Ionisation equilibrium of tungsten without transport computed by ADAS405 for a typical RFX plasma with $T_e = 700$ eV and $n_e = 3 \times 10^{19}$m^{-3}. Charge-exchange processes not included in the calculation.

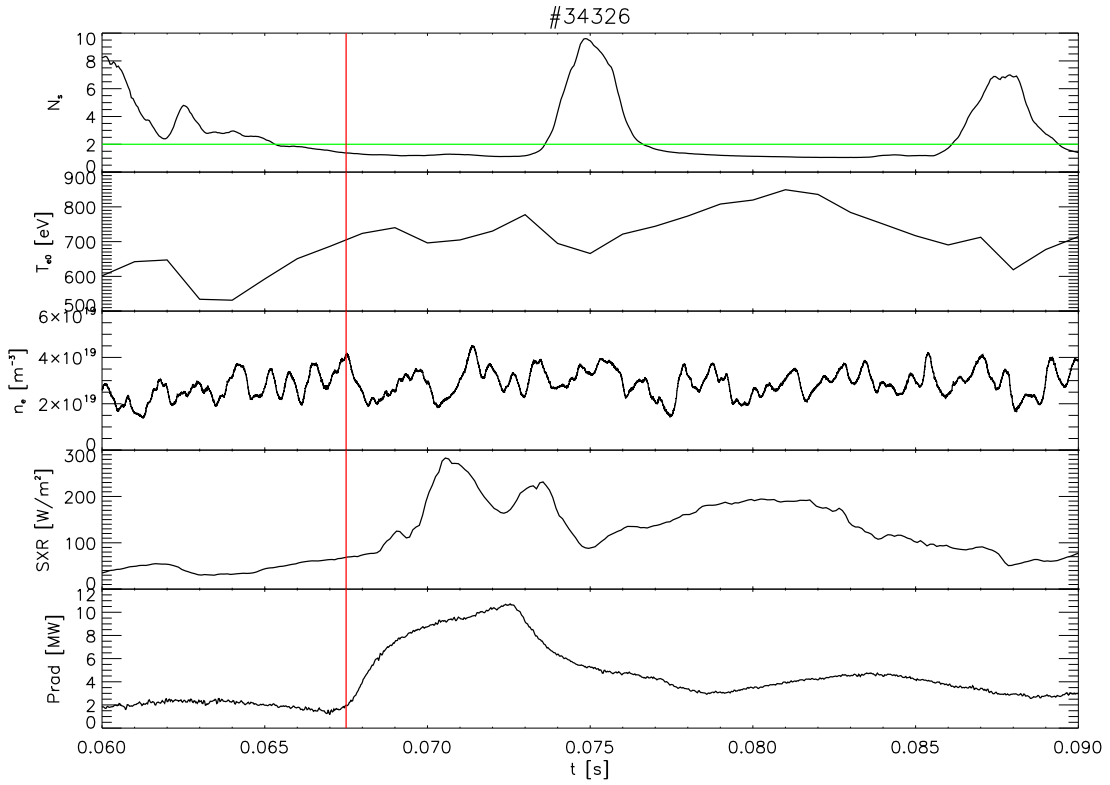

Figure 4.35: W LBO at 67.5 ms (vertical red line). [top to bottom] Magnetic spectral index with MH-QSH threshold in green. Central electron temperature. Line-averaged electron density. Central chord SXR brightness. Total radiated power.

4.6.3 Spectroscopic investigations

Once the injection is performed impurities are traced inside the plasma following their emissions: in particular vacuum ultra violet (VUV) and extreme ultra violet (XUV) spectral ranges are investigated by different spectrometers in order to identified W lines and regions of high radiative emissions.

Spectral lines at 1900-2000 Å

This spectral range is scanned by a Czerny-Turner spectrometer: equipped with a 1200 g/mm grating, it covers the wide range 1150-8000 Å, from the ultraviolet (UV) to the near infrared, with a resolution of 0.3 Å. In particular the instrument is optimised for observations in the VUV and UV regions [95, 96]. For the shots with W LBO the selected spectral range is 1875-2030 Å.

In this spectral region several W lines are observed as reported in Table 4.1. These lines are emitted by low ionisation stages of tungsten in the plasma periphery. Fig. 4.36 shows the spectrum acquired before and after the LBO with identified lines from tungsten and intrinsic impurities.

λ_{obs}	λ_{ref}	ion	transition	rel. int.
1900	1901.23	W IV	$5d^2(^3\mathrm{F})6s - 5d^2(^3\mathrm{F})6p$	900
1976.5	1976.70	W III	$5d^3(^4\mathrm{F})6s - 5d^3(^4\mathrm{F})6p$	800
1979	1978.77	W III	$5d^3(^2\mathrm{H})6s$	80
	1979.02	W IV	$5d^2(^3\mathrm{F})6s - 5d^2(^1\mathrm{D})6p$	100
1991.5	1991.78	W III	$5d^4 - 5d^3(^4\mathrm{F})6p$	800

Table 4.1: Identified W lines in the region 1875-2030 Å. Reference wavelengths, transitions and relative intensities are taken from NIST Atomic Spectra Database (http://physics.nist.gov/asd).

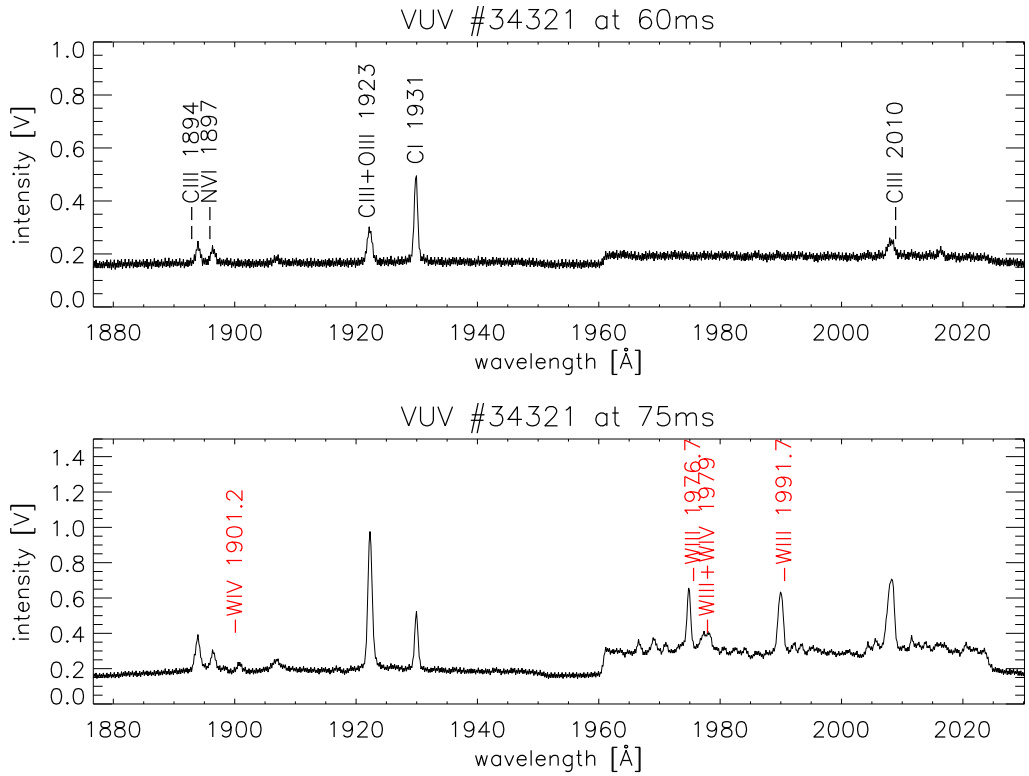

Figure 4.36: VUV spectrum before and after W laser-blow off showing the appearance of some W lines.

Quasi-continuum around 50 Å and 35 Å

XUV spectral range is scanned by a grazing incidence Schwob-Fraenkel duochromator, equipped with a 600 g/mm grating [87]. The instrument is provided with two multichannel detectors each of them scanning a different range of wavelengths simultaneously in the range 5-340 Å, with a measured resolution of about 0.2 Å.

In the spectral region selected for the first detector, 25 - 60 Å, tungsten exhibits two quasi-continuum structures, originated by a large number of energy levels with similar energies from different ions, resulting in an array of lines which overlap in the same wavelength region. These quasi-continuum bands are located around 35 and 50 Å; they are clearly visible in Figs 4.37 and

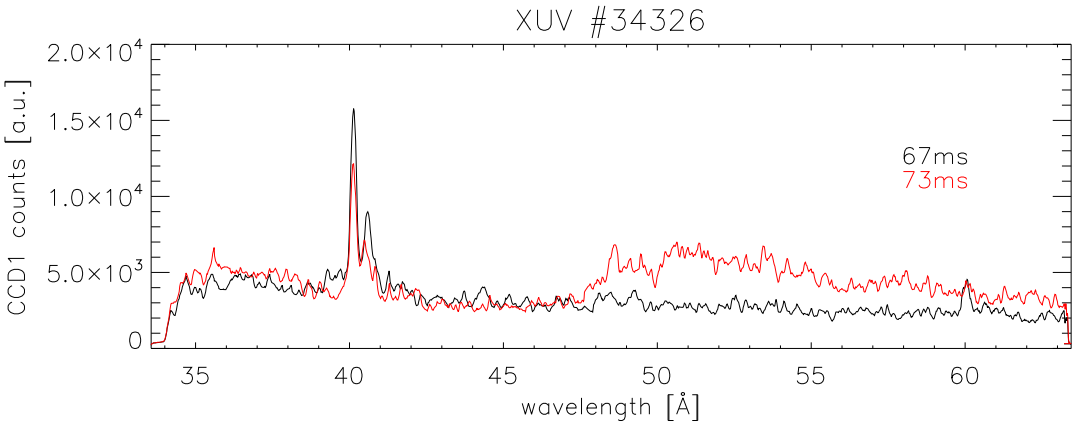

Figure 4.37: XUV spectra measured before and after W LBO (at 67.5 ms) showing the W quasi-continuum emission between 50 and 60 Å. Strong lines are emitted by intrinsic impurities: C V 40.27 Å and C V 40.73 Å.

4.38, showing measured spectra before and after W laser blow-off.

The quasi-continuum structures between 30 Å and 60 Å are common features of tungsten emission is fusion plasmas. They were already observed, for higher temperatures, at the ORMAK [97] and PLT [98] tokamaks in the 1970s, and more recently at the ASDEX Upgrade tokamak [99]. These bands are composed of a large number of spectral lines which arise from overlapping transition arrays originating from several successive states of ionisation of the atom. The lines arising from the $4d-4f$ type transitions fall into a rather narrow spectral range throughout the stripping of the 24 electrons in the $4f$ and $4d$ subshells. All tungsten ions from about W XVIII (ionisation potential $E_\mathrm{i} \approx 430$ eV) to W XLVI ($E_\mathrm{i} \approx 2.4$ keV) are expected to emit their strongest radiation between about 30-70 Å. In other words, this is the wavelength range where more than half of the total energy emitted by tungsten is expected to fall, in plasmas with electron temperatures roughly between $0.3 < T_\mathrm{e} < 2$ keV.

Measurements of the radiation of W ions in the range 21+ to 45+ were performed at the Berlin laboratory with an electron beam ion trap [100]. These experiments showed that for charge states lower than W^{+36}, the spectrum lines fuse into a bright emission band situated around 50 Å, with an extension of about 2 Å. This narrow band emission originates from ions that have either an open $4d$ subshell or a few electrons in the $4f$ subshell. When the beam energy becomes less than about 1 keV, the emission pattern disperses and shifts to higher wavelengths, forming a continuum structure ranging approximately between 50 and 60 Å. This is the structure visible in the RFX spectrum reported in Fig. 4.37, where the highest W ions responsible for this structure are those around W^{+25}. This band originates when ions with several $4f$ electrons in the ground-state configuration play an important role in the emission of tungsten.

RFX spectrum also exhibits a quasi-continuum structure at about 35 Å (Fig. 4.38). This feature had been observed at similar electron temperatures at the TEXT tokamak during W LBO experiments [101]. Their theoretical calculations for species from W^{+21} to W^{+25} showed that this band originates from $4d - 5p$ and $4f - 5g$ transitions, and that the ions involved are those with more than 3 electrons in the open $4f$ subshell.

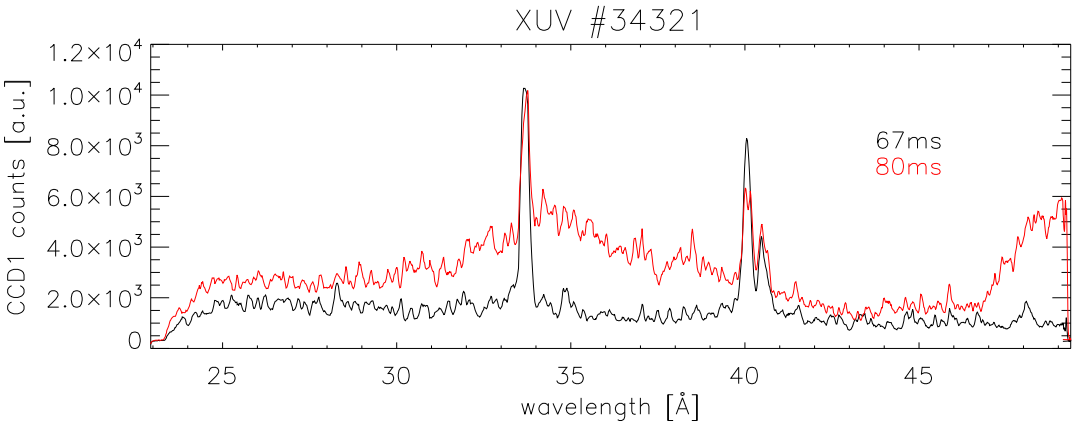

Figure 4.38: XUV spectra measured before and after W LBO (at 70 ms) showing the W quasi-continuum emission around 35 Å. Strong lines are emitted by intrinsic impurities: C VI 33.73 Å, C V 40.27 Å and C V 40.73 Å.

Quasi-continuum at 100-300 Å

This spectral range is scanned by a grazing incidence spectrometer, the Survey Poor Resolution Extended Domain spectrometer (SPRED): equipped with a 450 g/mm grating, it covers the range 20-1280 Å with a spectral resolution of 2 Å [102].

In the spectral range 100-300 Å tungsten exhibits a broad quasi-continuum structure, as reported in Fig. 4.39 showing different spectra before and after W LBO injection. The most intense spectrum leads to a saturation of the signal acquired by the detector.

A broad feature at those wavelengths was also observed at JET [103] and ASDEX Upgrade tokamaks [99]. In particular the latter experiment showed that this structure is emitted at temperatures below 1.3 keV, as those of the experiments done at RFX-mod. Modelled spectrum at ASDEX Upgrade revealed that the strong emissions around 180 Å originate from the ionisation stages W^{+26} to W^{+24}, while the emissions between 190 and 270 Å could be generated from W^{+23} to W^{+14}. The emissions between 100 and 300 Å contain contributions from the configurations $4f^3 5s, 4f^3 5p, 4f^3 5d$ and $4f^3 5f$ [99].

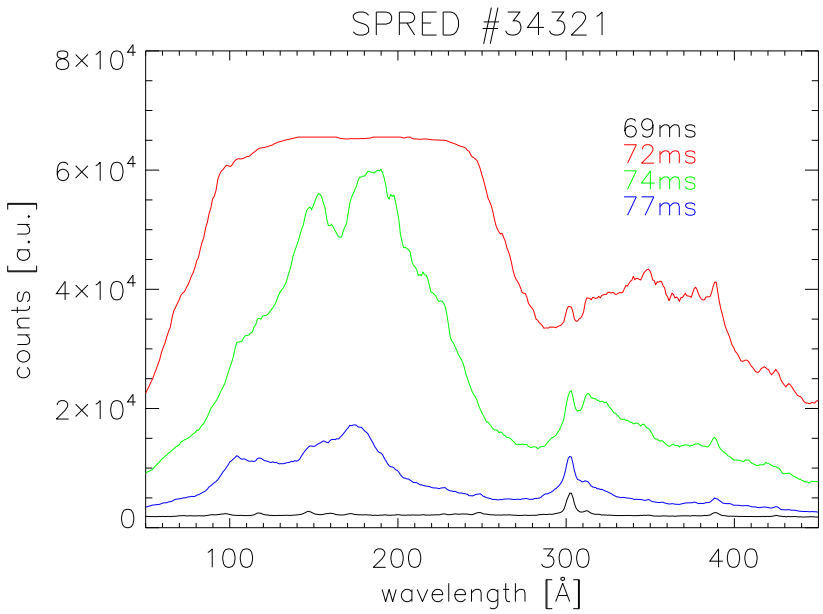

Figure 4.39: Measured emissions before and after W LBO (at 70 ms) featuring a quasi-continuum structure at 100-300 Å. A saturation of the measurements occurs soon after the injection. He II line at 303.8 Å and C IV line at 384 Å.

4.6.4 Total radiation investigations

Tungsten injection has been analysed by means of a tomographic reconstruction of the total radiated emissivity through the measurements of a bolometer. The bolometer array consists of 36 vertical lines-of-sight, arranged in three overlapping fans of 12 lines-of-sight each; the detectors are gold resistor bolometers covering the spectral region from 0.2 to $\simeq$ 500 nm, from visible to soft x-ray radiation [14].

The basic principle of radiative emission tomography is that of measuring the emitted radiation from a plasma poloidal cross-section along a large number of collimated lines of sight. A pinhole open in the head front plate defines the geometry of the lines-of-sight and allows radiation to impinge the detectors. The lines are uniquely identified by their impact parameter p (the distance of the line-of-sight from the centre of the plasma cross-section) and chord angle ϕ (the angle between the normal to the line-of-sight and the equatorial plane). If $\varepsilon(r,\theta)$ is the plasma *emissivity* at each point, then the power $P_{L(p,\phi)}$ impinging on the detector is proportional, through a geometrical factor k, to the line integral of the emissivity along the line-of-sight L

$$\frac{P_{L(p,\phi)}}{k} = f(p,\phi) \equiv \int_{L(p,\phi)} \varepsilon(r,\theta)\,\mathrm{d}l \tag{4.3}$$

where r and θ are the usual polar coordinates over the poloidal cross-section. The measured quantity $f(p,\phi)$ is the *brightness* [W $\cdot$ m^{-2}]. An interesting physical result is that in Eq. 4.3 the brightness is the same for all the chords with the same p and ϕ, i.e. the brightness does not depend on the length of the viewing chord.

Emissivity distributions [W $\cdot$ m^{-3}] can be obtained from the brightness measurements by means of the inversion of Eq. 4.3; this can be performed with a variety of techniques, which can be divided into three categories:

- **analytical methods:** they are based on the decomposition of the $\varepsilon(r,\theta)$ function into a finite number of basic functions; for the angular coordinate they are poloidal harmonics of the type $\sin m\theta, \cos m\theta$, while for the radial coordinate they are chosen among suitable functions (orthonormal polynomials, cylindrical Bessel functions, piecewise linear functions, etc.);
- **finite elements methods:** they are based on the direct discretisation of the $\varepsilon(r,\theta)$ function, assumed to be constant over plasma regions (*pixels*) of suitably chosen shape;
- **hybrid methods:** they combine features of the two previous methods; though the Fourier expansion is maintained, the emissivity radial behaviour is described dividing the plasma cross section in concentric pixels. The radial dependence of the emissivity in individual pixels is then approximated by continuous linear piecewise functions.

The algorithm used here to invert brightness measurements is a hybrid method: the detailed description is given in [85, 104].

The results of the tomographic reconstruction are shown in Fig. 4.40, where are plotted the measured brightness profiles, reconstructed emissivity profiles and distributions before and after W LBO.

For a standard discharge the total radiation emissivity profiles are peaked close to the wall; emission is strongly localised near the impurity source where low ionisation stages of carbon and oxygen radiate. This external radiative layer extends radially for a few centimetres.

Soon after the tungsten injection $P_{\rm rad}$ raises; the peaks in the emission profiles grow and move inwards. Contour plots show that radiation comes predominantly from an external radiative layer located at about $10 \div 15$ cm from the vacuum vessel and which extends for about 10 cm. This means that radiation is confined in an external region and does not come from the core plasma. There is no evidence of tungsten accumulation in the core, on the contrary this external radiative layer suggests that tungsten ions are kept in the external region and do not penetrate in the central plasma.

This impurity screening is similar to what had been found with nickel LBO and neon gas puffing experiments in QSH discharges, carried out in the past years at RFX-mod [55]. Fig. 4.41(a) reports the total radiation emissivity reconstruction for a Ni injection in QSH regime (LBO at 85 ms). Fig. 4.41(b) shows the reconstructed emissivity for a Ne puffing in QSH regime (Ne enters at 140 ms). We note that in both cases a radiative ring appears in the external region, like what has been observed during tungsten LBO shots. This ring is more external for Ne due to its lower atomic number: it radiates predominantly at low temperatures where there are low Ne charge states. For greater atomic number species (Ni and W), the radiative layer is more internal: ions of those species radiate more at higher temperatures. However the emitting layer is still far from the plasma core, implying that those ions are confined in the external region.

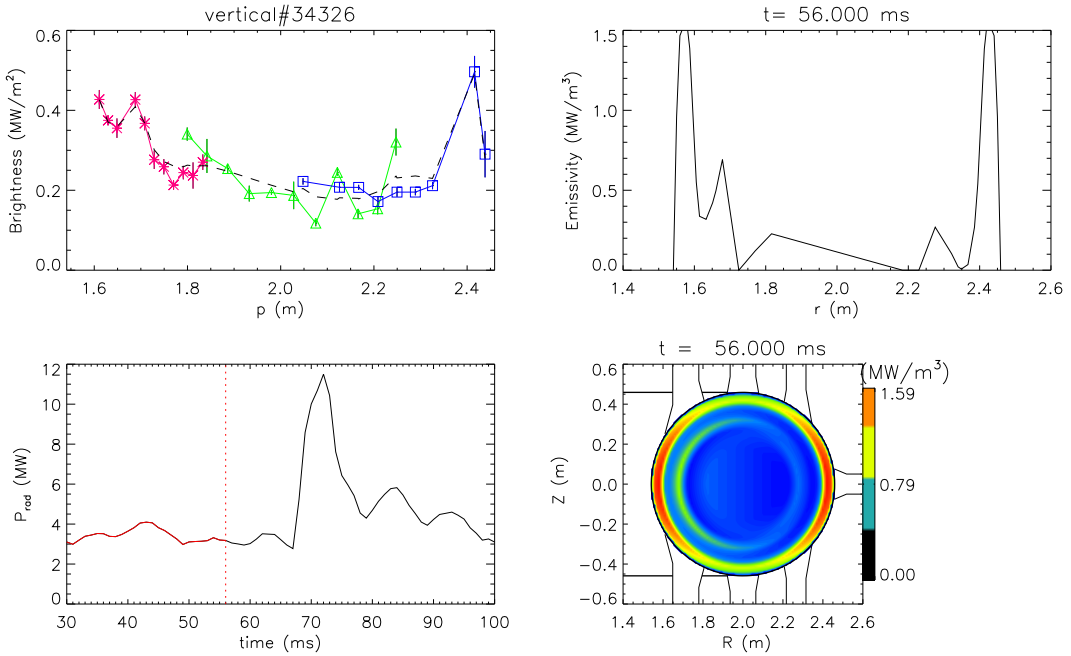

(a)

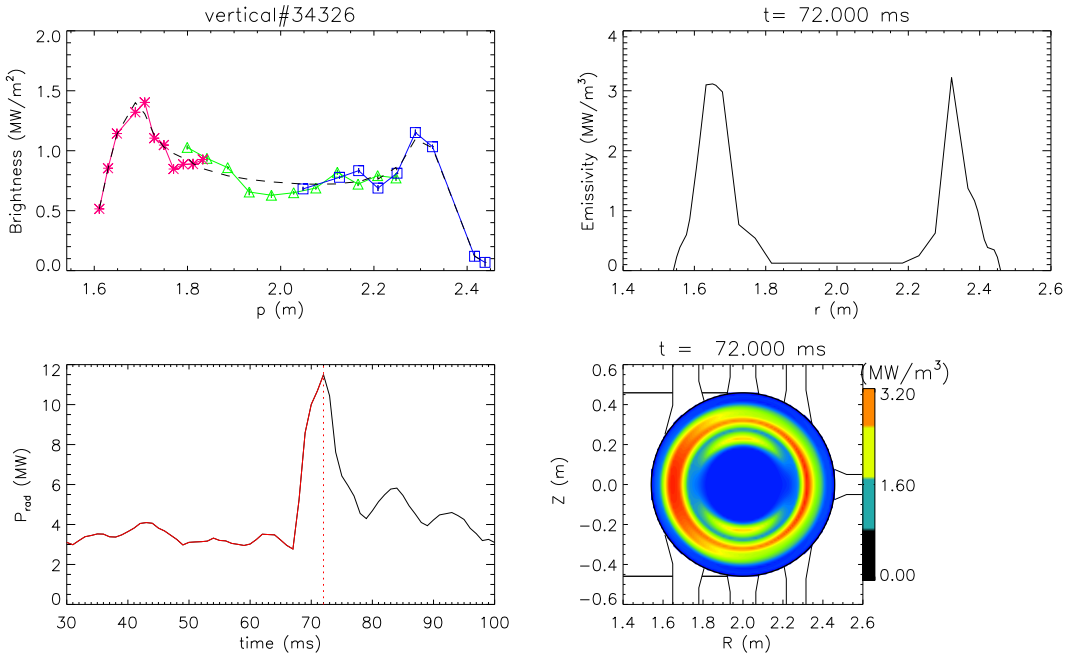

(b)

Figure 4.40: Bolometry analysis for a shot with W LBO at 67.5 ms. [From top left to bottom right] Experimental brightness profile. Reconstructed emissivity profile. Radiated power. Contour plot of the emissivity distribution.

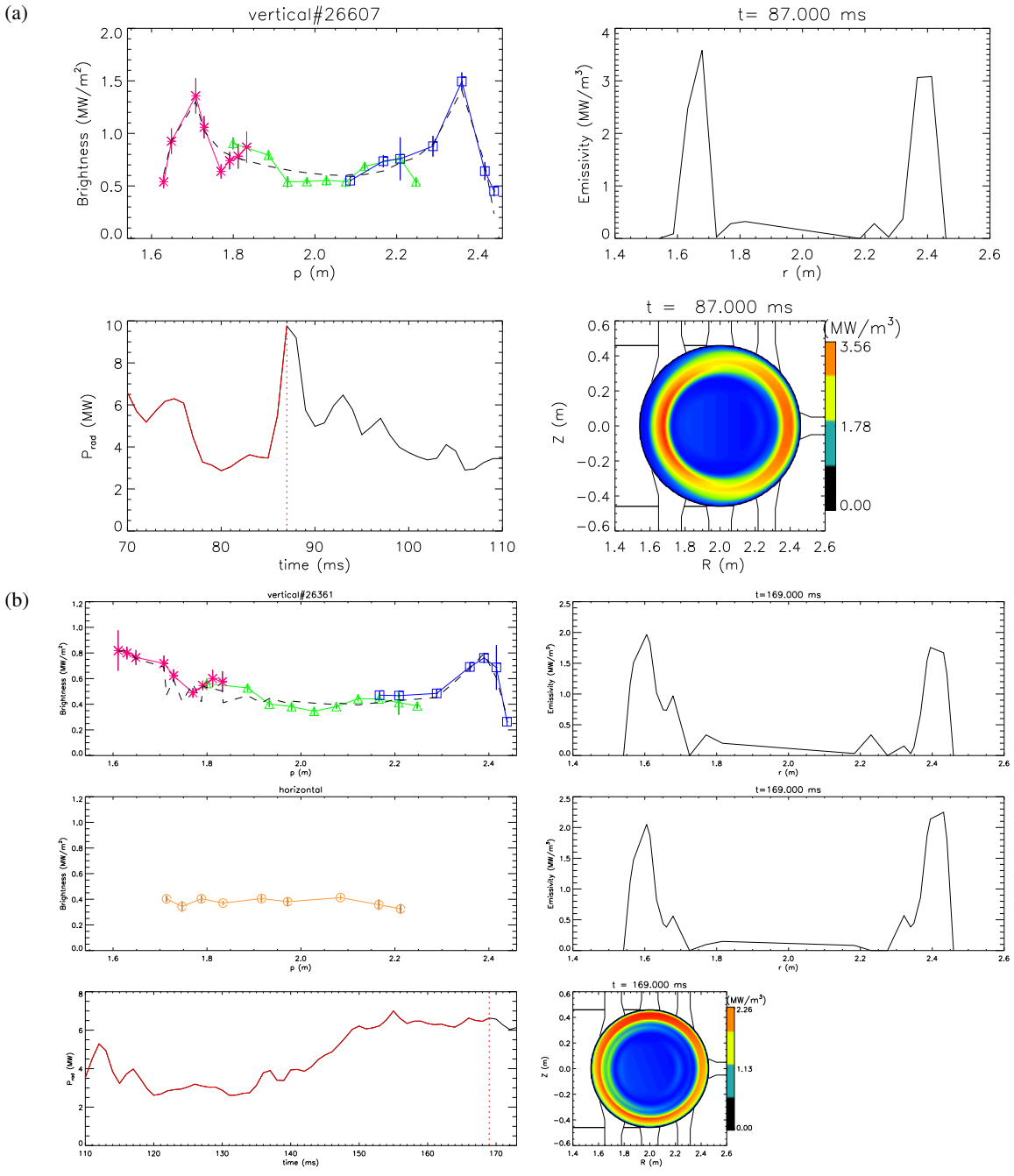

Figure 4.41: (a) Bolometry analysis for a shot with Ni LBO at 85 ms. [From top left to bottom right] Experimental brightness profile. Reconstructed emissivity profile. Radiated power. Contour plot of the emissivity distribution. (b) Bolometry analysis for a shot with Ne gas puffing at 140 ms. [From top left to bottom right] Vertical chords brightness measurements. Corresponding reconstructed emissivity profile. Horizontal chords brightness measurements. Corresponding reconstructed emissivity profile. Radiated power. Contour plot of the emissivity distribution.

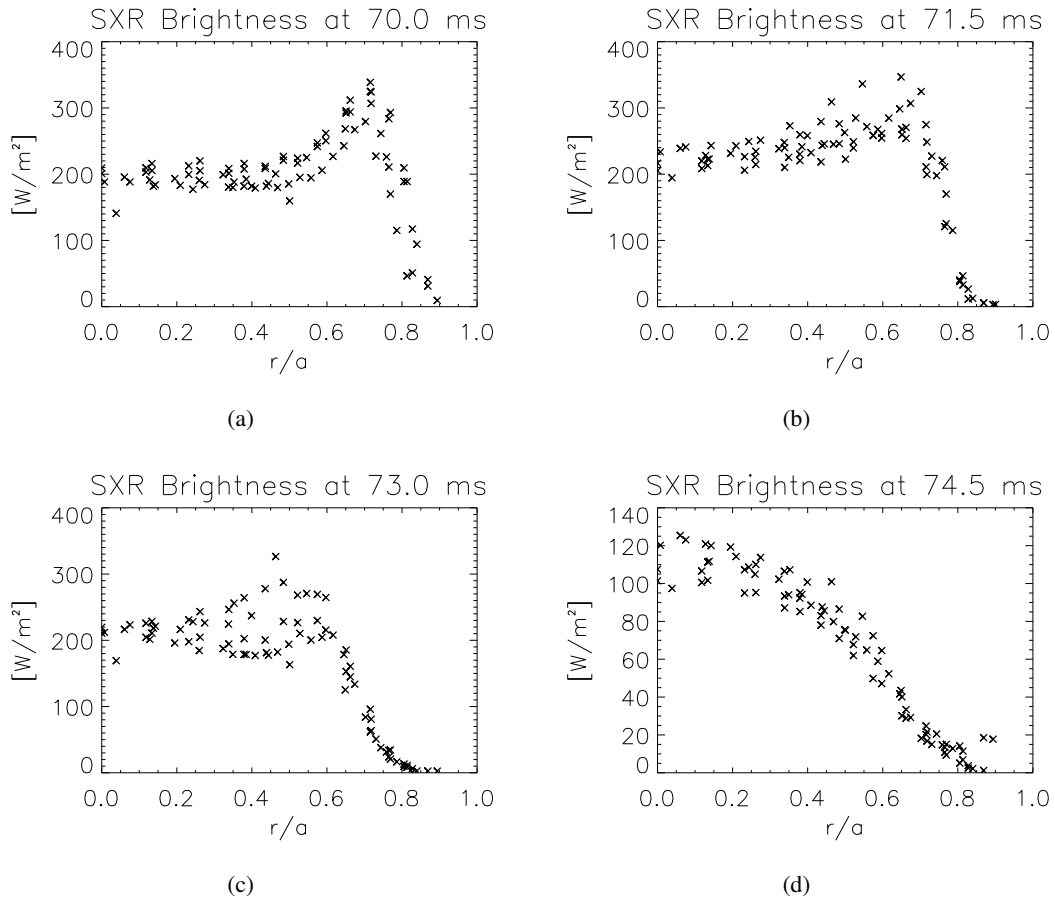

Figure 4.42: SXR brightness profiles at different times after W LBO (injection at 67.5 ms).

4.6.5 Soft X-rays investigations

Tungsten injection has been investigated also through the analysis of the SXR emissions. Measured brightnesses result in hollow profiles immediately following the LBO injection, as reported in Fig. 4.42. Subsequently, as tungsten does not progress to the plasma centre, the SXR profile returns to its previous centrally peaked shape after a few milliseconds. This is exactly what was observed with Ni LBO injection. Fig. 4.43 shows measured SXR brightnesses along with the simulated profiles for Ni experiments [55]. Nickel remained confined in the outer region leading to hollow SXR brightness profiles. The analogy with the present W experiments is evident.

This tendency is confirmed by 2D poloidal inversions of SXR brightnesses, performed through the same hybrid algorithm used for inverting total radiated brightnesses. Fig. 4.44(a) shows the reconstructed emissivity distribution following W injection: the SXR radiation comes predominantly from a narrow ring in the external region, in analogy with the peaked SXR brightness profiles; no core emission is observed. The same feature has been observed with the emissivity reconstruction after Ni LBO injection, reported in Fig. 4.44(b): a wider radiative ring appears soon after the injection. In the Ni case the SXR radiation is much stronger because it is dominated by K lines of nickel.

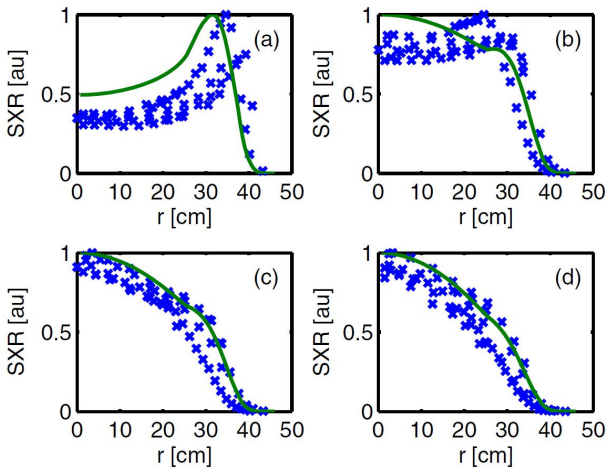

Figure 4.43: Normalised experimental SXR brightnesses (×) and simulated profiles (green lines) for different times after Ni LBO (injection at 85 ms): (a) 87 ms, (b) 91 ms, (c) 93 ms, (d) 95 ms. [55]

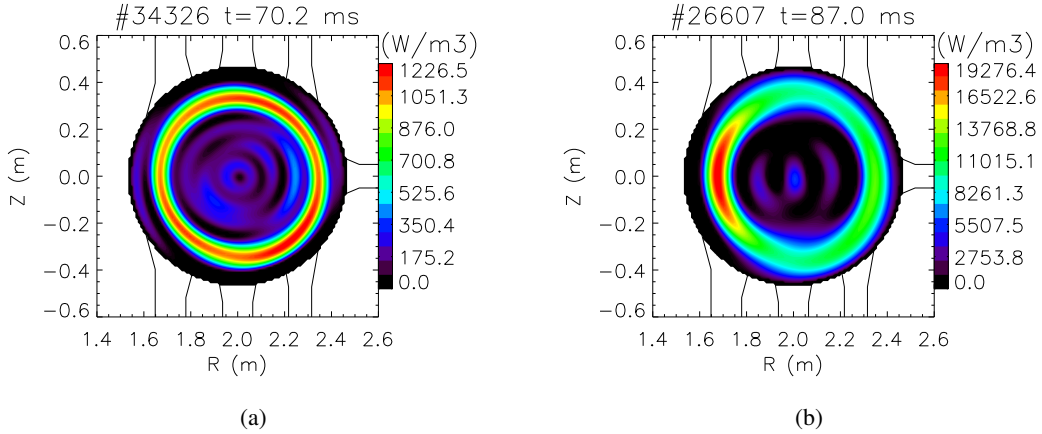

(a) (b)

Figure 4.44: Tomographic reconstruction of the SXR emissivity following (a) W LBO and (b) Ni LBO injection.

In conclusion tungsten experiments confirm that impurities are screened in RFX-mod especially during the QSH regime, regardless of the mass/atomic number. Simulations with CR codes for Ni and Ne showed that the screening was due to a velocity barrier located in the plasma external region (see Figs 4.5 and 4.6). Simulations of carbon and lithium pellet injections showed that the same velocity barrier well reproduces those experiments. Now we can say that, even if a W CR code is not available, this picture can be extended to tungsten, by supposing that the same velocity barrier acts also on W ions preventing them from penetrating towards the plasma core.

This is an appealing feature for a future W first wall in RFX-mod. Since W does not penetrate in the plasma core and it concentrates in a region where temperature is not very high, it radiates less than it would have radiated if it had accumulated in the core. This in turn avoids a strong cooling of the plasma.

4.7 Conclusions

In this chapter the analyses of impurity transport on RFX-mod through transient experiments have been presented. Solid pellet of carbon and lithium have been injected with a pellet injector. The injection causes a variation in the plasma density and radiative emissions (line, SXR and radiated power). This transient is reproduced by the 1D transport code, allowing to estimate the transport coefficients for the different species in different plasma regimes.

For carbon, transient experiments are carried out in both MH and QSH scenarios, confirming the transport coefficients previously determined for intrinsic impurities in a transientless simulation. They denote a region of outward convection in the outer radius, which is wider in the QSH regime. Diffusion coefficient is found lower in the core for QSH states, in agreement with the improved confinement in the core plasma.

For lithium, transient experiments are reproduced in MH conditions. The estimated transport coefficients are similar to those determined for carbon, with a stronger outward velocity near the edge.

For both species, the outward convection of impurities previously discovered with Ni and Ne experiments is confirmed for lighter elements, implying a common nature of transport independent on mass/atomic number.

Further experiments with tungsten laser blow-off are carried out in order to investigate W plasma core penetration capability, and explore W emission spectra. W spectral features are found similar to those observed in other devices at higher temperatures. Analysis of inverted SXR and total radiation measurements reveals that tungsten ions do not penetrate in the core plasma but remain confined in the external region, as it happens for lighter impurities.

Chapter 5

Impurity transport analysis on MST

This chapter presents the analysis performed on MST about the transport of the main impurity species in different regimes of operation. The impurity transport code has been employed in order to estimate the transport coefficients.

5.1 Madison symmetric torus experiment

MST experiment is a large reversed-field pinch located in Madison, Wisconsin, USA. Its main parameters are listed in the following table.

Major radius	1.5 m
Minor radius	0.52 m
Toroidal magnetic field	≤ 0.4 T
Plasma current	< 600 kA
Electron density	$\sim 10^{19}$ m^{-3}
Discharge duration	< 0.1 s

Figure 5.1: The MST experiment.

Figure 5.2: MST's inner wall.

The MST vacuum vessel is aluminium, with a thickness of 5 cm. Partially covering the inner surface of the vessel are tiles and limiters which interact with the plasma during the discharge and become a source of impurities. The identified dominant impurities in MST plasmas are carbon, oxygen, boron, nitrogen and aluminium [105]. Carbon comes from the graphite tiles that line the vacuum vessel. Boron from the boron nitride probes and RF antennas that routinely get inserted into MST and from boronisation. Nitrogen from the boron nitride probes. Oxygen from the adsorption of H_2O vapour when MST is brought up to air. Aluminium from the vacuum vessel. The charge state distribution of these impurities in the plasma depends mainly on the electron temperature (ionisation) and the hydrogen neutral density (charge-exchange loss), which are significantly different in various plasma regimes in MST.

The typical safety factor (q) profile from a MST standard plasma is shown in Fig. 5.3(a). Major rational values are marked. The q profile accommodates a large number of rational flux surfaces where tearing modes grow. The dominant instabilities in the plasma core have poloidal mode number m=1. These modes are driven primarily by a gradient in the radial profile of the plasma current. These multiple coupled tearing modes result in quasi-periodic sawtooth (global magnetic reconnection) events as shown in Fig. 5.3(b). Magnetic field lines have a high degree of stochasticity both during and between these events. Transport is therefore predominantly stochastic. The global thermal diffusivity (χ_E) and energy confinement time (τ_E) are $\chi_E \sim 60\ m^2/s$ and $\tau_E \sim 1$ ms [106].

One reliable means of reducing these instabilities and improving energy confinement is modification of the current profile via auxiliary inductive current drive. Tearing mode suppression and an associated confinement improvement are achieved in MST during the enhanced confinement regime using "Pulse Poloidal Current Drive" (PPCD), an inductive control technique which reduces the free energy in the current profile that drives tearing instabilities. PPCD drives a poloidal current at the edge of the plasma by pulsing the toroidal magnetic field. The main characteristic of PPCD discharge are low level of magnetic fluctuations, higher core electron temperature (see Fig. 5.4), and improved energy confinement [52]. The estimated energy confinement time ($\tau_E \sim 12$ ms) is increased more than tenfold compared to standard discharges, and the corresponding global thermal diffusivity drops to $\chi_E \sim 5\ m^2/s$.

Electron particle confinement time is increased by a factor of 8, similar to the gains in energy

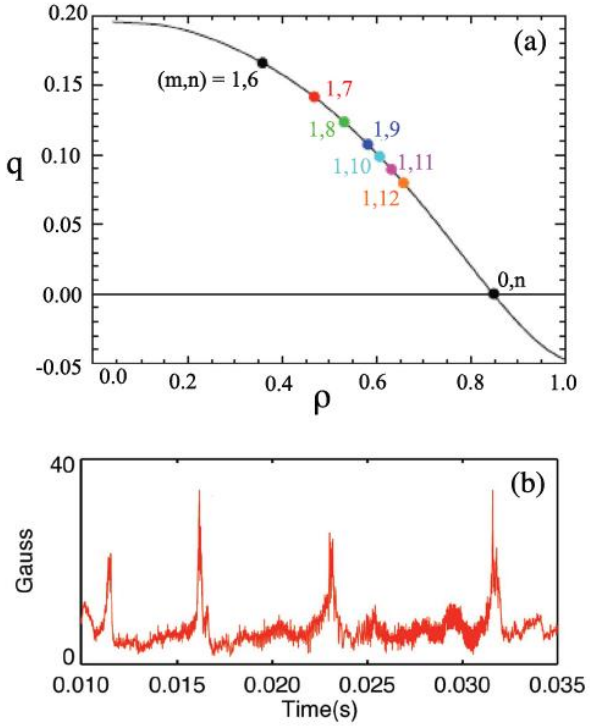

Figure 5.3: (a) Typical safety factor profile for standard RFP discharge. Major rational values are marked. (b) Mean amplitude of core-resonant magnetic fluctuations (m = 1, n = 7-12 modes) in a standard RFP discharge exhibiting quasi-periodic sawtooth activity. [56]

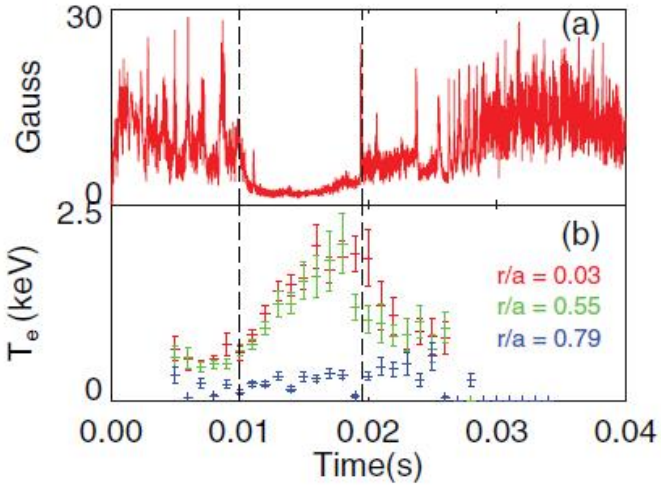

Figure 5.4: (a) Mean amplitude of core-resonant tearing modes in PPCD discharge (m = 1, n = 7-12 modes). The region between dotted lines represent the improved confinement regime. (b) Electron temperature measured using a Thomson scattering diagnostic at three radial locations. [56]

confinement: from $\sim$ 0.6 ms in standard plasma to $\sim$ 4.7 ms during PPCD [107]. Experiments with injection of frozen deuterium pellet found a value of the particle confinement time $<$ 6 ms [108], compatible with the previous value in lower density improved confinement plasmas.

In standard plasmas, the ions are heated via collisions with electrons and, during global reconnection events, via an additional anomalous mechanism linked to dynamo activity [109]. During PPCD, unlike for T_e, the ion temperature does not change significantly with fluctuation reduction. This may reflect an improvement in ion energy confinement, since at least one source of ion energy is expected to drop with improved confinement. With PPCD, dynamo becomes much smaller and this heat input is expected to drop. Hence ions may be only collisionally heated during PPCD. Moreover since stochastic transport is expected to scale with the thermal velocity $\chi^{st} \propto v_{\|T}$, the expected ion $\chi_i^{st} = (m_e T_i / m_i T_e)^{1/2} \chi_e^{st}$. The upper bound for χ_e^{st} during PPCD is the power-balance measured χ_e, which implies very small $\chi_i^{st} \lesssim 0.1\ m^2 s^{-1} \sim \nu_{ie} \rho_i^2$ [106]. The expected stochastic magnetic transport for ions during PPCD is therefore reduced to the classical transport level.

Impurity transport in these two regimes of operation is expected to be very different. In standard plasmas transport is strongly linked with stochasticity and magnetic fluctuations. We expect an intense perpendicular flux of impurities especially during reconnection events. In PPCD plasmas magnetic fluctuation are reduced and particle confinement time increases revealing that the radial electron flux is significantly reduced over the entire cross section. We expect that also the impurity flux will be reduced over the radius and the transport will come closer to classical value.

5.2 MST impurity analysis

5.2.1 Charge-exchange recombination spectroscopy

In the past years impurity density measurements were made in MST during both standard and PPCD discharge by means of Charge-Exchange Recombination Spectroscopy (CHERS) [61][105]. A beam of neutral hydrogen atoms is injected radially into the plasma, and these atoms exchange their charge with the impurity ions in the plasma. The impurity ions are left in an excited lower charge state which then radiatively decays. Below is shown the scheme of this process for carbon.

$$C^{+6} + H \rightarrow C^{+5*} + H^{+}$$
$$C^{+5*} \rightarrow C^{+5} \rightsquigarrow$$

The charge-exchange process preserves the energy; the Doppler shift and Doppler broadening of this deexcitation emission are used to calculate flow velocity and temperature of the initial-charge-state impurity ion population.

Although the C VI emission from charge exchange with the beam is strong, the background signal from the plasma is of the same order or larger in most circumstances. High background neutral density in MST results in substantial charge exchange of C^{+6} with thermal neutrals in the plasma; the C^{+5} ions thus created are excited by electron impact, and decay producing substantial background emission at the C VI transition of interest. Below is the scheme for this process.

$$C^{+5} + e \rightarrow C^{+5*} \rightsquigarrow + e$$

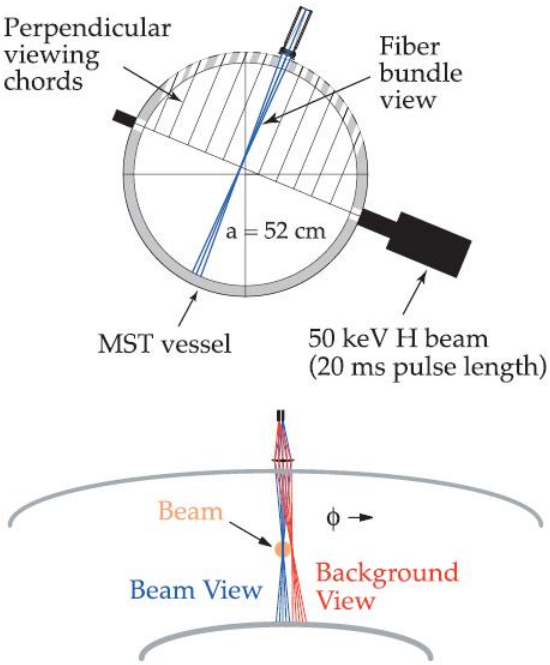

Figure 5.5: [Top] Poloidal cross section of MST showing diagnostic neutral beam path and CHERS perpendicular viewing chords. [Bottom] Radial view along the diagnostic neutral beam path showing toroidal displacement of the on-beam and off-beam views. [56]

In order to distinguish between beam-induced and background emissions, two signals are differenced from two lines-of-sight on poloidal planes that are toroidally separated by ~ 4 cm (see Fig. 5.5), to measure simultaneously both on-beam and off-beam (background) emission.

The charge-exchange and the electron-impact excitation/deexcitation emissions are modelled accurately using fine structure in corresponding atomic transitions, obtained from ADAS, to extract Doppler broadened emission parameters. The model is necessary for the accurate estimation of the ion temperature when the wavelength span of the fine structure manifold is comparable to or more than the Doppler broadening.

Local impurity density (n_z) is calculated from the emission brightness using the relation $B_{cx} = (1/4\pi) n_z \langle \sigma v \rangle \int n_b dl$, where B_{cx} (photons/m^{2}s Sr) is the charge-exchange emission brightness (the difference in the area under on-beam and background spectral curves), $\langle \sigma v \rangle$ is the effective emission rate and $\int n_b dl$ is the beam particle density n_b (m^{-3}) integrated over the spectrometer line-of-sight. Effective emission rates are obtained from ADAS. Beam attenuation is modelled using relevant beam stopping reaction cross sections for the three beam-energy components (full, half and one-third energy components are present in the beam with the ratio E : E/2 : E/3 $\sim$ 60 : 36 : 4%), verified with beam-emission and shine-through detector measurements. A 10% uncertainty is estimated in the impurity density, mainly due to uncertainties in the beam attenuation calculations and transmission efficiencies of the viewing lenses.

On MST, the CHERS diagnostic has 11 poloidal viewing chords (Fig. 5.5) sampling emission along the diagnostic neutral beam (nominal parameters: 45-50 keV, 4-5 A, 20 ms pulse length). Since only one high-throughput CHERS spectrometer has been built for use on MST,

measurements are made at one radial location, for one impurity species, per discharge. However, due to high reproducibility, compilation of profiles from various similar discharges in MST is possible. Distinct features of CHERS are good spatial (~ 1 cm) and temporal (up to 10 μs) resolution [110].

These experiments were conducted in deuterium discharges with toroidal plasma current ~ 400-550 kA, line-averaged central electron density n_e ~ 0.8-1 × 10^{19} m^{-3} and central electron temperature ranging from 300 eV (in standard discharges) to above 1.5 keV (in improved confinement discharges). Measurements were made for C^{+6} (n = 7-6 transition, 343.4 nm), B^{+5} (n = 6-5 transition, 298.1 nm), O^{+8} (n = 8-7 transition, 297.6 nm), Al^{+11} (n = 10-9 transition, 321.05 nm) and Al^{+13} (n = 11-10 transition, 310.65 nm). Carbon measurements were carried out both in standard and PPCD discharge, whereas boron and other higher-Z impurities were measured only during high current PPCD discharge (higher core electron temperature) in order to access higher charge states.

5.2.2 Impurity monochromator array

Impurities are also monitored by the Impurity Monochromator Array (IMA). It is composed of 5 monochromators each tuned to a specific emission line which is wanted to be monitored. The IMA measures the following impurity lines:

Impurity (Wavelength)	Location
C III (229.69 nm)	Extreme Edge ($\rho > 0.85$)
C V (227.09 nm)	Core ($\rho < 0.7$)
B IV (282.17 nm)	Mid to Edge ($\rho \sim 0.6$ to 0.9)
O IV (338.55 nm)	Extreme Edge
N IV (347.87 nm)	Extreme Edge

Fig. 5.6(a) shows the behaviour of the impurities for a standard discharge at medium current (400 kA). As the plasma gets started, the electron temperature is low and we can see that the plasma is composed mainly of low charge states. As the discharge evolves, low charge states burn through quickly and assume extremely hollow profiles. Hollow profile tend to produce lower chord-averaged signals, hence the observed intensity decreases. Higher charge states become dominant. Sawtooth events occur throughout the discharge leading to an increase in the impurity influx from the wall and a consequent increase in the low charge states signals.

Fig. 5.6(b) shows the behaviour of the impurities for a medium current PPCD discharge. C III, O IV and N IV exhibit typical edge element (lower charge state) behaviour as they spike up initially, hollow out and then ramp up at the end when the plasma cools down. The B IV and C V traces display typical mid to core element (higher charge state) behaviour. One can observe that they spike later in the shot than the lower charge states, taper off, ramp up again this time before the low charge state and then die down.

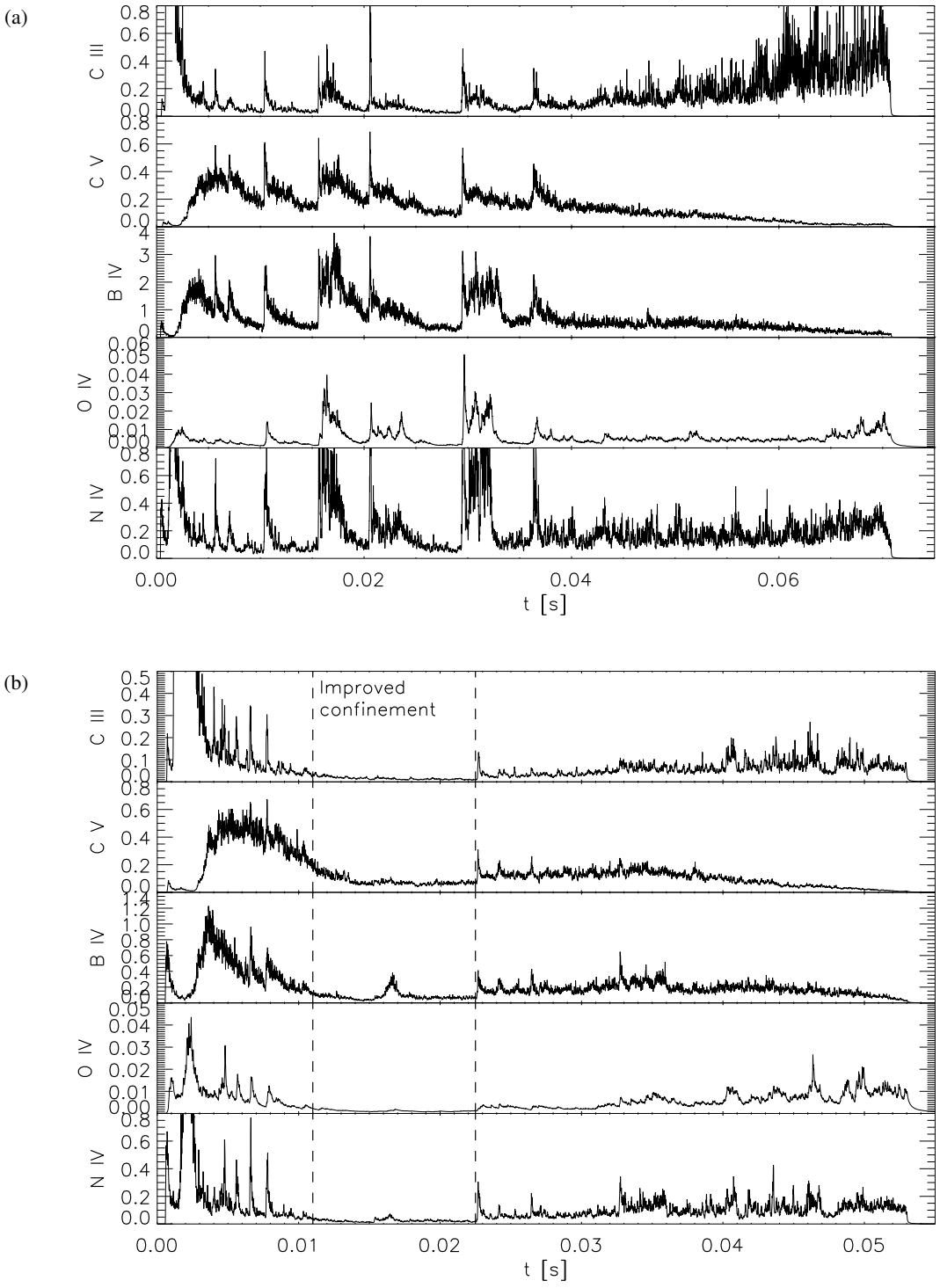

Figure 5.6: Line intensities for several impurities measured by the Impurity Monochromator Array during (a) standard discharge and (b) PPCD discharge. Intensities are expressed in a.u.

5.2.3 Impurity collisional-radiative and transport code

For characterising the impurity behaviour in MST, the 1-D collisional-radiative transport code, described in Chapter 3, is used for the different species, namely boron, carbon and oxygen. Aluminium code is not available, since the CR codes were written for intrinsic or injected species in RFX-mod where Al is absent. The codes are run in order to reproduce the density profiles and, when available, the time evolution of the impurities content in the plasma. The transport coefficients (D and v) enter the code as inputs and they are estimated by comparing the result of the simulation with the experimental data: the coefficients are varied until a match is achieved within the experimental uncertainties.

The measurements of the impurity density profiles on MST were averaged over a time interval of some milliseconds and over similar discharges. In standard discharges C^{+6} density measurements were carried out away from sawtooth events, where a steady-state condition of the plasma can be assumed; they represent equilibrium profiles. In these conditions transport coefficients are estimated by matching the measured density profile with the steady-state profile achieved in the simulation. In this steady-state situation usually only the ratio v/D (peaking factor) can be properly determined. However, as it will be detailed in Section 5.3.2, even in this situation an estimate of the two coefficients separately can be obtained.

In PPCD conditions the time variation of the radial impurity content was measured. The impurity influxes and the profiles of T_e and n_e are also evolving throughout the PPCD period. These time evolutions are taken into account in the simulation. In these conditions by matching the temporal evolution of the impurity content in three radial locations during the PPCD period, along with a full density profile measured at the end of that period, an separate estimate of D and v can be obtained.

Code inputs

Here are listed the main inputs to the code. Central electron density, $n_\mathrm{e}(r = 0, t)$, comes from the central line-averaged density measured by the CO_2 interferometer [111]. Central electron temperature, $T_\mathrm{e}(r = 0, t)$, is measured by Thomson scattering diagnostic (central chord) [112]. Electron temperature profile, $T_\mathrm{e}(r)$, is assumed on the basis of the multi-chord Thomson scattering measurements. During the PPCD these measurements are good enough to be directly used as inputs, while during standard discharge the TS data are often not very reliable and assumptions are needed. In this case the profile is fixed in shape and the time evolution is done on the central value (see Eq. (3.5)). The temperature at the edge ($\rho > 0.9$) is measured with a Langmuir probe [52]. Electron density profile, $n_\mathrm{e}(r)$, is assumed on the basis of FIR interferometry measurements [113]. The FIR system measures the line-averaged density along 11 chords, and with inversion, yields the full density profile. In the code the profile is fixed in shape and the time evolution is done on the central value (see Eq. (3.6)).

Neutral density profile is calculated using the Monte Carlo neutral particle tracing code NENÈ [49], properly scaled to the measured D_α emission from the edge of the plasma.

Impurity neutral influxes are estimated through comparing the time evolution of strong lines from low ionisation stages measured by the Impurity Monochromator Array (IMA) with the chord integrated line intensities simulated by the code. As the spectrometer is not absolutely calibrated only the influx temporal trend can be used.

Main gas ion temperature is a further input: its profile is measured at MST by Rutherford

scattering of helium neutrals injected by a diagnostic neutral beam [110]. In the code it is simply inserted multiplying the electron temperature by a constant factor taking into account the ratio between $T_e(0)$ and $T_i(0)$ but assuming the same profile.

Transport coefficients estimation

Given the limited number of experimental points, D and v profiles are estimated among a restrictive class of simple functions: linear between two consecutive spatial nodes (two and three nodes are used for D and v respectively).

The simulation is started with $D(r)$ set to constant values for the inner and the outer regions, connected through a step function. $D(r)$ is then adjusted, by modifying the two constant values and shifting the position of the transition. $v(r)$ is simply set in the form $v(r) = (r/a)v_a$, then the profile is adjusted by adding radial transition points in which $v(r)$ can be set positive (outward convection) or negative (inward convection). The profiles are adjusted in order to minimise the difference between the simulated and experimental fully stripped ion population with respect to the position and magnitude of the nodes.

In order to find the best magnitude of the coefficients, once the good position of the nodes is found, the minimum chi-square method is applied for both the core and edge region of the profiles. χ^2 is normalised to the number of experimental points. This is the application of the least squares procedure for the estimation of nonlinear parameters. In this situation may be useful to draw confidence ellipses in order to evaluate the correlation between those parameters.

Confidence ellipses

From the theory of the least squares estimation of nonlinear parameters [114], let the model to be fitted to the data be

$$\begin{aligned} E(y) &= f(x_1, x_2, \cdots, x_m; \beta_1, \beta_2, \cdots, \beta_k) \\ &= f(\mathbf{x}, \beta) \end{aligned} \tag{5.1}$$

where $x_1, x_2, \cdots, x_m$ are independent variables, $\beta_1, \beta_2, \cdots, \beta_k$ are the population values of k parameters, and $E(y)$ is the expected value of the dependent variable y. Let the data points be denoted by

$$(Y_i, X_{1i}, X_{2i}, \cdots, X_{mi}), \qquad i = 1, 2, \cdots, n \tag{5.2}$$

The problem is to compute those estimates of the parameters which will minimise

$$\begin{aligned} \Phi &= \sum_{i=1}^{n} [Y_i - \hat{Y}_i]^2 \\ &= \| \mathbf{Y} - \hat{\mathbf{Y}} \|^2 \end{aligned} \tag{5.3}$$

where $\hat{Y}_i$ is the value of y predicted by Eq. (5.1) at the ith data point.

When f is linear in the βs, the contours of constant Φ are ellipsoids, while if f is nonlinear, the contours are distorted, according to the severity of the nonlinearity. Even with nonlinear models, however, the contours are nearly elliptical in the immediate vicinity of the minimum of Φ. Typically the contour surface of Φ is greatly attenuated in some directions and elongated in others so that the minimum lies at the bottom of a long curving trough.

In our case the f function represents the transport model and the βs would be the transport coefficients. So if we plot χ^2 (or Φ) as a function of D and v in the core and edge regions we can have information about the linearity of the model with respect to its parameters. The result will be a series of concentric contours connecting all the points with equal value of χ^2. The smallest contour represents the region of the minimum χ^2. In case of linearity of the model in D and v these contours will be ellipses, while in case of nonlinearity the contours will be figures with distorted shapes. Moreover, if positive correlation exists between D and v, the major axis of the contours will have positive slope, while the slope will be negative in case of negative correlation. If no correlation exists the figures will be aligned with the coordinate axis.

From this analysis an estimate of the uncertainties of the D and v profiles can be obtained. Those profiles will correspond to the minimum χ^2 and their uncertainty will be the area around the smallest contour.

5.3 Standard discharge

Standard discharges are characterized by a sequence of quasi-periodic sawtooth events for all the discharge duration. The growth of magnetic fluctuations increases transport and consequently increased particle transport at the crash induces plasma-wall interaction (e.g., sputtering), leading to injection of impurities into the plasma [115]. This is evident looking at the low charge state impurities in Fig. 5.6(a): an increase in the impurity influx corresponds to an increase in the measured line intensity.

5.3.1 CHERS C^{+6} measurements

Fully stripped carbon measurements were made during standard discharges at and away the sawtooth crashes [61]. Radial and temporal profiles of C^{+6} density are shown in Fig. 5.7(a) and 5.7(b), respectively. Data are averaged over a large number of sawtooth events. Profiles away ($\sim$ 1.5 ms before) from the sawtooth event represent equilibrium profiles. The C^{+6} density has a flat/weakly hollow profile both at and away from the event. There is a global increase in the C^{+6} density at sawtooth events. The 'burst' of impurity density at a sawtooth event is more apparent from the sawtooth averaged temporal evolution shown in Fig. 5.7(b). The chord at $\rho \sim 0.75$, where ρ is the radial distance from the magnetic axis normalised to the plasma minor radius, shows the maximum increase, which is consistent with the fact that sawtooth activity leads to the liberation of impurities from the wall. Nevertheless the same figure reveals that impurities injected at a sawtooth event are expelled before the subsequent event. The resultant impurity density profile is then flat. This may not be a surprising result considering that stochasticity leads to mixing of different plasma regions.

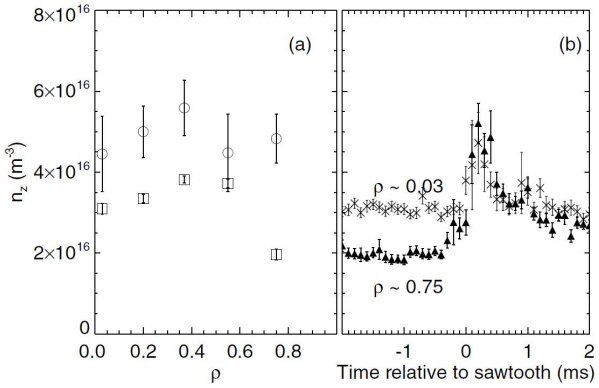

Figure 5.7: C^{+6} density for standard discharge measured by CHERS: (a) radial profiles away from (□) and at (○) sawtooth events. (b) Sawtooth averaged temporal evolution at $\rho \sim 0.03$ and $\rho \sim 0.75$. Error-bars show standard deviation of the mean from ensembles. [61]

5.3.2 Carbon transport analysis

Transport code for carbon is used to characterise carbon transport in standard discharge. The code cannot reproduce the complex impurity dynamics which is involved in the sawtooth event, that is the sudden increase in the neutral influx from the wall and following expulsion of impurities. Hence for the simulation the discharge is considered as it were free of sawteeth, the only sign of their presence are the periodic crashes in $T_e(0)$ (Fig. 5.9(a)). The simulation therefore will attempt to reproduce the carbon profile measured away from the sawtooth event, which represents a steady-state profile.

The chosen shot to be reproduced is #1110510075. In Fig. 5.9 are shown the inputs to the code. The first part of the central electron temperature time evolution, where there are not data from Thomson scattering, is assumed starting from an initial value set to 100 eV and then reaching the first TS measurement with a time evolution similar to that of the plasma current ramp. The evaluation of the first value of the electron temperature is made without any experimental evidence. However, even if it were not correct, this would not influence the simulation since the temperature grows up immediately. Neutral density profile has been reconstructed through NENÈ code for standard discharge away from sawteeth (Fig. 5.10(a)).

The steady-state C^{+6} density profile is simulated and is compared with the corresponding CHERS measurements with the best fit D and v (Fig. 5.10(b)). However, even modifying the profiles of the transport coefficients, the simulated carbon population is always underestimated with respect the measurements in the outer region, as it is clear looking at Fig. 5.10(b). The reason of this discrepancy is believed to lie in the incorrect estimation of the neutrals through the NENÈ code. In fact it is thought that the amount of neutrals present in the edge region is overestimated, as a consequence the neutral particles in the simulation charge exchange with the C^{+6} ions and simulated C^{+6} is lower than experimental C^{+6} in the external region.

The estimation of the neutral density profile by NENÈ may suffers from great inaccuracy. The line-integrated D_α measurements are hard to interpret when the core neutral density is several orders of magnitude lower than the edge, and in MST there are not measurements all the way out to the edge. Moreover, that method only accounts for atoms (not D_2 molecules) and NENÈ does not model gas puffing or wall recycling exactly how it occurs on MST. Therefore,

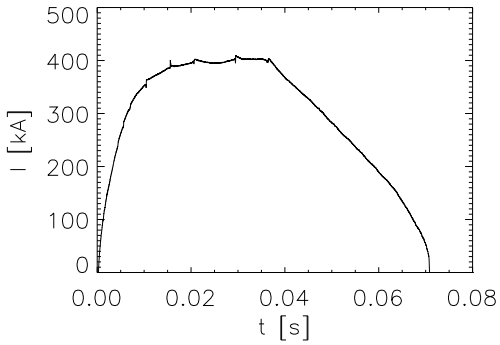

Figure 5.8: Plasma current for a 400 kA standard discharge.

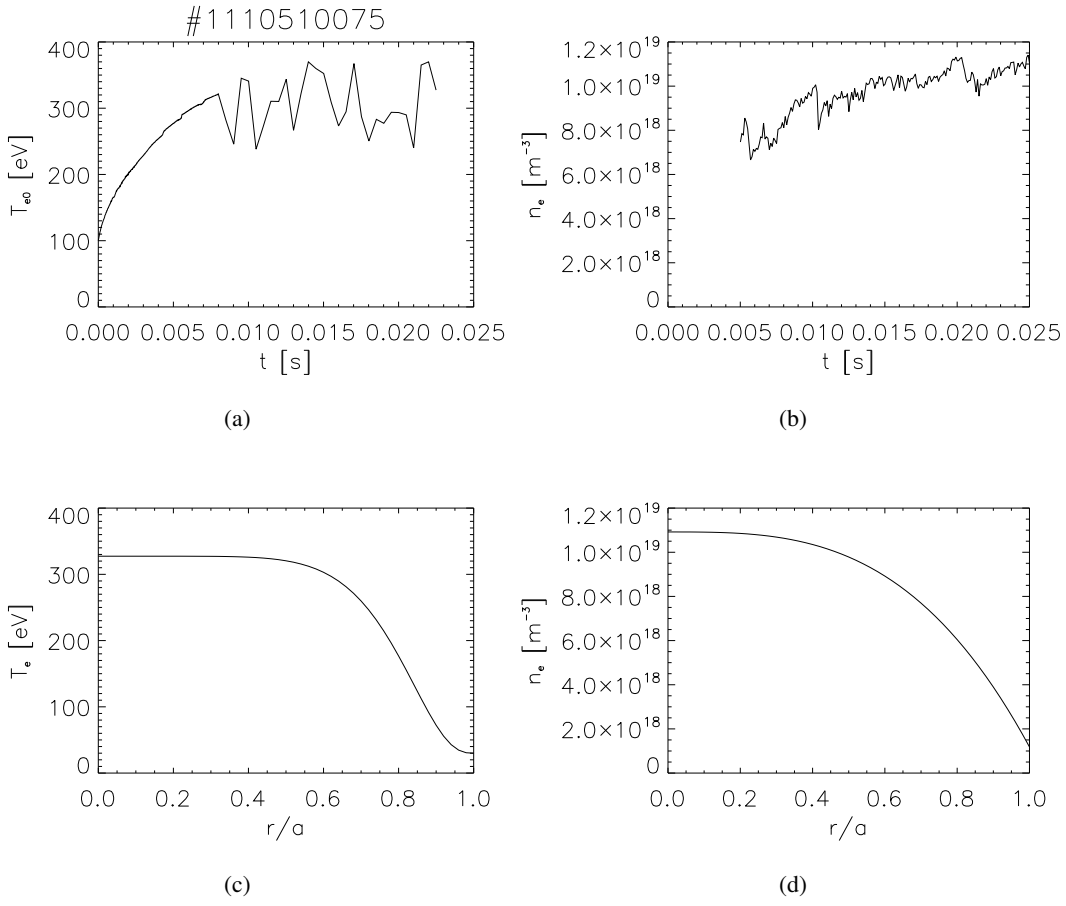

Figure 5.9: Code inputs: (a) Central electron temperature from Thomson scattering. (b) Electron density from CO_2 interferometer. (c) Electron temperature profile. (d) Electron density profile.

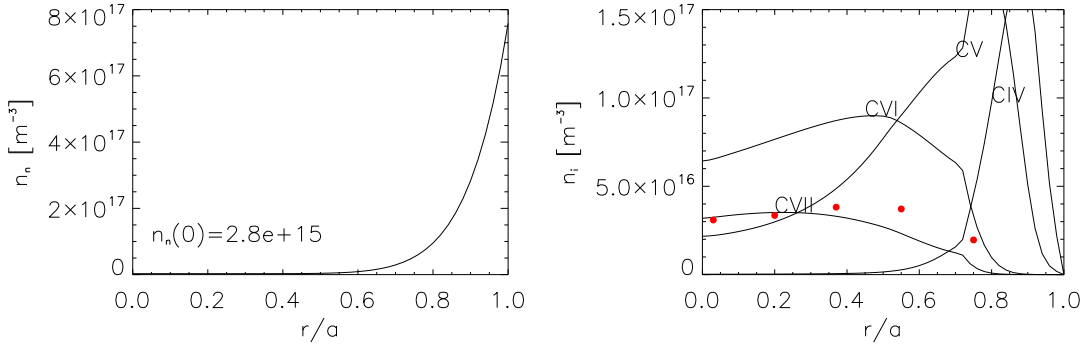

(a) (b)

Figure 5.10: (a) Original neutral density profile from NENÈ code. (b) C IV-VII population profiles away from sawteeth computed by the transport code (lines) and C VII density measured by CHERS (red circles). Experimental data are averaged over similar discharges. Error bars represent standard deviation of the mean from samples. Note that in this case error bars are of the order of $\sim 10^{15}\mathrm{m}^{-3}$.

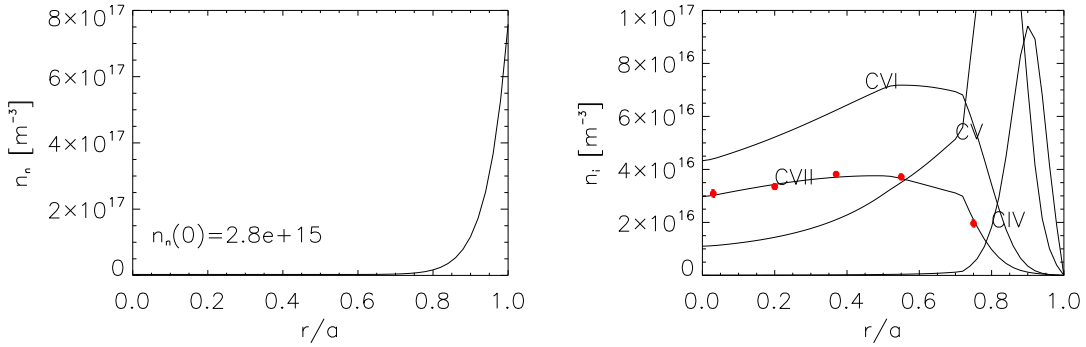

(a) (b)

Figure 5.11: (a) Modified neutral density profile. (b) C IV-VII population profiles away from sawteeth computed with the modified neutral profile. Total amount of C is reduced compared to the previous simulation in order to fit the experimental points.

it is often believed that the neutral densities estimated with this method are too high; the carbon transport simulation confirms this supposition.

After those considerations, we try to reduce the neutral penetration moving the neutral profile closer to the edge (Fig. 5.11(a)). In this way a better agreement between the simulated C^{+6} population and the experimental data is reached, as shown in Fig. 5.11(b).

In this type of simulation the reconstruction of the impurity content is made upon measurements which represent a steady-state situation, since they are carried out away from sawteeth, where the plasma is considered to be in the steady state. Moreover the measurements are averaged in time and over similar discharges. The simulation, in the same way, reproduces the carbon content once it has stabilised over time, after an initial phase during which it is evolving, usually lasting $\sim$ 15 ms. With this type of analysis in principle only the peaking factor (v/D) could be determined. Instead, the simulation is found to be sensitive to the multiplication of the coefficients by a common factor. In particular by dividing or multiplying both D and v for 5 and 10 the match between the simulated and measured fully stripped carbon profile is lost. Moreover, since these coefficients are used in the first standard-regime part of the PPCD discharge simulation, as it will be described in Section 5.5, if D and v are divided or multiplied by a common factor, the agreement between measurements and simulation in the carbon time evolution during the PPCD period is also lost. For these reasons, we conclude that a separate determination of the two coefficients is possible in this case, even in the absence of transient impurity measurements.

The profiles of the transport coefficients are shown in Figs 5.12(a) and (b). They are chosen firstly finding the good function among linear functions between two consecutive spatial nodes and fixing the position of the nodes. All this is done by trying to minimise the simulated and measured carbon population. Afterwards, the precise values of the coefficient in the inner and outer regions are found applying the method of the minimum chi-square for the two regions separately. At the end uncertainty regions are estimated drawing confidence ellipses, applying the method explained in Section 5.2.3. Moreover, since these coefficients are also used in the standard-regime part of the PPCD discharge, the uncertainty regions take also into account any possible variations of the standard D and v which do not compromise the agreement between simulation and measurements in the PPCD discharge.

The estimated transport coefficients denote a region in the first part of the radius of strong diffusion and high outward convection which lead to a nearly flat impurity profile. These coefficients differ in magnitude and shape from the classical ones, as we shall see in Section 5.4.3; this is expected since standard discharge in MST has multiple, coupled tearing modes and the magnetic field lines have some degree of stochasticity which leads to a high D value and produces a flat impurity density profile.

Confidence ellipses give also a measure of the linearity of the model in the coefficients and of the correlation between the coefficients themselves. Ellipses in Fig. 5.12(c) show that the model is linear in the two coefficients in the inner region. There, a positive correlation exists between them: the peaking factor (v/D) does not vary significantly along the major axis of the ellipses. Fig. 5.12(d) shows that a more complex relationship is present between the two parameters in the outer region. Here the model presents a nonlinearity in the two parameters, as the contours are distorted. This may be due to the influence of another parameter which perturbs the relationship between the model and the two transport coefficients. It may be the neutral influx from the wall which strongly determines the impurity behaviour near the edge. In the simulation it is forced to remain constant on varying D and v due to the lack of its absolute measurement. Furthermore

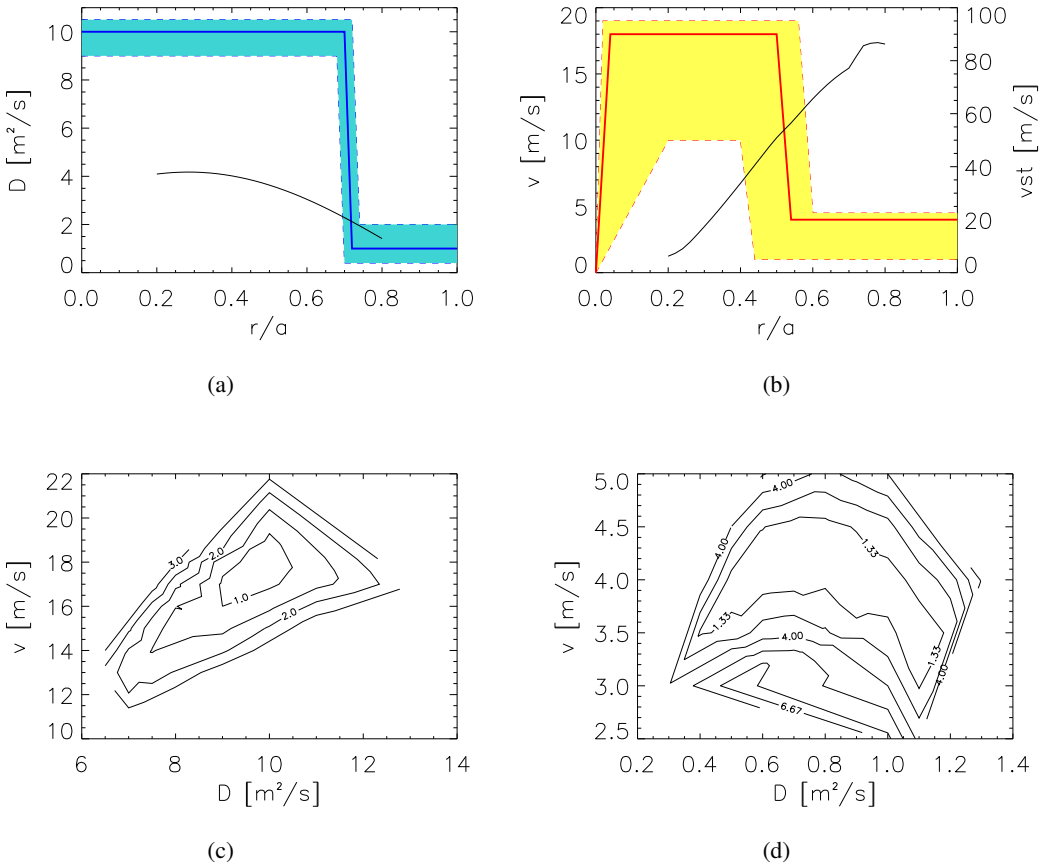

Figure 5.12: D (a) and v (b) profiles estimated for standard discharge with uncertainty ranges indicated by the respective coloured areas. In black the stochastic coefficients. Confidence ellipses drawn for core (c) and edge (d) regions in standard discharge.

it has to be considered that in the external region the content of C^{+6} is very low as well as the number of the experimental points on which this analysis is performed.

5.3.3 Stochastic transport coefficients

Since standard plasmas are characterised by a high level of stochasticity, the calculation of D and v in a stochastic field is applied and compared with the experimentally determined coefficients. The impurity radial flux through a stochastic magnetic field is proportional to the diffusion coefficient of the stochastic magnetic field (also called magnetic diffusion coefficient), which depends on the magnetic fluctuations (see Section 1.6.2 for the analytical description of stochastic transport). For MST's standard plasmas the magnetic diffusion coefficient was calculated by B. Hudson applying the field line tracing code MAL [116]. MAL traces the magnetic field lines given the equilibrium field reconstruction by the code MSTFIT [117] and the mode amplitudes from the resistive MHD code DEBS [118] properly scaled to the mode amplitudes measured at the edge. MAL solves the field line equations and evaluates the following to arrive at a value for

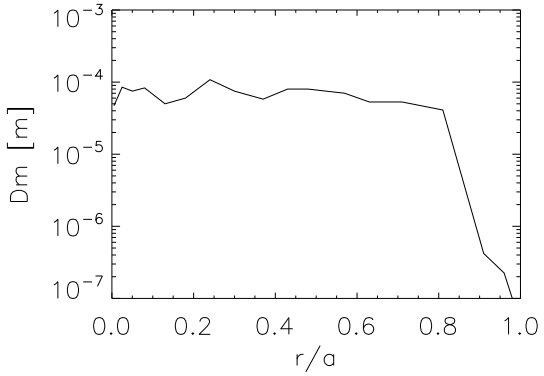

Figure 5.13: Magnetic diffusion coefficient calculated with the field line tracing code. The values at $r/a < 0.2$ and $r/a > 0.8$ are not valid there since the system is not diffusive in those regions. [116]

the magnetic diffusion coefficient D_{m}

$$D_{\mathrm{m}} = \frac{\left\langle (\Delta r)^2 \right\rangle}{2\Delta l} \tag{5.4}$$

where Δr is the radial excursion of the magnetic perturbation, Δl is the field line length, and the brackets denote an average over a large number of realisations.

The magnetic diffusion coefficient is plotted in Fig. 5.13. It has to be noted that the validity of the MAL calculation of the magnetic diffusion coefficients is not valid at $r/a < 0.2$ and $r/a > 0.8$. In those region the system described by MAL cannot be considered purely diffusive due to imposed constraints (at the boundary $r = 0$ and near the reversal surface) and the calculation of the magnetic diffusion coefficient is not valid.

With this magnetic coefficient it is then possible to compute the transport coefficients of the stochastic magnetic field (following Eq.1.32) and make a comparison with the ones found experimentally by matching carbon density measurements. This comparison is shown in Figs 5.12(a) and (b). Stochastic D is lower than the experimental D, but both have their maxima in the core region and then decrease at the edge. Instead, stochastic v has the maximum near the edge, contrary to the velocity found with the transport code. Theoretical v is also a factor of 5 greater.

Considering the limit of a steady-state analysis, we may conclude that the diffusion coefficient can be considered qualitatively consistent with a diffusive transport driven by the magnetic fluctuations, which are greater in the core region. On the other hand, estimated convective velocity behaves differently from the stochastic calculation.

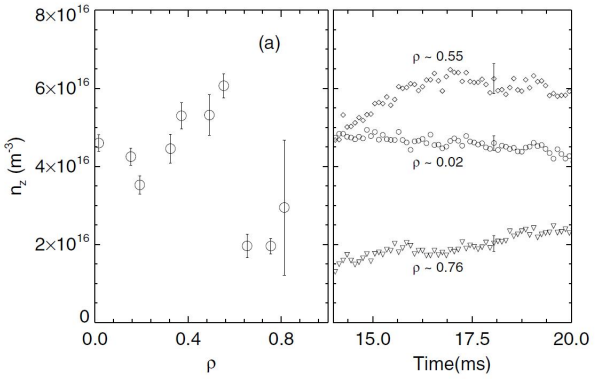

Figure 5.14: C^{+6} density for PPCD discharge measured by CHERS: (a) radial profile and (b) temporal evolution after transition to improved confinement at three radial locations: core ($\rho \sim 0.02$), mid-radius ($\rho \sim 0.55$) and outer regions ($\rho \sim 0.76$) of the plasma. Data are averaged over similar discharges. Error-bars represent standard deviation of the mean from samples. [61]

5.4 PPCD discharge

PPCD discharge is composed of a first part (about 10 ms) of standard discharge, then PPCD is activated and the discharge enters the improved confinement regime. In this regime tearing modes are suppressed. The electron temperature profile steepens in the outer region of the plasma, and the central electron temperature increases substantially, exceeding 1.5 keV at high toroidal plasma current (> 500 kA). Edge temperature decreases. Ion temperature does not change significantly. The density profile broadens and becomes hollow and the edge density decreases. This improved regime lasts for $\sim$ 10 ms and afterwards the discharge returns in standard mode.

5.4.1 CHERS impurity measurements

The impurity behaviour, once the discharge enters the PPCD mode, changes dramatically (Fig. 5.14). CHERS measurements made on carbon revealed an apparent decay of the core impurity density after this transition. The impurity density in the outer region of the plasma, on the other hand, is slowly increasing. The profile in the core region ($0 \leq \rho \leq 0.6$) approaches a stationary hollow shape towards the end of PPCD [61].

Impurity density measurements were made also during higher current PPCD discharge for different impurity ions, namely B^{+5}, C^{+6}, O^{+8}, Al^{+11} and Al^{+13}. Higher current means higher electron temperature allowing to those higher charge states of ions to be measured. The experimental data are reported in Fig. 5.15. Low-Z impurities like boron and carbon show a similar behaviour with respect to medium current discharge: a clearly hollow profile and slow decay in the core of the plasma. The electron temperature in PPCD is not high enough to fully ionise all the higher-Z impurity atoms in the plasma. Hence, density decay for higher-Z impurities is not expected, even though a hollow radial profile is observed for all impurity species. As an example, the O^{+8} density, which has a flat radial profile at the beginning of PPCD, increases due to an increase in ionisation and starts to decay only towards the very end of PPCD, slowly evolving to a hollow radial profile. Due to the steadily increasing electron temperature, which

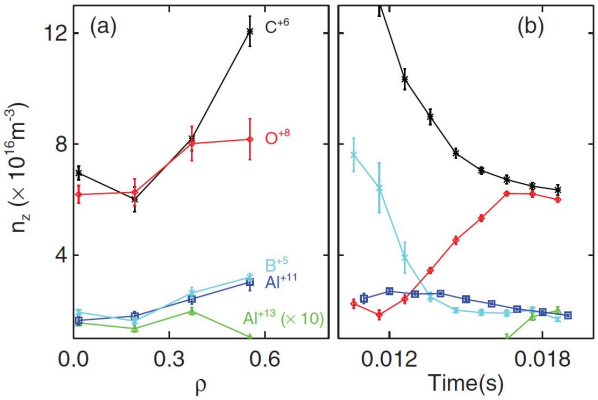

Figure 5.15: Various impurity ion densities for high current PPCD discharge measured by CHERS: (a) Radial profiles towards the end of PPCD. (b) On-axis temporal evolution during PPCD. Data are averaged over similar discharges. Error-bars represent standard deviation of the mean from samples. [56]

is not high enough to fully strip all aluminium ions, the aluminium charge state distribution is constantly evolving throughout PPCD.

5.4.2 Transportless ionisation equilibrium

We start the analysis of the impurity behaviour in PPCD plasmas comparing the CHERS impurity density measurements with a simple no-transport scenario, the ionisation balance of an element in equilibrium in a thermal plasma. Fractional abundances of the ions of the main impurities are calculated using ADAS405 [59]. This routine computes the ionisation equilibrium of an element as a function of given T_e, T_i, n_e and n_n, by means of CR rate coefficients for ionisation, recombination and charge-exchange processes. The plasma parameters used for this calculation are the typical parameters for high current PPCD discharge: $T_e(0) = 1.7$ keV, $T_i(0) = 680$ eV, $n_e(0) = 8 \times 10^{18}\,\mathrm{m}^{-3}$, $n_n(0) = 9 \times 10^{14}\,\mathrm{m}^{-3}$.

Fig. 5.16 shows the results of the ionisation equilibrium normalised to the central value of the CHERS measurements. It is quite evident the disagreement between this equilibrium and the ion populations. The measurements reveal a hollowing in the impurity profiles while the model predicts a flat profile for all the fully stripped ions. That model is a poor model for studying the impurity behaviour in MST's PPCD plasmas as it does not consider transport phenomena which strongly characterise the impurity abundances in this plasma. A more complete model, which must include transport, is therefore needed to fully reproduce the behaviour of the impurities.

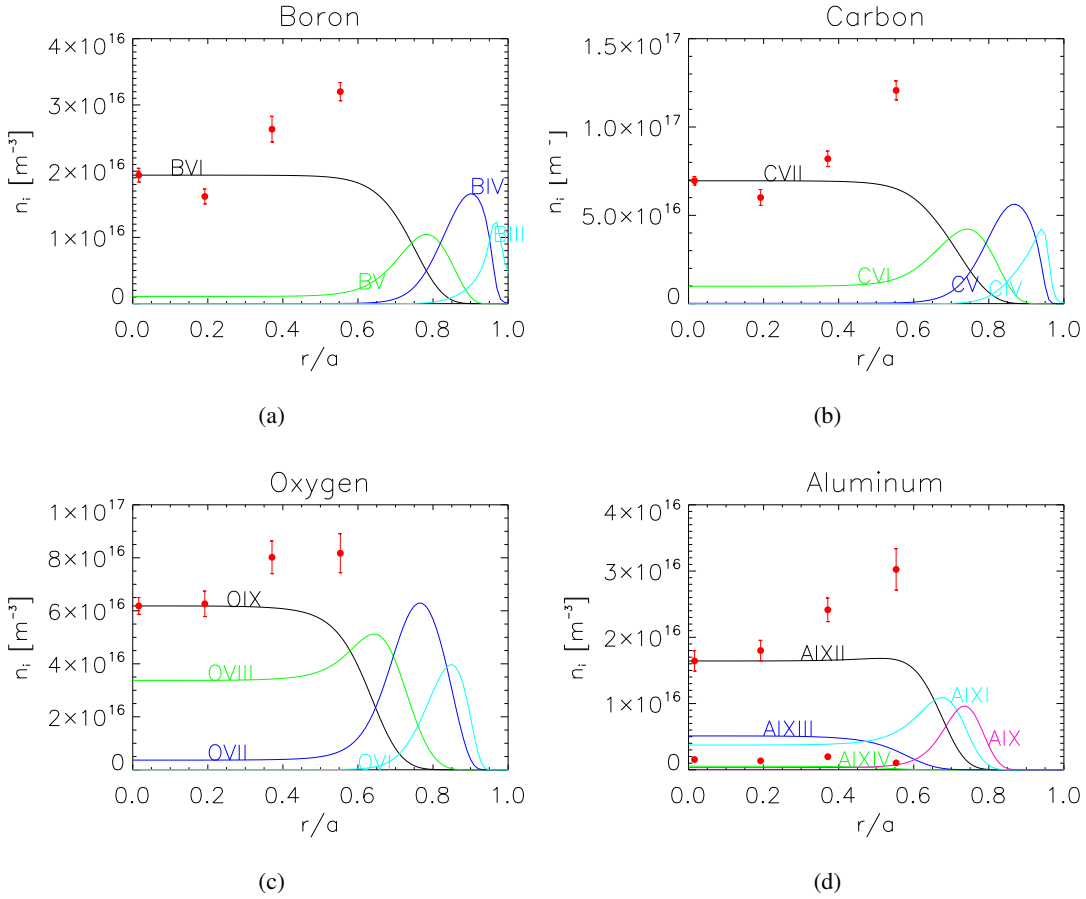

Figure 5.16: Ionisation equilibrium without transport (lines) and CHERS measurements (circles). Error bars represent standard deviation of the mean from samples.

5.4.3 Classical transport model

Radial impurity flux can be evaluated analytically considering the flux due to Coulomb collisions. This is the classical approach to transport phenomena in which binary Coulomb collisions in a straight magnetic field are considered. Cross-field transport phenomena deriving from toroidal geometry are neglected. This is a reasonable assumption as we have already pointed out in Section 2.2: in RFPs particle transport due to collisions is classical.

We shall consider a fully ionised multi-species plasma of electrons, main ions and several species of ions in different charge states. We shall assume all species and main ions to have the same temperature profile, as the impurity-main-ion energy equilibration time (~ 0.1ms) is much less than the particle confinement time ($\sim 30 - 40$ ms). This is consistent with majority and minority ion temperature measurements in PPCD plasmas [106]. The radial flux of the particle of the considered species is given by Eq. (1.21)

Considering a 1-D situation and expressing the radial flux as the sum of a diffusion and a convective term : $\Gamma_\alpha = -D\frac{\partial n_\alpha}{\partial r} + v\, n_\alpha$, we can rearrange the terms in Eq. (1.21) and obtain the classical values of the transport coefficients

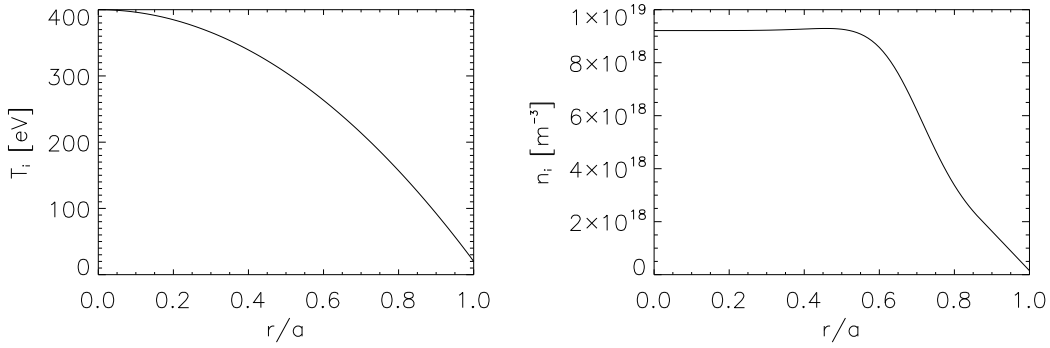

(a) (b)

Figure 5.17: (a) Radial profile of the ion temperature used in the model. (b) Radial profile of the main ion density used in the model calculated from n_e and impurity density profiles, assuming charge neutrality.

$$D_\alpha = \rho_\alpha^2 \sum_\beta \left(\frac{m_\beta}{m_\alpha + m_\beta} \right)^{1/2} \nu_{\alpha\beta} \tag{5.5}$$

$$\begin{aligned} v_\alpha = \rho_\alpha^2 \sum_\beta \left(\frac{m_\beta}{m_\alpha + m_\beta} \right)^{1/2} \nu_{\alpha\beta} \left\{ \frac{Z_\alpha}{Z_\beta} \frac{1}{n_\beta} \frac{\partial n_\beta}{\partial r} + \right. \\ \left. - \left[1 - \frac{Z_\alpha}{Z_\beta} + \frac{3}{2} \frac{m_\beta}{m_\alpha + m_\beta} \left(\frac{m_\alpha Z_\alpha}{m_\beta Z_\beta} - 1 \right) \right] \frac{1}{T} \frac{\partial T}{\partial r} \right\} \end{aligned} \tag{5.6}$$

The ion temperature and main ion density (calculated from the electron and impurity density profiles assuming charge neutrality) used in this calculation are shown in Fig. 5.17. Impurity density profiles for boron, carbon and oxygen are reconstructed through the transport codes starting from CHERS measurements, as we shall describe in Section 5.5.2. Impurity density profiles for aluminium are instead reconstructed through interpolation of CHERS measurements (Al^{+11}, Al^{+13}) and with ADAS ionisation equilibrium (Al^{+10}, Al^{+12}) [105]. The classical transport coefficients are calculated for the dominant species (B^{+5}, C^{+6}, O^{+8}, Al^{+11}) considering collisions with all species in the most populated charge states. The results are shown in Fig. 5.18.

Searching for dependencies of the transport coefficients on mass and charge for the different species in Eqs (5.5) and (5.6), we find that there is no dependence for D, whereas v has a dependence on Z (replacing $m_\alpha \sim 2Z_\alpha$ which is reasonable for fully stripped ions). These trends come out by looking at Fig. 5.18: D is almost constant for the different species, while the Z dependence of v is evident especially in its outer region.

The uncertainty of this calculation was estimated to be around 10%, due to experimental uncertainties of ion density measurements and to the uncertainty of the Coulomb logarithm value in the collision frequency expression. Other errors coming from other measured quantities (temperature and density of electrons and main ions) are evaluated to be smaller. In the outer

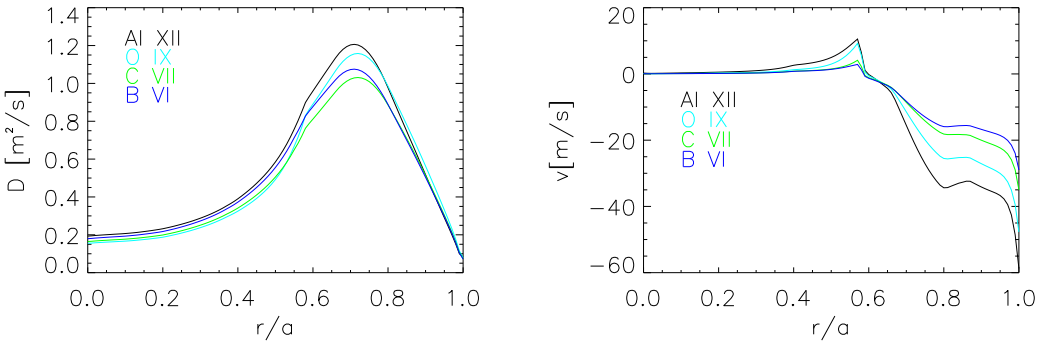

(a) (b)

Figure 5.18: Radial profile of the transport coefficients for different species computed using the classical model for PPCD discharge.

part CHERS data are not available; the impurity density profiles are computed by the codes starting from CHERS measurements for the inner radius but with no experimental points for the outer part (see Fig. 5.29). It should also be noted that the reliability of the calculated theoretical transport is reduced at the very edge ($\rho > 0.9$) where the electron and ion temperature and density profiles are affected by higher experimental uncertainties.

5.5 PPCD impurity transport analysis

Transport coefficients are now estimated by the impurity transport codes. The simulated population abundances are compared with the measured impurity densities; D and v are varied until the best reproduction of the experimental data is achieved.

In PPCD discharge simulation the attention is focused on reproducing the impurity radial profile towards the end of PPCD (at 18ms) as well as the impurity density time evolution in three different plasma regions as what was measured by CHERS.

PPCD discharge is composed of two distinct parts (standard and improved confinement regime) which are characterized by different types of transport. Therefore two different couples of transport coefficients have to be used for the two phases. For the standard part the simulation uses coefficients similar to those estimated for the standard discharge. Then for the PPCD period, suitable coefficients must be found by searching for the best agreement with the experimental signals.

5.5.1 Medium current PPCD discharge

Carbon transport simulation is performed for PPCD discharge at medium current ($\sim$ 400 kA) reproducing the fully stripped carbon measurements (Fig. 5.14).

The chosen shot to be reproduced is #1090524034. In Figs 5.20 and 5.21 are shown the inputs to the code. The first part of the central electron temperature time evolution, where there are not data from Thomson scattering, is assumed starting from an initial value set to 100 eV

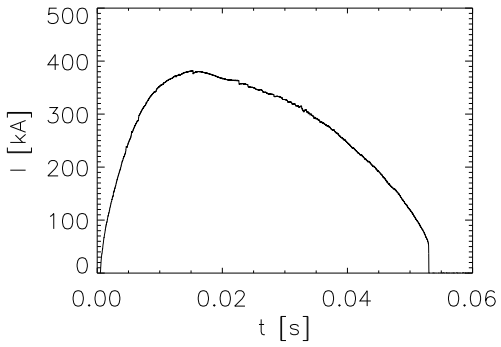

Figure 5.19: Plasma current for a 400 kA PPCD discharge.

and then reaching the first TS measurement with a time evolution similar to that of the plasma current ramp. The evaluation of the first value of the electron temperature is made without any experimental evidence. However, even if it were not correct, this would not influence the simulation since the temperature grows up immediately. Electron temperature profile is fixed in shape during the first part of the discharge then, from the TS switching on, the profile is obtained from the TS data and it varies at the same temporal rate of the measurements (0.5 ms). Electron density profile is fixed in shape during the standard part of the discharge then, during PPCD, it evolves in a weakly hollow profile at the end of PPCD according to FIR interferometry measurements (time resolution of 1 ms). Neutral density profile has been reconstructed through NENÈ code for medium current PPCD discharge. Carbon influx time evolution is assumed in order to reproduce the experimental C III line intensity measured by the IMA which is compared with the same line computed by the code (see Fig. 5.21). The influx decreases towards PPCD, then remains constant until the end of PPCD, and then it increases again.

Classical transport coefficients

As first attempt, the classical coefficients for carbon are used in the simulation (Fig. 5.18). Black lines in Fig. 5.22(a) show the C^{+6} experimental temporal evolution at three minor radial locations ($\rho \sim 0.15, 0.55, 0.76$) and red circles in 5.22(b) show the experimental radial profile of C^{+6} towards the end of PPCD. These data comes from CHERS measurements and they have already been presented in Section 5.4.1. Red lines in Fig. 5.22(a) and black lines in Fig. 5.22(b) show the results of the simulation performed using the classical transport coefficients. The experimental impurity behaviour is not satisfactorily reproduced with these coefficients. In fact while the carbon profile at 18 ms is reproduced in good approximation, the time evolution of carbon content in the three radial locations is not; classical transport coefficients produce a high increase of carbon content in the central region ($0 \leq \rho \leq 0.6$) during the PPCD phase which does not decrease towards its end like the measurements. Stronger outward velocity in the first part of the radius is needed for diminishing the central carbon content. Ad-hoc transport coefficients need to be drawn in order to lead to a better agreement with the measurements.

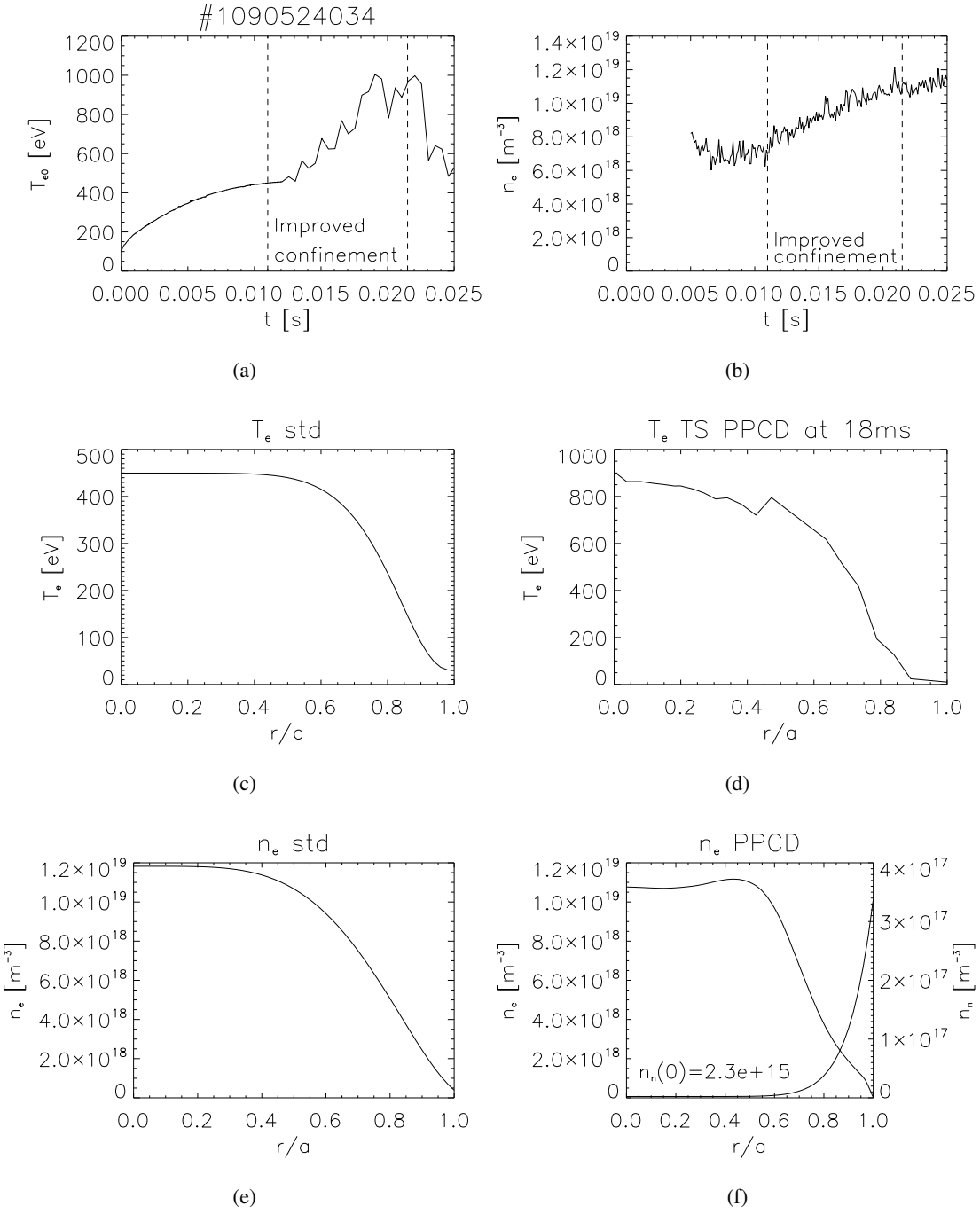

Figure 5.20: Code inputs: (a) Central electron temperature from Thomson scattering. (b) Electron density from CO_2 interferometer. (c) Electron temperature profile during standard part. (d) Electron temperature profile at the end of PPCD from smoothing Thomson scattering measurements. (e) Electron density profile for standard part. (f) Electron and neutral density profiles for PPCD part.

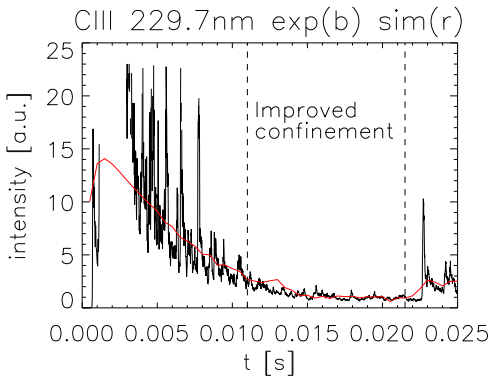

Figure 5.21: C III (229.7 nm) line intensity measured by the IMA at $\rho > 0.85$ (black) and chord integrated line intensity computed by the code (red).

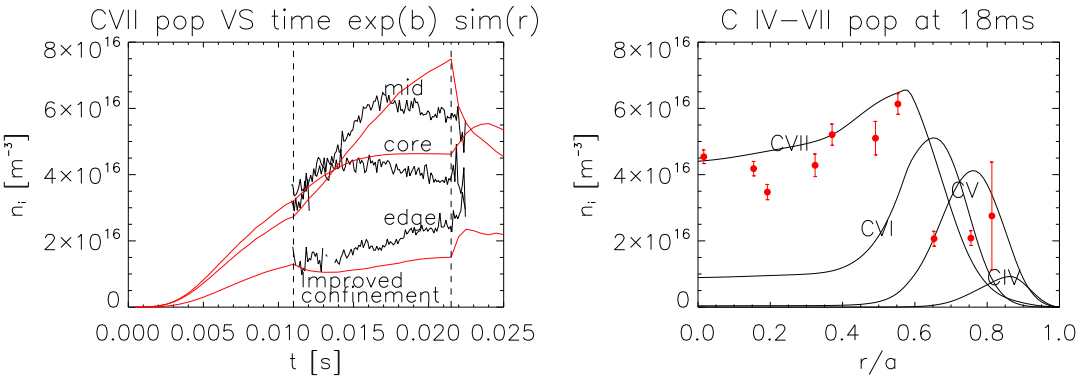

(a) (b)

Figure 5.22: (a) C VII population time evolution at $\rho \sim 0.15$ (core), 0.55 (mid), 0.76 (edge), measured (black) and simulated (red). (b) C IV-VII population profiles at the end of PPCD computed by the transport code (lines) and C VII density measured by CHERS (red circles). Experimental data are averaged over similar discharges towards the end of PPCD [17-19 ms]. Error bars represent standard deviation of the mean from samples. This simulation is performed using the classical transport coefficients for carbon.

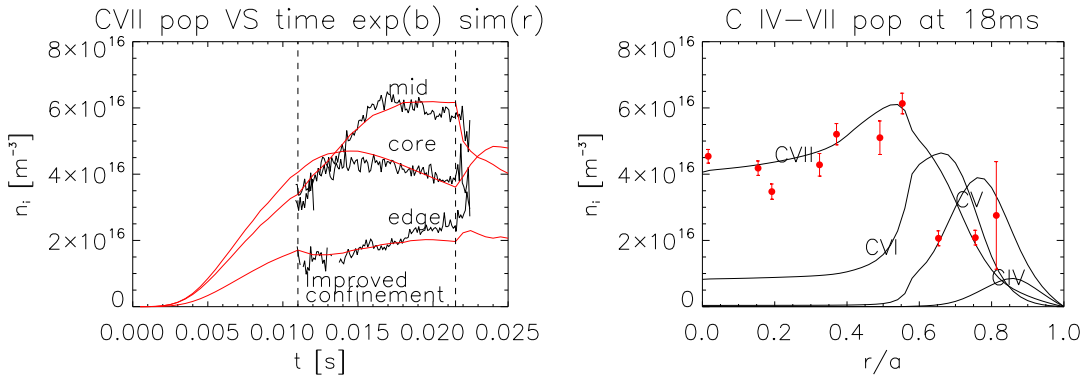

(a) (b)

Figure 5.23: (a) C VII population time evolution at $\rho \sim 0.15$ (core), 0.55 (mid), 0.76 (edge), measured (black) and simulated (red). (b) C IV-VII population profiles at the end of PPCD computed by the transport code (lines) and C VII density measured by CHERS (red circles) with corresponding error bars. This simulation is performed using ad-hoc step-function profiles for the transport coefficients.

Transport coefficients determination

Now transport coefficients are seeking among simple functions linear between two consecutive spatial nodes. First a preliminary profile, which produces a good agreement with the experimental points, is drawn and the position of the nodes is set. Then the minimum chi-square method is applied to the C^{+6} time evolution in order to find the D and v values in the core and edge regions. Finally drawing the confidence ellipses for the two regions allows to evaluate the uncertainty of the coefficients values.

Fig. 5.23 shows the comparison of C^{+6} density between the simulation and the experiment using ad-hoc step-function profiles for the transport coefficients (Fig. 5.24). The combination of strong outward velocity and a diffusion coefficient which is lower in the core and higher in the edge region leads to a very good agreement between the simulated curves and the experimental data.

Fig. 5.24 reports the estimated D and v together with the classical ones for comparison. The new coefficients are different from those predicted by the classical model: D is higher in the external region; v is greater when is outward in the central region and it reverses its direction at a greater ρ. Nevertheless the experimental transport coefficients agree within a factor lower than 2 with the classical calculation in the region of the profile which is constrained by CHERS data; it is possible to say that transport in MST during PPCD is nearly classical.

The confidence ellipses in Fig. 5.25 indicate that the model is linear in the coefficients in both the inner and outer region. Positive correlation exists between the two coefficients in both regions but stronger at the edge. In this region on varying D and v also the value of carbon influx is varied in the simulation in order to maintain the good agreement between the experimental and simulated intensity of the C III line (Fig. 5.21). This causes the final shape to be sharp-cornered but the trend is linear, very different from what found for the edge region in the standard discharge (Fig. 5.12).

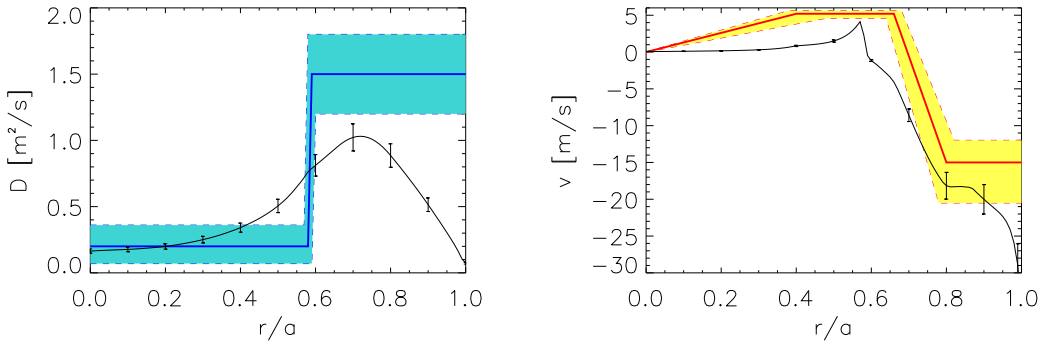

(a) (b)

Figure 5.24: D and v profiles estimated for the PPCD part of the discharge with uncertainty ranges indicated by the respective coloured areas. In black the classical coefficients for carbon with ±10% error bars.

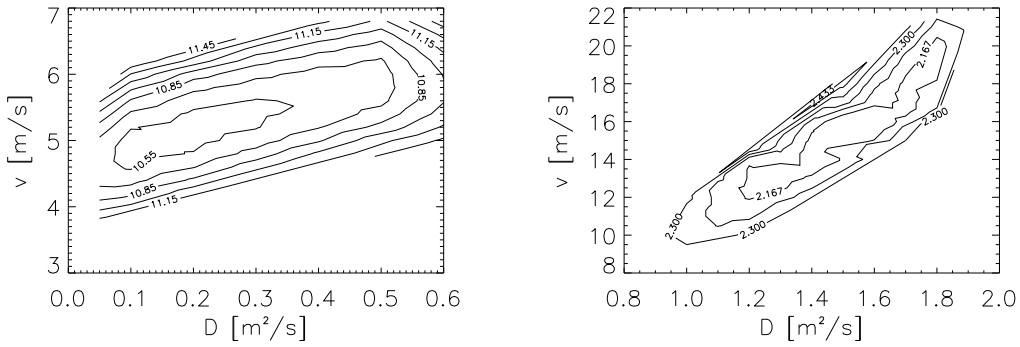

(a) (b)

Figure 5.25: Confidence ellipses drawn for core and edge regions in PPCD discharge. For core region χ^2 is computed considering time evolution measurements for all radial locations, while edge region χ^2 is computed considering time evolution measurements of three radial locations only ($\rho \sim 0.15, 0.55, 0.76$).

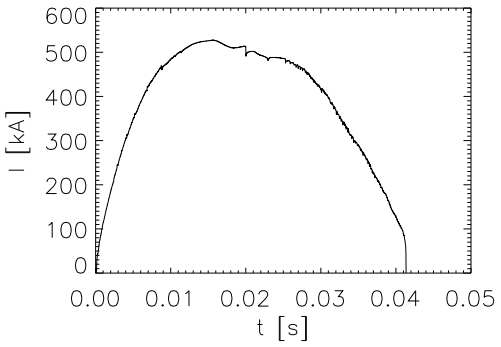

Figure 5.26: Plasma current for a 550 kA PPCD discharge.

5.5.2 High current PPCD discharge

The same method described in the previous section for simulating medium current PPCD discharge is applied to higher current PPCD discharge. For this type of discharge fully stripped ion radial profiles of boron and oxygen were measured by CHERS in addition to carbon (see Fig. 5.15). Thus B, C, O codes are run to simulate all three species behaviours. Aluminium ions density was measured too, but Al code is not available.

The chosen shot to be reproduced is #1110323024. In Figs 5.27 and 5.28 are shown the inputs to the code. Plasma measurements are inserted in the code as inputs using the same methods described in the previous section.

The transport coefficients estimated for carbon in medium current PPCD discharge (Fig. 5.24) are employed in these simulations in order to test their validity for different species in different plasma conditions. Fig. 5.29 shows the comparison between experiment and simulation for the considered impurities. The simulation well reproduces the experimental ion profiles. With this model and these few experimental points, the indication is that transport is almost equal between medium and high current PPCD discharges and that the impurity mass/charge is not a significant factor. In Section 5.4.3 we found that the classical D exhibits no dependence while v manifests a Z dependence which is more apparent in the outer region. The fact that transport simulations do not evidence this Z dependence of v may be explained considered that those simulations reproduce the experimental impurity profiles only for $0 \leq \rho \leq 0.55$ since there are no measurements for the outer part. Moreover the considered impurities have similar value of Z. So, it is reasonable that we do not see any dependence on the impurity mass/charge running the transport codes.

Fig. 5.29(e) shows Z_{eff} calculated summing up the contributions of the three species and adding the aluminium contribution from CHERS measurements [105]. This profile agrees with previous Z_{eff} estimate from X-ray measurements and modelling which ranged from 4 to 6 [119].

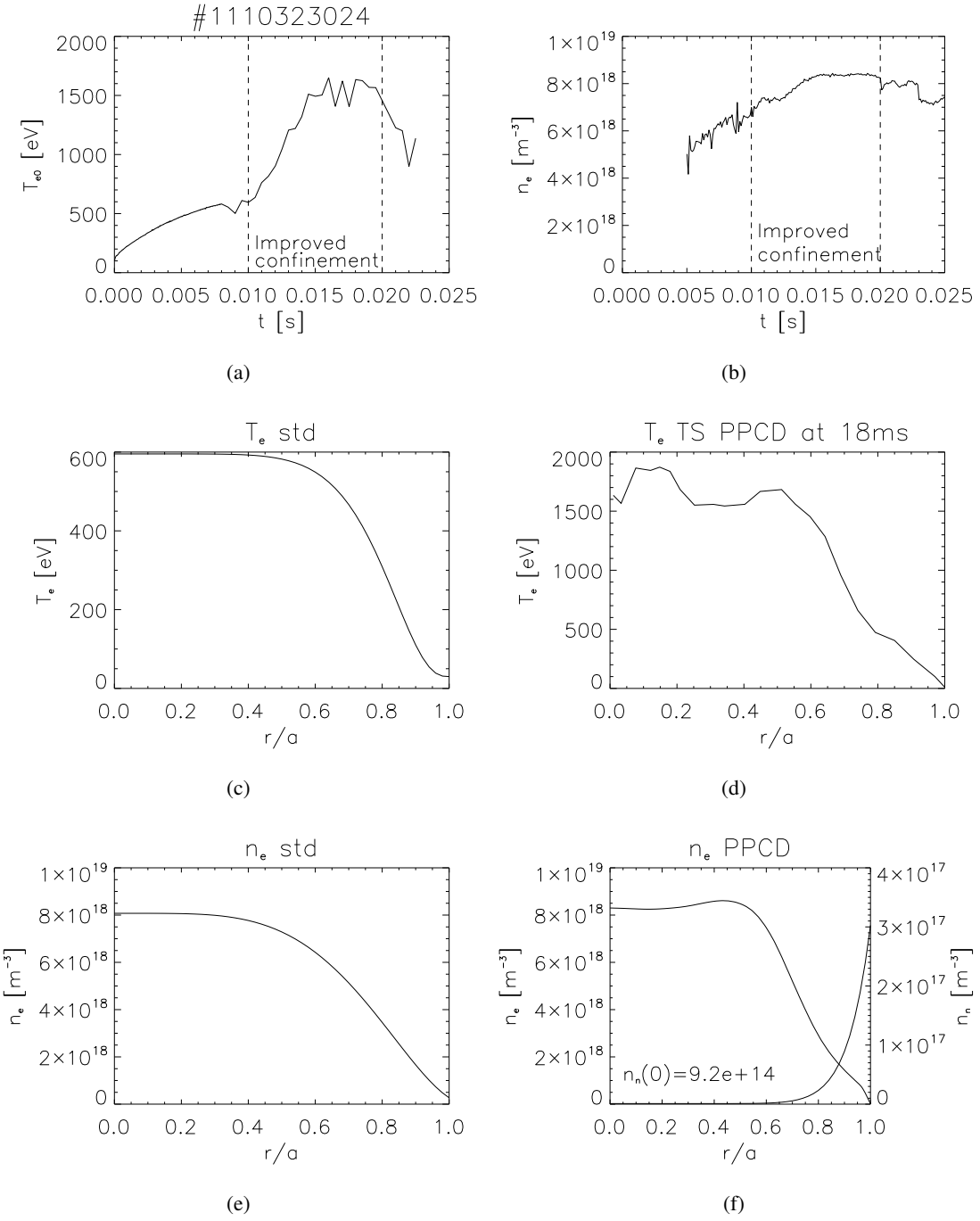

Figure 5.27: Code inputs: (a) Central electron temperature from Thomson scattering. (b) Electron density from CO_2 interferometer. (c) Electron temperature profile during standard part. (d) Electron temperature profile at the end of PPCD from smoothing Thomson scattering measurements. (e) Electron density profile for standard part. (f) Electron and neutral density profiles for PPCD part.

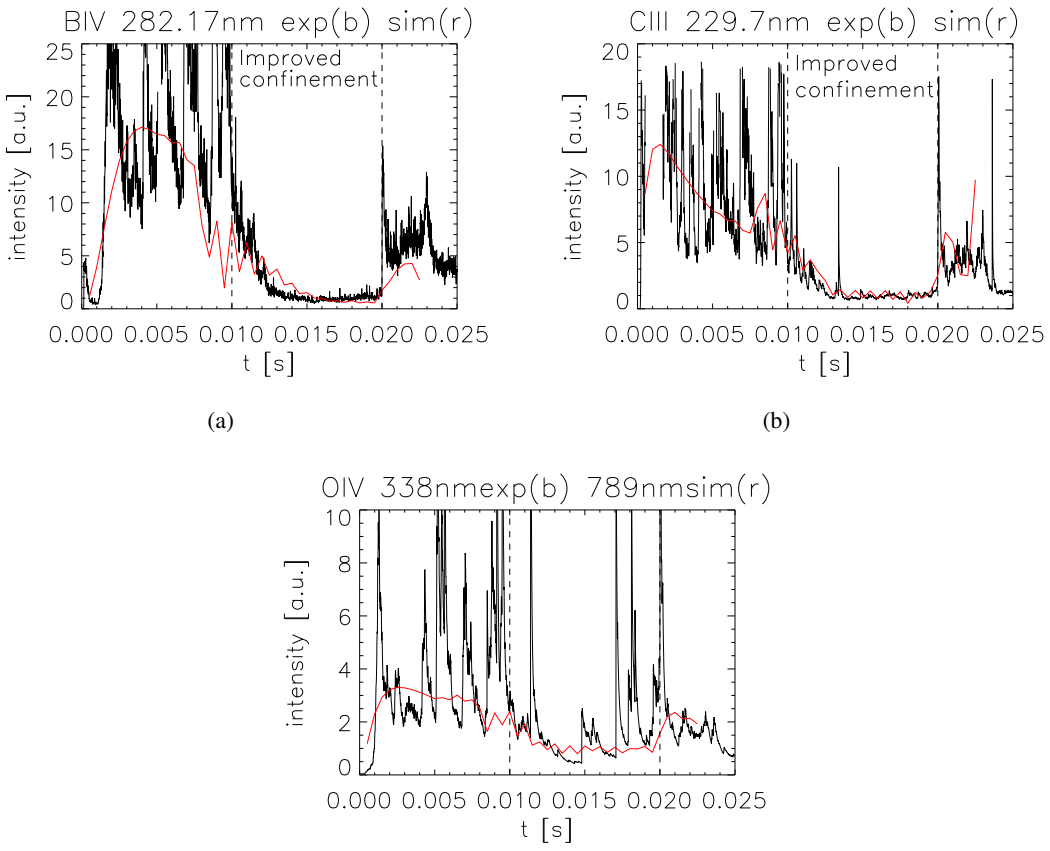

Figure 5.28: (a) B IV (282.17 nm) line intensity measured by the IMA at $\rho \sim 0.6$ to 0.9 (black) and chord integrated line intensity computed by the code (red). (b) C III (229.7 nm) line intensity measured by the IMA at $\rho > 0.85$ (black) and chord integrated line intensity computed by the code (red). (c) O IV (338.55 nm) line intensity measured by the IMA at $\rho > 0.85$ (black) and O IV (789.36 nm) chord integrated line intensity computed by the code (red).

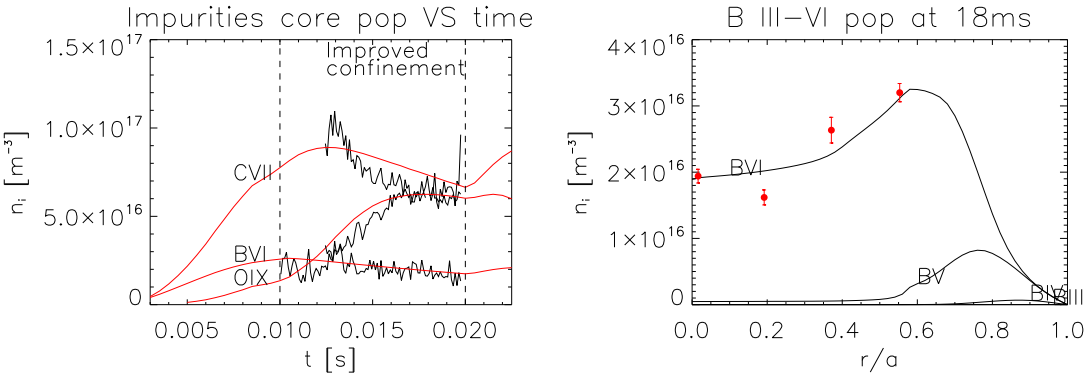

(a)

(b)

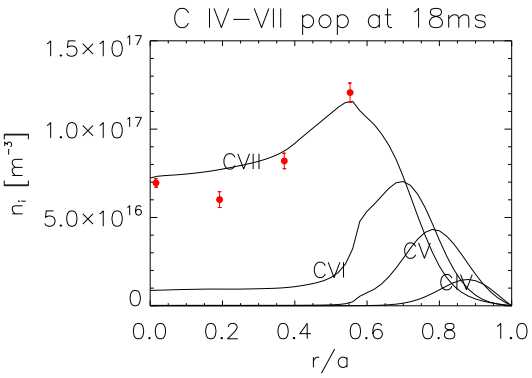

(c)

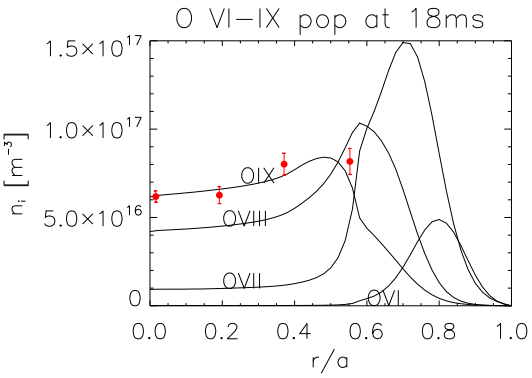

(d)

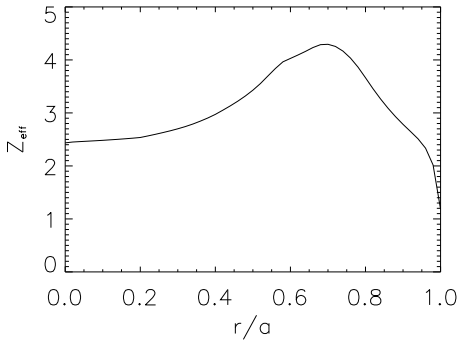

(e)

Figure 5.29: (a) B VI, C VII, O IX population time evolution at the core measured (black) and simulated (red). B III-VI (b), C IV-VII (c), O VI-IX (d) population profiles towards the end of PPCD computed by the transport code (lines) and B VI, C VII, O IX density measured by CHERS (red circles). (e) Z_{eff} computed by the code with contributions of B, C, O and Al. Experimental data are averaged over similar discharges. Error bars represent standard deviation of the mean from samples.

Soft X-rays simulation

Soft X-ray emission is reconstructed summing up the contributions of D, B, C and O computed by the collisonal-radiative codes. Aluminium and nitrogen contributions are lacking. In fact the experimental SXR measurements are much greater: in Fig. 5.30 the simulated SXR radiation is compared with the signal acquired by SXR tomography for different thicknesses of the Be filter installed on the diagnostic during high current PPCD discharges [120]. It is though that most of the missing radiation comes from Al ions, especially for the thinner filter (44 μm) which does not cut off Al line radiation.

In order to validate this supposition the SXR emission from Al is simulated using ADAS routines for the two thickest filters. The result is that Al emission is about 2 W/m^2 at the end of PPCD for the 421 μm Be filter and about 0.9 W/m^2 for the 857 μm Be filter. Nitrogen emission is not reproducible because of the lack of Ni content measurements. In any case it is estimated to be lower than Al emission due to the Ni lower atomic number. So, there must be another source of radiation in addition to impurities. This additional source may be a non-Maxwellian component of the electron distribution. In fact at MST there is some evidence that during PPCD, at higher energies, there is a measurable non-Maxwellian tail, and it is possible that this tail could extend down to the sensitivity range of the SXR detectors.

SXR brightness profiles are reproduced by the code and then normalised to be compared with the measured profiles from tomography reconstructions. The profiles are shown in Fig. 5.31 for different times during the PPCD period. The simulation well reproduces the experimental profiles.

5.6 The temperature screening effect

It has been shown that the main feature of the impurity behaviour during PPCD discharge is the expulsion of impurities from the plasma core. A possible mechanism for explaining this process is the classical "temperate screening effect", described in Section 1.6.1.

According to Eq. (1.21) temperature screening in a multi-species plasma is possible, in the presence of a negative temperature gradient, only if collisions take place with ions with mass and charge lower than the considered species. During the PPCD, the ion density profile is nearly flat in the plasma core and there exists a strong ion temperature gradient (see Fig. 5.17). Considering that collisions are likely to occur mainly with the main gas due to its concentration, temperature screening acts on all impurity species.

Looking at the profiles of the fully stripped ion densities at the end of the PPCD and at the temporal evolution of their core densities in Fig. 5.29, the effects of the temperature screening are clearly visible in the hollow profiles of B VI and C VII and in the decrease of their core density. Heavier species like O (and Al) are only partially ionised at MST's temperature. The ionisation balance is changing throughout the PPCD period and hence a clear indication of the outward flux is not present in the data: O IX core density increases during the PPCD and only at the end starts decreasing, assuming a slightly hollow profile.

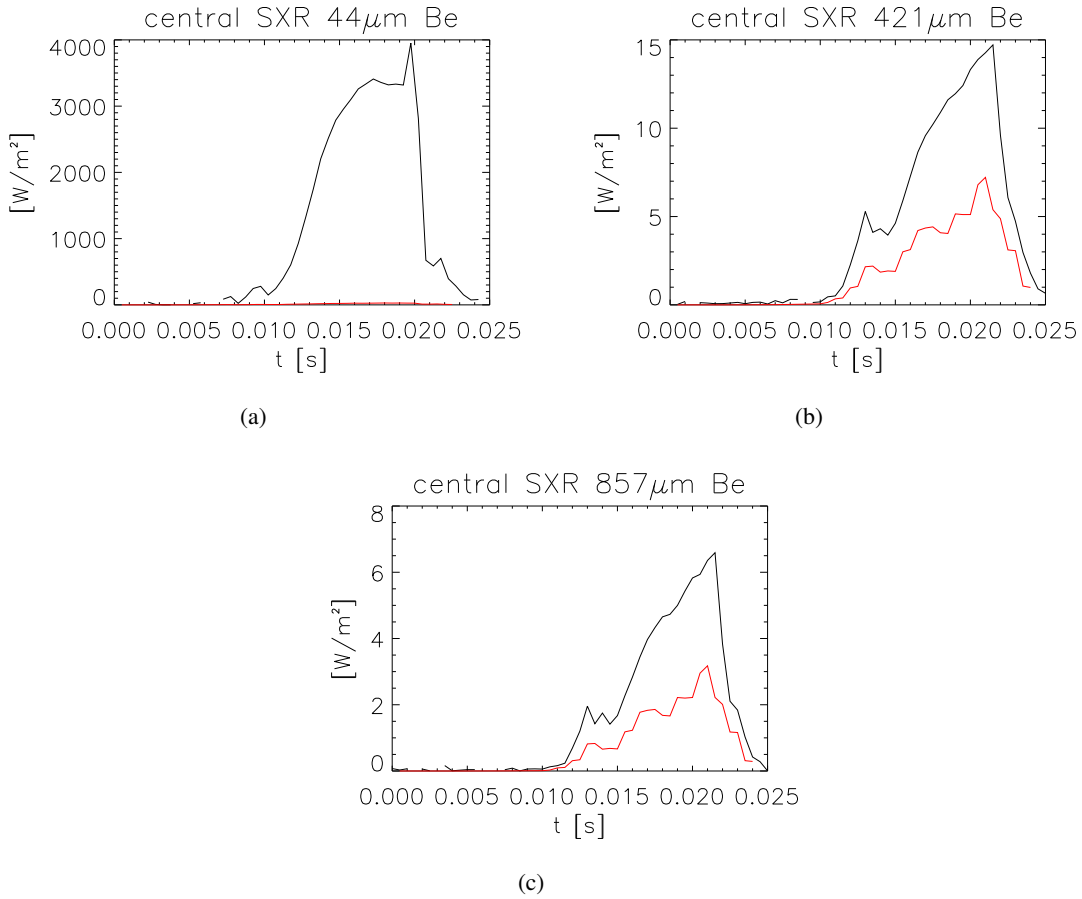

(a) (b)

(c)

Figure 5.30: Central chord SXR time evolution measured by SXR tomography (black) and reconstructed by the code without Al contribution (red) for different thicknesses of Be filter [μm]. (a) refers to shot #1110509105, (b) and (c) refer to shot #1121203031. All those are high current PPCD discharges with similar value of n_e.

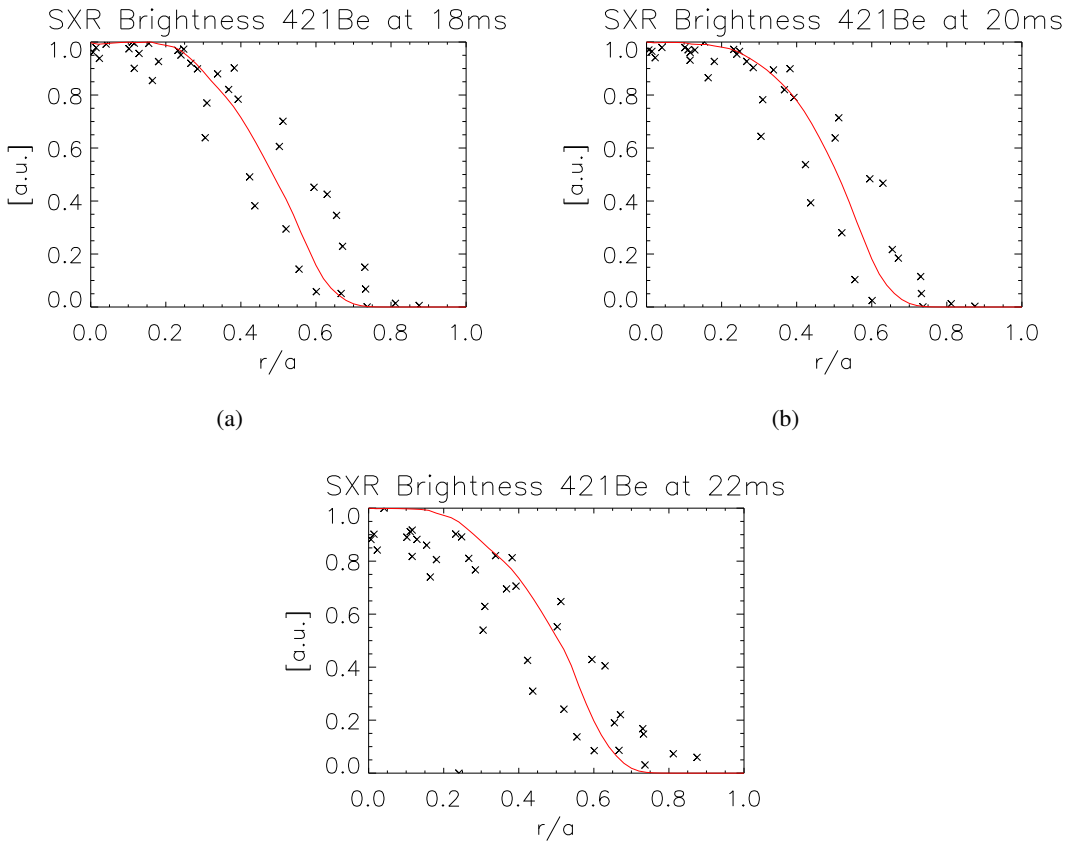

Figure 5.31: Normalised SXR brightness profiles for different times during PPCD: reconstructed by the tomography (×) and simulated (red lines).

5.7 Conclusions

Analysis of impurity transport in MST through simulations with the impurity transport code has been presented. The fully stripped ion radial profile of C, measured by charge-exchange recombination spectroscopy, have been reconstructed and radial profiles of transport coefficients for both standard and PPCD discharges have been deduced. B and O fully stripped ion radial profiles have been reconstructed for higher current PPCD discharge.

In standard plasmas transport is anomalous, with very high diffusion in the central region, resulting in nearly flat radial profiles of the fully stripped ion. A high flat D was assumed in the simulation, qualitatively consistent with the theoretical indications from the stochastic diffusion. Convective velocity is assumed to be highly outward in core region, not in agreement with stochastic calculation.

During PPCD magnetic fluctuations are reduced; impurity density decays in the core and evolves into a hollow radial profile, indicating outward convection of impurity ions. Estimated transport coefficients are low and close to classical values. Convective velocity is outward in the core region and then reverses its direction at mid-radius.

This impurity expulsion is supposed to be due to the "temperature screening effect" where the thermal force due to the ion temperature gradient expels impurities from the core of the plasma.

Additionally, high current PPCD simulations involving other species evidence the same transport and a mass/charge independence of the transport parameters.

In conclusion this study evidences a close-to-classical transport regime during the improved confinement whereas transport is more stochastic during standard discharge and consequently transport coefficients are higher.

Additional experimental data would help constrain the model; further measurements of impurity density especially at the edge in high current PPCD discharge would allow to both validate the step-function model and better calculate the classical transport coefficients.

Chapter 6

Summary and conclusions

In the research on the magnetically confined plasmas impurities play a crucial role. Radiation, transport, plasma-wall interaction and first wall conditioning are indeed key aspects - where impurities play important roles - which need to be controlled and understood.

ITER is currently under construction and it has been designed with beryllium facing components and tungsten divertor. The latter element, in particular, is attracting the scientists' attention because it may become a serious concern if were found to penetrate towards the core plasma. In this regard several W-oriented experiments are being carried out in different devices worldwide in order to figure out W transport properties.

On the other hand, light impurities have been exploited in several devices as radiative dissipators by reducing peak heat load near the edge. Light impurities have been used in seeded discharge through the creation of an external radiative layer which helps in dissipating energy, preventing hazardous loads to the wall.

In this context, a precise knowledge of the transport properties of the different species in different operating scenarios is mandatory.

This thesis has been dedicated to cast light on the impurity transport in the reversed-field pinch configuration. In this work intrinsic and injected impurity behaviour in different experimental scenarios has been studied, planning and executing devoted non-perturbing experiments based on different techniques, collecting data (impurity influx form the wall, selected line emissions, SXR profiles, total radiated power) and comparing the obtained emission patterns with the simulations of impurity transport codes. The simulation tool consists in a 1D impurity transport code coupled to a collisional-radiative code for different species. This code simulates the perpendicular transport of impurities and their radiative emissions. By comparing the simulation's results with plasma measurements, an assessment of the transport features (i.e. the coefficients which determine the radial transport) can be achieved.

In RFX-mod RFP this modus operandi had already been applied to study nickel and neon transport following their injection through laser blow-off and gas puffing. In this work this method has been extended to other impurities injected with a different technique: carbon and lithium entering the plasma as solid pellets.

The activity on RFX-mod started with a simulation of the radiation emitted by intrinsic impurities (C and O) in a typical high current discharge, in which the plasma spontaneously moves between the two magnetic regimes (MH and QSH). This simulation allowed to have a first estimate of the transport coefficients for the intrinsic impurities in both magnetic regimes.

Then, transient experiments with solid C pellet injections have been carried out in both magnetic regimes. The successful reproduction of the enhancement in the density and radiative emissions of the plasma after the injection, as well as SXR brightness profiles, permitted to validate the transport coefficients previously estimated for intrinsic impurities. A strong outward convective velocity is found in the external region, wider in the QSH regime. This positive pinch velocity confines impurity ions in the outer region, similarly to what was previously observed with Ni and Ne. Diffusion coefficient is found lower in the core of QSH plasmas than MH ones, confirming the enhancement in confinement and the reduction of stochasticity in the core which characterised the QSH states.

Lithium collisional-radiative code has been tested for the first time by simulating Li pellet injections. The increase in plasma density and SXR radiation was reproduced by the code, along with SXR brightness profiles. Transport coefficients for lithium were estimated in MH magnetic regime. They were found similar to those determined for the other impurities (C, O , Ne, Ni). This suggests that transport in RFX-mod is little dependent on the mass/charge of the different species.

Besides these experiments with light impurities, first experiments with tungsten have been carried out in RFX-mod. Small quantities of W have been introduced in the plasma through the laser blow-off technique. W emission spectra have been acquired in different wavelength regions at $T_e \sim 600 - 800$ eV and compared with analogous spectra observed at higher temperatures in other devices. The observed spectral features resulted similar to those observed in other devices, in particular strong quasi-continuum emissions were found at 35, 50 and 200 Å, in agreement with what reported in other experiments.

W penetrating capability has been checked by measuring total radiation and SXR emissions. Tomographic reconstructions of the emissivity profiles in these two energy ranges showed clear W radiative layers in the external region. These rings are explained by the fact that tungsten ions remain confined in the external region without progressing in the core plasma; no accumulation has been observed. The capability of RFX-mod plasmas, especially during QSH states, of confining impurities in the external region is therefore extended to tungsten. Its feature to remain in the outer region, where it radiates less, is appealing in the view of the possible RFX-mod's first wall renewal. In fact tungsten is one of the possible candidates for the replacement of the present low-performing C wall, thanks to its good properties: low H retention, sustainment of high power loads and neutral reflection energy higher than C.

In conclusion, the transport of impurities in RFX-mod has been confirmed to be characterised by a strong outward convection of ions, especially during the QSH states. These experimental observations are, however, not validated by any theoretical models, being the estimated transport coefficients not in agreement with classical or stochastic expectations. More theoretical work is therefore needed to explain what is the nature of this transport.

From an experimental point of view, further experiments with carbon pellets would validate the simulations presented in this thesis, which rely on few shots. Furthermore, the overcoming of the difficulties in operating the diagnostic neutral beam installed on RFX-mod would allow to have density measurements of intrinsic impurities. So far large stray fields plus high neutral pressure in the duct hamper beam penetration above 600 kA of plasma current.

In MST RFP the simulations of intrinsic impurity densities have been compared to the measurements carried out in the past years through the charge-exchange recombination spectroscopy. The density profile of the fully stripped carbon was measured in standard discharges, while dur-

ing improved confinement (PPCD) discharges density profiles of fully stripped boron, carbon and oxygen were measured. By reproducing those profiles through the transport codes, an estimate of the transport coefficients in the two different magnetic regimes was obtained.

In standard discharges, characterised by a high level of magnetic fluctuations, the fully stripped carbon profile is nearly flat. This profile has been reproduced assuming a high D and a strong outward v in the core. Diffusion coefficient was found in agreement with theoretical predictions from the stochastic diffusion, while the convective velocity was not.

In PPCD discharges, characterised by a reduced magnetic stochasticity, the fully stripped profiles of B, C and O result hollow, clearly indicating an outward flux of ions. Temporal evolution of the profiles of B^{+5}, C^{+6} and O^{+8} has been successfully simulated. The assumed transport coefficients resulted low and close to the values predicted by the classical theory of transport. The same coefficients well reproduced the behaviour of the three species, revealing a mass/charge independence of the transport parameters. The outward convection of impurities was explained by the classical temperature screening effect.

In conclusion this analysis on MST revealed a different nature of the impurity transport between the two magnetic regimes. In the standard plasmas transport is governed by the stochasticity of the field lines. In the improved confinement plasmas transport is close to classical, as predicted for an ideal RFP without magnetic fluctuations.

Further density measurements would help constrain this depicted figure, in particular time dependent measurements in standard plasmas could lead to better determine the transport coefficients, beyond the poor steady-state determination. Moreover, transient experiments like those performed at RFX-mod could be of great importance in the validation of the transport properties of the different impurities.

From a computational point of view, the assembly of a collisional-radiative code for aluminium, the additional intrinsic impurity present in MST, would make possible to reconstruct the SXR radiation, which is of great importance in studying the impurity behaviour.

Bibliography

[1] C. D. Michelis and M. Mattioli, "Spectroscopy and impurity behaviour in fusion plasmas," *Reports on Progress in Physics* **47** (1984) 1233.

[2] W. O. Hofer and J. Roth, *Physical processes of the interaction of fusion plasmas with solids*. Academic Press, New York, 1996.

[3] V. Philipps, "Plasma Wall Interaction and Its Control by Wall Conditioning," *Fusion Science and Technology* **45** (2004) 237–248.

[4] S. Munaretto, *First wall conditioning and plasma edge studies in RFP and Tokamak devices*. PhD thesis, University of Padua, 2012.

[5] J. Wesson, *Tokamaks*. Clarendon Press, Oxford, third ed., 2004.

[6] W. Möller, "Hydrogen trapping and transport in carbon," *Journal of Nuclear Materials* **162 - 164** (1989) 138.

[7] M. G. Bell *et al.*, "Plasma response to lithium-coated plasma-facing components in the National Spherical Torus Experiment," *Plasma Physics and Controlled Fusion* **51** no. 12, (2009) 124054.

[8] G. Mazzitelli *et al.*, "FTU results with a liquid lithium limiter," *Nuclear Fusion* **51** (2011) 073006.

[9] S. Munaretto *et al.*, "RFX-mod wall conditioning by lithium pellet injection," *Nuclear Fusion* **52** (2012) 023012.

[10] H. R. Griem, *Plasma spectroscopy*. McGraw-Hill, New York, 1964.

[11] Y. B. Zel'dovich and Y. P. Raizer, *Physics of shock waves and high temperature hydrodynamic phenomena*, vol. 1. Academic Press, New York, 1966.

[12] C. D. Michelis and M. Mattioli, "Soft-X-ray spectroscopic diagnostics of laboratory plasmas," *Nuclear Fusion* **21** (1981) 677.

[13] I. H. Hutchinson, *Principles of plasma diagnostics*. Cambridge University Press, Cambridge, 1987.

[14] L. Marrelli *et al.*, "Edge localised asymmetric radiative phenomena in RFX," *Journal of nuclear materials* **266** (1999) 877.

[15] R. V. Jensen *et al.*, "Calculations of impurity radiation and its effects on tokamak experiments," *Nuclear Fusion* **17** (1977) 1187.

[16] M. O'Mullane, "ADAS-EU course." Consorzio rfx, padua, italy, 26-30 march, 2012. http://www.adas-fusion.eu/.

[17] R. W. P. McWhirter, *Plasma Diagnostic Techniques*. Academic Press, New York, 1965.

[18] S. D. Loch *et al.*, "Collisional-radiative study of lithium plasmas," *Phys. Rev. E* **69** (2004) 066405.

[19] L. Lauro-Taroni *et al.*, "Assessment of the Superstage Description of Heavy Impurities for JET and ITER," in *Proceedings of the 35th EPS Conference on Plasma Physics*, D1.003. Hersonissos, Greece, 2008.

[20] M. F. Stamp *et al.*, "Particle influx measurements in jet helium plasmas using a multichannel visible spectrometer," *Journal of Nuclear Materials* **162-164** (1989) 404.

[21] M. N. Rosenbluth *et al.*, "Plasma Transport in Toroidal Confinement Systems," *Physics of Fluids* **15** (1972) 116.

[22] A. A. Galeev, "Diffusion-electrical Phenomena in a Plasma Confined in a Tokamak Machine," *Soviet Physics JETP* **32** (1971) 752.

[23] L. Solovev and V. Shafranov, "Effects of curvature on classical diffusion and thermal conductivity," in *Reviews of plasma physics*, vol. 5, p. 145. Consultants Bureau, New York, 1970.

[24] K. W. Wenzel and D. J. Sigmar, "Neoclassical analysis of impurity transport following transition to improved particle confinement," *Nuclear Fusion* **30** (1990) 1117.

[25] V. M. Zhdanov, *Transport Processes in Multicomponent Plasma*. Taylor & Francis, London, 2002.

[26] S. P. Hirshman and D. J. Sigmar, "Neoclassical transport of impurities in tokamak plasmas," *Nuclear Fusion* **21** (1981) 1079.

[27] A. Samain and F. Werkoff, "Diffusion in tokamaks with impurities in the Pfirsch-Schlüter regime," *Nuclear Fusion* **17** (1977) 53.

[28] R. Dux and A. G. Peeters, "Neoclassical impurity transport in the core of an ignited tokamak plasma," *Nuclear Fusion* **40** (2000) 1721.

[29] R. Guirlet *et al.*, "Parametric dependences of impurity transport in tokamaks," *Plasma Physics and Controlled Fusion* **48** (2006) B63.

[30] ITER Physics Expert Groups *et al.*, "Chapter 2: Plasma confinement and transport," *Nuclear Fusion* **39** (1999) 2175.

[31] H. Takenaga *et al.*, "Relationship between particle and heat transport in JT-60U plasmas with internal transport barrier," *Nuclear Fusion* **43** (2003) 1235.

[32] R. Neu *et al.*, "Tungsten: an option for divertor and main chamber plasma facing components in future fusion devices," *Nuclear Fusion* **45** (2005) 209.

[33] K. Molvig *et al.*, "Evidence for Magnetic Fluctuations as the Heat-Loss Mechanism in the Alcator Tokamak," *Physical Review Letters* **41** (1978) 1240.

[34] R. W. Harvey *et al.*, "Electron Dynamics Associated with Stochastic Magnetic and Ambipolar Electric Fields," *Physical Review Letters* **47** (1981) 102.

[35] A. B. Rechester and M. N. Rosenbluth, "Electron Heat Transport in a Tokamak with Destroyed Magnetic Surfaces," *Physical Review Letters* **40** (1978) 38.

[36] J. Y. Hsu *et al.*, "Anomalous impurity ion transport due to magnetic fluctuations," *Physics of Fluids* **24** (1981) 2216.

[37] L. Lauro-Taroni *et al.*, "Time-dependent modelling of impurity transport in the jet core and divertor plasma," *Contributions to Plasma Physics* **38** (1998) 242–247.

[38] D. D. S. S Ortolani, *Magnetohydrodynamics of Plasma Relaxation*. World Scientific, Singapore, 1993.

[39] F. D'Angelo and R. Paccagnella, "The stochastic diffusion process in reversed-field pinch," *Physics of Plasmas* **3** (1996) 2353.

[40] T. Tamano *et al.*, "Observation of a new toroidally localized kink mode and its role in reverse-field- Pinch plasmas," *Physical review letters* **59** (1987) 1444.

[41] D. Escande *et al.*, "Quasi-single-helicity reversed-field-pinch plasmas," *Physical Review Letters* **85** (2000) 1662.

[42] P. Martin *et al.*, "Overview of quasi-single helicity experiments in reversed field pinches," *Nuclear fusion* **43** (2003) 1855.

[43] R. Lorenzini *et al.*, "Self-organized helical equilibria as a new paradigm for ohmically heated fusion plasmas," *Nature Physics* **5** (2009) 570.

[44] A. Galeev and R. Sagdeev, "Transport phenomena in a collisionless plasma in a toroidal magnetic system," *Sov. Phys. JETP* **26** (1968) 233.

[45] M. Wakatani and R. Itatani, "Collisional Diffusion in a Toroidal Pinch," *Journal of the Physical Society of Japan* **34** (1973) 181.

[46] V. D. Shafranov, *Review of Plasma Physics*, vol. 2. Consultants Bureau, New York, 1966.

[47] H. Oshiyama and S. Masamune, "MHD diffusion in the reversed field pinch plasma," *Journal of the Physical Society of Japan* **52** (1983) 2041.

[48] T. Chen *et al.*, "Monte Carlo studies of transport in a reversed field pinch," *Journal of the Physical Society of Japan* **61** (1992) 530.

[49] R. Lorenzini *et al.*, "Particle transport in reversed field pinch helium plasmas," *Physics of Plasmas* **13** (2006) 112510.

[50] D. Terranova *et al.*, "Experimental particle transport studies by pellet injection in helical equilibria," *Nuclear Fusion* **50** (2010) 035006.

[51] J. Sarff *et al.*, "Fluctuation and transport reduction in a reversed field pinch by inductive poloidal current drive," *Physical review letters* **72** (1994) 3670.

[52] B. E. Chapman *et al.*, "High confinement plasmas in the Madison Symmetric Torus reversed-field pinch," *Physics of Plasmas* **9** (2002) 2061–2068.

[53] P. Franz *et al.*, "Observations of multiple magnetic islands in the core of a reversed field pinch," *Physical review letters* **92** (2004) 125001.

[54] R. O'Connell *et al.*, "Observation of velocity-independent electron transport in the reversed field pinch," *Physical review letters* **91** (2003) 045002.

[55] S. Menmuir *et al.*, "Impurity transport studies in RFX-mod multiple helicity and enhanced confinement QSH regimes," *Plasma Physics and Controlled Fusion* **52** (2010) 095001.

[56] S. T. A. Kumar *et al.*, "Classical confinement and outward convection of impurity ions in the MST RFP," *Physics of Plasmas* **19** (2012) 056121.

[57] L. Carraro *et al.*, "Collisional-Radiative models for hydrogen-like and helium-like carbon and oxygen ions and applications to experimental data from the TS tokamak and the reversed field pinch RFX," *Physica Scripta* **55** (1997) 565.

[58] A. Canton *et al.*, "Studies of spatial uniformity of glow discharge cleaning plasmas on the RFX-mod device," *Journal of Nuclear Materials* **438, Supplement** (2013) S1164.

[59] H. P. Summers, *The Adas User Manual version 2.6*, 2004. http://www.adas.ac.uk/.

[60] L. Carraro *et al.*, "Carbon and oxygen behaviour in the reversed field pinch RFX," *Nuclear Fusion* **36** (1996) 1623.

[61] S. T. A. Kumar *et al.*, "Behaviour of carbon and boron impurities in the Madison Symmetric Torus," *Plasma Physics and Controlled Fusion* **53** (2011) 032001.

[62] L. Carraro *et al.*, "Reconstruction of the radiation emitted by the intrinsic impurities in the RFX reversed field pinch," *Plasma Physics and Controlled Fusion* **42** (2000) 731.

[63] H. P. Summers *et al.*, "Radiative power loss from laboratory and astrophysical plasmas. I. Power loss from plasmas in steady-state ionisation balance," *Journal of Physics B: Atomic and Molecular Physics* **12** (1979) 2387.

[64] W. J. Karzas *et al.*, "Electron Radiative Transitions in a Coulomb Field," *Astrophysical Journal Supplement* **6** (1961) 167.

[65] R. D. Gill *et al.*, "Soft X-ray measurements of the impurity density in DITE," *Nuclear Fusion* **19** (1979) 1003.

[66] L. Carraro *et al.*, "Impurity transport during pulsed poloidal current drive experiment in the reversed field pinch experiment RFX," *Plasma Physics and Controlled Fusion* **44** (2002) 2135.

[67] P. B. Parks *et al.*, "Analysis of low Z a impurity pellet ablation for fusion diagnostic studies," *Nuclear Fusion* **28** (1988) 477.

[68] L. Garzotti *et al.*, "Noncryogenic pellet injector for diagnostic purposes on the RFX reversed field pinch," *Review of Scientific Instruments* **70** (1999) 939.

[69] P. Sonato *et al.*, "Machine modification for active MHD control in RFX," *Fusion engineering and design* **66** (2003) 161.

[70] G. Rostagni, "RFX: an expected step in RFP research," *Fusion engineering and design* **25** (1995) 301.

[71] P. Martin *et al.*, "Overview of RFX-mod results," *Nuclear Fusion* **49** (2009) 104019.

[72] F. D'Angelo and R. Paccagnella, "The stochastic diffusion process in reversed-field pinch," *Physics of Plasmas* **3** (1996) 2353.

[73] M. Valisa *et al.*, "High current regimes in RFX-mod," *Plasma Physics and Controlled Fusion* **50** (2008) 124031.

[74] L. Carraro *et al.*, "Improved confinement with internal electron transport barriers in RFX-mod," *Nuclear Fusion* **49** (2009) 055009.

[75] P. Scarin *et al.*, "Topology and transport in the edge region of RFX-mod helical regimes," *Nuclear Fusion* **51** (2011) 073002.

[76] P. Sonato *et al.*, "Boronization with trimethylboron in the reversed field pinch RFX," *Journal of nuclear materials* **227** (1996) 259.

[77] M. Puiatti *et al.*, "Wall conditioning and density control in the reversed field pinch RFX-mod," *Nuclear Fusion* **53** (2013) 073001.

[78] P. Innocente and S. Martini, "A two color multichord infrared interferometer for RFX," *Review of scientific instruments* **63** (1992) 4996.

[79] P. Innocente *et al.*, "Upgrade of the RFX CO_2 interferometer using in-vessel optics for extended edge resolution," *Review of scientific instruments* **68** (1997) 694.

[80] A. Murari *et al.*, "An optimized multifoil soft x-ray spectrometer for the determination of the electron temperature with high time resolution," *Review of scientific instruments* **70** (1999) 581.

[81] A. Alfier and R. Pasqualotto, "New Thomson scattering diagnostic on RFX-mod," *Review of Scientific Instruments* **78** (2007) 013505.

[82] F. Bonomo *et al.*, "A multichord soft x-ray diagnostic for electron temperature profile measurements in RFX-mod," *Review of scientific instruments* **77** (2006) 10F313.

[83] P. Franz *et al.*, "Experimental investigation of electron temperature dynamics of helical states in the RFX-Mod reversed field pinch," *Nuclear Fusion* **53** (2013) 053011.

[84] S. Menmuir *et al.*, "Edge spectroscopic characterization of RFX-mod after Li wall conditioning," in *Proceedings of the 37th EPS Conference on Plasma Physics*, P2.149. Dublin, Ireland, 2010.

[85] P. Franz *et al.*, "Soft X ray tomographic imaging in the RFX reversed field pinch," *Nuclear fusion* **41** (2001) 695.

[86] D. Terranova *et al.*, "A 3D approach to equilibrium, stability and transport studies in RFX-mod improved regimes," *Plasma Physics and Controlled Fusion* **52** (2010) 124023.

[87] J. Schwob *et al.*, "High-resolution duo-multichannel soft x-ray spectrometer for tokamak plasma diagnostics," *Review of scientific instruments* **58** (1987) 1601.

[88] F. Bonomo *et al.*, "Experimental background emissivity at the transitions useful for the active CXRS in RFX-mod," in *Proceeding of the 51st Annual Meeting of the Division of Plasma Physics*, TP8.00085. Atlanta, GA, 2009.

[89] E. Müller and F. Mast, "A new metal resistor bolometer for measuring vacuum ultraviolet and soft x radiation," *Journal of applied physics* **55** (1984) 2635.

[90] G. B. Sabine, "Reflectivities of Evaporated Metal Films in the Near and Far Ultraviolet," *Physical Review* **55** (1939) 1064.

[91] P. Innocente *et al.*, "Three-dimensional time-resolved H pellet trajectory reconstruction in RFX by position sensitive detector H_α diagnostic," *Review of scientific instruments* **70** (1999) 943.

[92] F. M. Poli *et al.*, "Scaling of pellet ablation and trajectory deflection in RFX," in *Proceedings of the 26th EPS Conference on Controlled Fusion and Plasma Physics*, P3.050. Maastricht, The Netherlands, 1999.

[93] A. Alfier *et al.*, "Electron pressure measurements in the outer region of RFX-mod with the upgraded edge Thomson scattering diagnostic," *Plasma Physics and Controlled Fusion* **52** (2010) 035004.

[94] T. Pütterich, *Investigations on Spectroscopic Diagnostic of High-Z Elements in Fusion Plasmas*. PhD thesis, University of Augsburg, 2005.

[95] L. Carraro *et al.*, "A wide wavelength range spectrometer (1150–8000 Å) for the RFX reversed field pinch experiment," *Review of scientific instruments* **63** (1992) 5188.

[96] L. Carraro *et al.*, "Absolute calibration of a vacuum Czerny–Turner spectrometer in the range 1200–7000 Å," *Review of scientific instruments* **66** (1995) 613.

[97] R. C. Isler *et al.*, "Tungsten radiation from tokamak-produced plasmas," *Physics Letters A* **63** (1977) 295.

[98] E. Hinnov *et al.*, "Effects of tungsten radiation on the behaviour of PLT tokamak discharges," *Nuclear Fusion* **18** (1978) 1305.

[99] T. Pütterich *et al.*, "Modelling of measured tungsten spectra from ASDEX Upgrade and predictions for ITER," *Plasma Physics and Controlled Fusion* **50** (2008) 085016.

[100] R. Radtke *et al.*, "Line and band emission from tungsten ions with charge 21+ to 45+ in the 45–70-Å range," *Physical Review A* **64** (2001) 012720.

[101] M. Finkenthal *et al.*, "Soft X-ray bands of highly ionized tungsten, gold and lead emitted by the TEXT tokamak plasma," *Physics Letters A* **127** (1988) 255.

[102] R. Fonck *et al.*, "Multichannel grazing-incidence spectrometer for plasma impurity diagnosis: SPRED," *Applied Optics* **21** (1982) 2115.

[103] M. O'Mullane *et al.*, "Diagnostic exploitation of complex heavy elements in tokamak plasmas," *Review of scientific instruments* **74** (2003) 2080.

[104] G. Spizzo, *Thermal Properties of Improved Confinement Regimes in RFX*. PhD thesis, University of Padua, 2000.

[105] S. T. A. Kumar *et al.*, "High resolution charge-exchange spectroscopic measurements of aluminum impurity ions in a high temperature plasma," *Plasma Physics and Controlled Fusion* **54** (2012) 012002.

[106] J. S. Sarff *et al.*, "Tokamak-like confinement at high beta and low field in the reversed field pinch," *Plasma Physics and Controlled Fusion* **45** (2003) A457.

[107] N. E. Lanier *et al.*, "Control of Density Fluctuations and Electron Transport in the Reversed-Field Pinch," *Phys. Rev. Lett.* **85** (2000) 2120–2123.

[108] M. D. Wyman *et al.*, "High-beta, improved confinement reversed-field pinch plasmas at high density," *Physics of Plasmas* **15** (2008) 010701.

[109] D. J. D. Hartog *et al.*, "Isotropy of ion heating during a sawtooth crash in a reversed-field pinch," *Plasma Physics and Controlled Fusion* **42** (2000) L47.

[110] D. J. D. Hartog *et al.*, "Advances in neutral-beam-based diagnostics on the Madison Symmetric Torus reversed-field pinch (invited)," *Review of Scientific Instruments* **77** (2006) 10F122.

[111] P. Innocente *et al.*, "An infrared vibration compensated interferometer for the MST experiment," *Review of Scientific Instruments* **63** (1992) 4999.

[112] J. A. Reusch *et al.*, "Multipoint Thomson scattering diagnostic for the Madison Symmetric Torus reversed-field pinch," *Review of Scientific Instruments* **79** (2008) 10E733.

[113] D. L. Brower *et al.*, "Multichannel far-infrared polarimeter-interferometer system on the MST reversed field pinch," *Review of Scientific Instruments* **72** (2001) 1077–1080.

[114] D. W. Marquardt, "An Algorithm for Least-Squares Estimation of Nonlinear Parameters," *Journal of the Society for Industrial and Applied Mathematics* **11** (1963) 431–441.

[115] B. E. Chapman *et al.*, "Sawteeth and energy confinement in the Madison Symmetric Torus reversed-field pinch," *Physics of Plasmas* **3** (1996) 709–711.

[116] B. Hudson, *Fast Ion Confinement in The Reversed-Field Pinch*. PhD thesis, University of Wisconsin - Madison, 2006.

[117] J. Anderson *et al.*, "Equilibrium reconstruction in the Madison Symmetric Torus reversed field pinch," *Nuclear fusion* **44** (2004) 162.

[118] D. Schnack *et al.*, "Semi-implicit magnetohydrodynamic calculations," *Journal of Computational Physics* **70** (1987) 330.

[119] D. J. Clayton *et al.*, "An upgraded x-ray spectroscopy diagnostic on MST," *Review of Scientific Instruments* **81** (2010) 10E308.

[120] P. Franz *et al.*, "High resolution soft x-ray tomography in the Madison Symmetric Torus," *Review of Scientific Instruments* **75** (2004) 4013–4016.